

Winter 2-23-2019

Development of an Astrocyte/Glioma Co-Culture System for Measuring Cellular Dynamics

Urna Kansakar

Follow this and additional works at: <https://digitalcommons.latech.edu/dissertations>

 Part of the [Bioelectrical and Neuroengineering Commons](#), and the [Other Biomedical Engineering and Bioengineering Commons](#)

**DEVELOPMENT OF AN ASTROCYTE/GLIOMA
CO-CULTURE SYSTEM FOR MEASURING
CELLULAR DYNAMICS**

by

Urna Kansakar, M.S.

A Dissertation Presented in Partial Fulfillment
of the Requirements of the Degree
Doctor of Philosophy

COLLEGE OF ENGINEERING AND SCIENCE
LOUISIANA TECH UNIVERSITY

February 2019

LOUISIANA TECH UNIVERSITY
THE GRADUATE SCHOOL

DECEMBER 17, 2018

Date

We hereby recommend that the dissertation prepared under our supervision by
Urna Kansakar, M.S.

entitled **Development of an Astrocyte/glioma Co-culture System for Measuring
Cellular Dynamics**

be accepted in partial fulfillment of the requirements for the Degree of
Doctor of Philosophy in Biomedical Engineering

Supervisor of Dissertation Research

Head of Department
Biomedical Engineering

Department

Recommendation concurred in:

Advisory Committee

Approved:

Director of Graduate Studies

Dean of the College

Approved:

Dean of the Graduate School

ABSTRACT

Gliomas are brain tumors that primarily arise from glial cells. Gliomas account for 70% of the brain tumors and they are more prevalent in older adults. About 60% of the people with gliomas experience at least one seizure. Brain tumors can grow and metastasize to neighboring areas, thereby destroying normal brain cells. In a brain tumor microenvironment, both malignant cancer cells and healthy brain cells are present. Studies have shown that astrocytes may have a role in tumor growth in the brain. Monocultures cannot evaluate interactions between two cell types and does not accurately represent *in vivo* conditions. Thus, a co-culture *in vitro* cell model is needed to gain better insight into the dynamics of the system. However, co-cultures are challenging as the two different cell types have different growth rates and the population ratios must be optimized to achieve a stable system. A co-culture experimental model comprised of normal brain cells and cancer cells will be beneficial as it mimics the brain tumor microenvironment. In this work, a mixed co-culture method was employed to simulate a diseased state of the brain and study cell-cell interactions between normal brain astrocytes and glioma cells. In addition, tumor invasion in the presence of normal brain cells was studied. This research enhances understanding on the brain tumor microenvironment and cancer progression. Signaling molecules such as neurotransmitter will be considered in this system, one of these, glutamate, is a major excitatory neurotransmitter and plays a major role in normal functioning of the brain. However,

excess glutamate is present in numerous neurological disorders such as seizure, and epilepsy. Moreover, few studies have examined the uptake of glutamate in co-culture of glioma cells and normal brain astrocytes. In the present study, glutamate uptake was measured in normal brain astrocytes, glioma cells and combination of both cell types using a quantitative colorimetric assay kit. Results showed that co-culture of glioma cells with astrocytes enhanced the uptake of glutamate by astrocytes as compared with uptake by astrocytes alone. Furthermore, changes in morphology in normal brain cells were observed in sodium-free medium when sodium-dependent transporters were blocked. New approaches were developed to modify brain cell microenvironment using engineered micro/nano materials and chemical treatments such as staurosporine. Finally, the potential applications of Copper-containing High Aspect Ratio Structures (CuHARS), a promising novel biomaterial, were explored for biomedical purposes such as incorporating them with cellulose to construct a stable matrix for CuHARS delivery in glioma cells. In addition, interaction of sonicated CuHARS was investigated in a co-culture model developed earlier in this project and degradation of the sonicated CuHARS was studied to quantify degradable biomaterials.

APPROVAL FOR SCHOLARLY DISSEMINATION

The author grants to the Prescott Memorial Library of Louisiana Tech University the right to reproduce, by appropriate methods, upon request, any or all portions of this Dissertation. It is understood that “proper request” consists of the agreement, on the part of the requesting party, that said reproduction is for his personal use and that subsequent reproduction will not occur without written approval of the author of this Dissertation. Further, any portions of the Dissertation used in books, papers, and other works must be appropriately referenced to this Dissertation.

Finally, the author of this Dissertation reserves the right to publish freely, in the literature, at any time, any or all portions of this Dissertation.

Author _____

Date _____

DEDICATION

I dedicate this dissertation to my family, Abhaya Ratna Kansakar (dad), Roshani Kansakar (mom), and Vipasana Kansakar (sister), who offered unconditional love and support throughout my journey. I cannot thank you enough for always being there for me.

TABLE OF CONTENTS

ABSTRACT.....	iii
APPROVAL FOR SCHOLARLY DISSEMINATION	v
DEDICATION	vi
LIST OF FIGURES	xiii
LIST OF TABLES	xx
ACKNOWLEDGMENTS	xxi
CHAPTER 1 INTRODUCTION	1
1.1 Motivation.....	1
1.2 Objectives	4
1.3 Dissertation Overview	5
CHAPTER 2 BACKGROUND AND LITERATURE REVIEW	6
2.1 Gliomas.....	6
2.2 Astrocytes	7
2.3 Cells	8
2.3.1 CRL-2303 Glioma Cell Line	8
2.3.2 Rat Astrocytes.....	9
2.4 Co-culture	10
2.4.1 Cultures with Cell-cell Contact.....	12
2.4.1.1 Mixed co-culture	12
2.4.1.2 Micropatterning.....	13
2.4.1.3 Temporary divider.....	13

2.4.2	Cultures without Cell-cell Contact.....	14
2.4.2.1	Segregated co-culture.....	14
2.4.2.2	Conditioned media	14
2.4.2.3	Porous membrane.....	15
2.5	Co-culture of Astrocytes and Gliomas.....	15
2.6	Neurotransmitters.....	17
2.6.1	History of the Discovery of Neurotransmitters.....	19
2.6.2	Fate of a Neurotransmitter	20
2.7	Glutamate.....	21
2.7.1	Chemistry of Glutamate	22
2.7.2	Chemistry of Glutamine.....	23
2.7.3	Glutamate Receptors	23
2.7.4	Glutamate Transporters.....	24
2.7.5	Low Affinity Transporters	25
2.7.6	High Affinity Transporters	26
2.8	Mechanism of Glutamate Removal	26
2.9	Glutamate-Glutamine Cycle	27
2.10	Role of Glutamate in Epilepsy and Seizures	28
2.11	Gliomas and Excitotoxicity	28
2.11.1	The Cystine/Glutamate Antiporter System (X_c^-).....	29
2.12	Mechanism to Block Sodium-Dependent Transporters.....	30
2.12.1	Locke's Solution	30
2.12.2	Chemistry of Choline Chloride.....	31
2.13	MTT Assay	32
2.14	Apoptosis	33

2.15	Necrosis	33
CHAPTER 3 USE OF A TWO-DIMENSIONAL <i>IN VITRO</i> CO-CULTURE MODEL WITH NORMAL BRAIN ASTROCYTES AND GLIOMA CELLS FOR ENGINEERING THE TUMOR MICROENVIRONMENT		
34		
3.1	Introduction.....	34
3.2	Materials and Methods.....	35
3.2.1	Cell Culture.....	35
3.2.2	Cell Fixation.....	36
3.2.3	GFAP Staining.....	36
3.2.4	β -gal Staining.....	36
3.2.5	DAPI Staining.....	36
3.2.6	Microscopy	37
3.2.7	Image Analysis.....	37
3.3	Results.....	37
3.3.1	GFAP Staining.....	37
3.3.2	β -gal Staining.....	41
3.3.3	Staining Co-culture with GFAP and β -gal.....	43
3.3.4	Identifying Cell Types Using Size and Shape of Nuclei	46
3.3.5	Tumor Invasion in Co-culture.....	52
3.4	Conclusion and Discussion.....	56
CHAPTER 4 STUDYING GLUTAMATE UPTAKE IN A CO-CULTURE EXPERIMENTAL MODEL OF NORMAL BRAIN ASTROCYTES AND GLIOMA CELLS		
58		
4.1	Introduction.....	58
4.2	Materials and Methods.....	59
4.2.1	Cell Culture.....	59
4.2.2	Glutamate Assay	60

4.2.3	Sodium (Na ⁺) Transport Test.....	60
4.2.4	MTT Assay	60
4.2.5	Statistics	61
4.3	Results.....	61
4.3.1	Glutamate Uptake	61
4.3.2	Cell Metabolism.....	68
4.4	Conclusion and Discussion.....	70
CHAPTER 5 APPROACHES FOR MODIFICATION OF BRAIN CELLS USING ENGINEERED MICRO/ NANOMATERIALS.....		72
5.1	Introduction.....	72
5.2	Materials and Methods.....	73
5.2.1	Creating Nanofilms	73
5.2.2	Chemicals.....	73
5.2.3	Preparation of Halloysite Drug Composites	74
5.2.4	LbL Assembly on Halloysite	74
5.2.5	Cell Culture.....	75
5.2.6	Microscopy	75
5.2.7	MTT Assay	75
5.3	Results.....	76
5.3.1	Creating Nanofilms.....	76
5.3.2	Effect of Nanofilms on Cells	76
5.3.3	Drug Delivery Using Halloysite Nanotubes	81
5.4	Conclusions.....	88
CHAPTER 6 POTENTIAL APPLICATIONS OF COPPER CONTAINING HIGH ASPECT RATIO STRUCTURES (CUHARS) FOR BIOMEDICAL PURPOSES		89
6.1	Introduction.....	89

6.2	Materials and Methods.....	90
6.2.1	Materials and Reagents	90
6.2.2	Sonication of CuHARS.....	90
6.2.3	Generation of Cellulose Films and Cellulose Hybrid Materials.....	90
6.2.4	Cell Culture.....	92
6.2.5	Digital Microscopy Imaging.....	92
6.2.6	Image Analysis.....	92
6.3	Results.....	92
6.3.1	Integration of CuHARS with Cellulose and Magnetic Susceptible Nanoparticles	92
6.3.2	Application of Constructed Cellulose Materials to Aqueous Solutions	95
6.3.3	Cellular Interaction of Sonicated CuHARS in a Co-culture Model	97
6.4	Conclusion and Discussion.....	109
CHAPTER 7 CONCLUSIONS AND FUTURE WORK.....		112
APPENDIX A CELL CULTURE MEDIA.....		115
A.1	CRL-2303 Media	116
A.1.1	Materials Required for 250 mL Media	116
A.1.2	Preparation of CRL-2303 Growth Media	116
A.2	Astrocyte Media.....	116
A.2.1	Materials Required for 250 mL Media	116
A.2.2	Preparation of Astrocyte Growth Media.....	117
A.3	Microglia Media	117
A.3.1	Materials Required for 250 mL Media	117
A.3.2	Preparation of Microglia Growth Media.....	118
A.4	Locke’s Solution.....	118
A.4.1	Materials Required for 250 mL Media	118

APPENDIX B	FIXING CELLS	120
APPENDIX C	GFAP ANTIBODY (Ab) STAINING.....	122
APPENDIX D	β -GALACTOSIDASE STAINING.....	125
D.1.1	Reagents Required for Staining	126
D.1.2	Preparation Instructions	126
D.1.3	Procedure for 48-well Cell Culture Plate.....	126
APPENDIX E	DAPI STAINING PROTOCOL.....	128
APPENDIX F	IMAGE-PRO PLUS VERSION 7.0.....	130
F.1.1	Calculating the Area of β -gal Staining from the Image.....	131
	Bibliography	134

LIST OF FIGURES

Figure 1.1: Schematic diagram of some major cell types that comprises tumor microenvironment in the brain [8].	2
Figure 2.1: Major types of astrocytes	8
Figure 2.2: Phase contrast microscopy of CRL-2303 glioma cell line a) Pre X-gal treatment b) Post X-gal treatment. Scale bar = 100 um.	9
Figure 2.3: Rat Astrocytes a) Phase contrast microscopy before GFAP staining b) Fluorescence microscopy after GFAP staining. Scale bar = 100 um.	10
Figure 2.4: Schematic of a two-dimensional <i>in vitro</i> co-culture systems to evaluate cell-cell interactions a) Mixed co-culture; b) Micropatterning; c) Temporary divider; d) Segregated co-culture; e) Conditioned media; f) Porous membrane [34].	12
Figure 2.5: Schematic representation of a) normal rat brain astrocytes; b) glioma cells (CRL-2303); c) co-culture of normal rat brain astrocytes and glioma cells.	16
Figure 2.6: Schematic representation of a chemical synapse [54].	18
Figure 2.7: Classification of Neurotransmitters.	19
Figure 2.8: [Modified] Schematic representation of the fate of neurotransmitter after it is released [63].	21
Figure 2.9: Chemical structure of Glutamate.	22
Figure 2.10: Chemical structure of Glutamine	23
Figure 2.11: Schematics demonstrating sodium-dependent glutamate transporters (EAAT1-EAAT4) and glutamate receptor [81].	25
Figure 2.12: Schematic illustration of the release of neurotransmitters from the synaptic vesicles, glutamate-glutamine cycle, and generation of epileptic discharge [84].	28
Figure 2.13: Xc ⁻ system in glioma cells [66].	30
Figure 2.14: Chemical structure of choline chloride	31

Figure 2.15: Reaction scheme for MTT reduction [96]..... 32

Figure 3.1: GFAP staining for 12,000 normal brain astrocytes cells per mL. The left panel shows phase contrast images before GFAP staining and the right panel shows fluorescence images after GFAP staining. The images in the top row are positive control with both primary and secondary antibodies (1° Ab + 2° Ab) and the images in the bottom row are negative control with no primary antibody (1° Ab). Scale bar = 100 μ m. 38

Figure 3.2: GFAP staining for 24,000 normal brain astrocytes cells per mL. The left panel shows phase contrast images before GFAP staining and the right panel shows fluorescence images after GFAP staining. The images in the top row are positive control with both primary and secondary antibodies (1° Ab + 2° Ab) and the images in the bottom row are negative control with no primary antibody (1° Ab). Scale bar = 100 μ m. 39

Figure 3.3: GFAP staining for 4,000 glioma cells (CRL-2303) per mL. The left panel shows phase contrast images before GFAP staining and the right panel shows fluorescence images after GFAP staining. The images in the top row are positive control with both primary and secondary antibodies (1° Ab + 2° Ab) and the images in the bottom row are negative control with no primary antibody (1° Ab). Scale bar = 100 μ m. 40

Figure 3.4: GFAP staining for 8,000 glioma cells (CRL-2303) per mL. The left panel shows phase contrast images before GFAP staining and the right panel shows fluorescence images after GFAP staining. The images in the top row are positive control with both primary and secondary antibodies (1° Ab + 2° Ab) and the images in the bottom row are negative control with no primary antibody (1° Ab). Scale bar = 100 μ m. 41

Figure 3.5: β -gal staining for 4,000 glioma cells (CRL-2303) per mL. The left panel shows the image before β -gal staining and right panel shows the same image after β -gal staining. All the images are obtained using phase contrast microscopy. Scale bar = 100 μ m. 42

Figure 3.6: β -gal staining for 8,000 glioma cells (CRL-2303) per mL. The left panel shows the image before β -gal staining and the right panel shows the same image after β -gal staining. All the images are obtained using phase contrast microscopy. Scale bar = 100 μ m. 43

Figure 3.7: Control (no staining), GFAP and β -gal staining for co-culture of 4,000 glioma cells (CRL-2303) per mL and 12,000 normal brain astrocytes per mL. The left panel (Control) and the right panel (after β -gal staining) are the images obtained with phase contrast microscopy. The middle panel (after GFAP staining) are the images obtained with fluorescence microscopy, the top row is positive control with both primary and secondary antibodies (1° Ab + 2° Ab) and the bottom row is negative control with no primary antibody (1° Ab). Scale bar = 100 μ m. 44

Figure 3.8: Control (no staining), GFAP and β -gal staining for co-culture of 8,000 glioma cells (CRL-2303) per mL and 24,000 normal brain astrocytes per mL. The left panel (Control) and the right panel (after β -gal staining) are the images obtained with phase contrast microscopy. The middle panel (after GFAP staining) are the images obtained with fluorescence microscopy, the top row is positive control with both primary and secondary antibodies (1° Ab + 2° Ab) and the bottom row is negative control with no primary antibody (1° Ab). Scale bar = 100 μ m. 45

Figure 3.9: Fluorescence images of DAPI-stained nuclei for different densities (per mL) of glioma cells alone (CRL-2303), normal brain astrocytes alone, and co-cultured glioma cells and astrocytes. Scale bar = 100 μ m. 48

Figure 3.10: Control, DAPI-stained nuclei, and β -gal staining for co-culture of 4,000 cells per mL gliomas (CRL-2303) and 12,000 cells per mL normal brain astrocytes. Left panel represents phase contrast images (Control), middle panel shows fluorescent images of DAPI-stained nuclei, and right panel shows the same phase contrast images after staining with β -gal. Yellow arrows show glioma cells and white arrows show normal brain astrocytes. Scale bar = 100 μ m. 49

Figure 3.11: Control, DAPI-stained nuclei, and β -gal staining for co-culture of 8,000 cells per mL gliomas (CRL-2303) and 24,000 cells per mL normal brain astrocytes. Left panel shows phase contrast images (Control), middle panel shows fluorescent images of DAPI-stained nuclei, and right panel shows the same phase contrast images after staining with β -gal. Yellow arrows show glioma cells and white arrows show normal brain astrocytes. Scale bar = 100 μ m. 50

Figure 3.12: Average nuclei number covered by gliomas alone, normal brain astrocytes alone, and co-culture of gliomas with astrocytes after 3 days *in vitro* (div). Error bars indicate standard deviation (SD); * $P < 0.05$, $n = 9$ 51

Figure 3.13: Average nuclei area covered by gliomas alone, normal brain astrocytes alone, and co-culture of gliomas with astrocytes after 3 days *in vitro* (div). Error bars indicate standard deviation (SD); * $P < 0.05$, $n = 9$ 52

Figure 3.14: β -gal staining on co-culture of 3,000 glioma cells (CRL-2303) per mL and 12,000 normal brain astrocytes per mL at a) Day 2, b) Day 4, c) Day 6, and, d) Day 8. Scale bar = 100 μ m. 53

Figure 3.15: Total area coverage (%) by β -gal staining on co-culture of 3,000 glioma (CRL-2303) cells per mL and 12,000 normal brain astrocytes per mL over time. 54

Figure 3.16: Total unstained area (%) on co-culture of 3,000 glioma cells (CRL-2303) per mL and 12,000 normal brain astrocytes per mL over time. 54

Figure 3.17: DAPI staining on co-culture of 3,000 glioma cells per mL (CRL-2303) and 12,000 normal brain astrocytes per mL at a) Day 2, b) Day 4, c) Day 6, and, d) Day 8. Scale bar = 100 μ m. 55

- Figure 4.1:** Microscopic images of 100k, 50k and 25k cells per mL normal brain astrocytes after 5 days *in vitro* (div) before and after preincubation with 100 μ M glutamate for 5 hr at 37 $^{\circ}$ C. Scale bar = 200 μ m. Dotted square lines mark the same area between the left and right image and show that the morphology of the cells remained the same before and after addition of 100 μ M glutamate. 62
- Figure 4.2:** Microscopic images of 50k, 25k and 10k cells per mL glioma cells (CRL-2303) after 3 days *in vitro* (div) before and after preincubation with 100 μ M glutamate for 5 hr at 37 $^{\circ}$ C. Scale bar = 100 μ m. Dotted square lines mark the same area between the left and right image and show that the morphology of the cells remained the same before and after addition of 100 μ M glutamate. 63
- Figure 4.3:** Percentage of glutamate uptake by different densities of normal brain astrocytes and glioma cells (CRL-2303) at 3 days *in vitro* (div) after preincubation with 100 μ M Glu for 5 hr at 37 $^{\circ}$ C. Error bars indicate standard deviation (SD); * $P < 0.05$, $n = 3$ 64
- Figure 4.4:** Microscopic images of co-culture of 4,000 glioma cells per mL and 12,000 normal brain astrocytes per mL, and 8,000 gliomas per mL and 24,000 normal brain astrocytes per mL at 3 days *in vitro* (div) before and after preincubation with 100 μ M glutamate for 5 hr at 37 $^{\circ}$ C. Scale bar = 100 μ m. Dotted square lines mark the same area between the left and right image and show that the morphology of the cells remained the same before and after addition of 100 μ M glutamate. 66
- Figure 4.5:** Percentage of glutamate uptake by different densities of normal brain astrocytes and glioma cells, 3 days *in vitro* (div) after preincubation with 100 μ M Glu for 5 hr at 37 $^{\circ}$ C. Error bars indicate standard deviation (SD); * $P < 0.05$, $n = 3$ 67
- Figure 4.6:** MTT assay as a measure of cell metabolism with and without 100 μ M glutamate. Error bars indicate standard deviation (SD); n.s.= not significant at $P < 0.05$, $n = 4$ 68
- Figure 4.7:** 5k/well normal brain astrocytes a) Control (Astrocyte medium), b) LKS (sodium chloride), c) LKS (choline chloride) at 3 days *in vitro* (div) post 5 hr after replacement of complete astrocyte media. Scale bar: 100 μ m..... 69
- Figure 5.1:** Drying pattern of 100 μ g/mL CuNps nanofilms after baking for 6 hr. Red arrows indicate aggregates of copper nanoparticles. Scale bar = 50 μ m. 76
- Figure 5.2:** Representative images of microglia cells after they were seeded on top of the nanofilms created with 100 μ g/mL CuNps or various concentrations of STS (500 nM, 1 μ M, and 2 μ M). The images were obtained using phase contrast microscopy at 4, 24, and 48 hr respectively. Scale bar = 50 μ m. 77
- Figure 5.3:** Phase contrast and fluorescence images of microglia after DAPI staining at 72 hr. 20,000 cells/mL were plated after creating nanofilms with 100 μ g/mL CuNps (positive control) and different concentrations of STS (500 nM, 1 μ M, and 2 μ M). Scale bar = 50 μ m. 79

- Figure 5.4:** (A-B) Schematic of halloysite nanotube depicting characteristics and dimensions of halloysite nanotubes (C) SEM image of halloysite nanotubes (D) TEM image of halloysite nanotubes..... 82
- Figure 5.5:** Schematics illustrating the loading of camptothecin inside the lumen of halloysite nanotubes followed by deposition of natural polyelectrolytes and FITC using layer-by-layer (LbL) technique and delivering them to brain tumor cells (CRL-2303). 82
- Figure 5.6:** Zeta potential values after the addition of each polyelectrolyte layer showing charge reversal..... 83
- Figure 5.7:** FITC labelled HNTs coated with natural polyelectrolytes (5 ug/mL); DAPI staining of CRL-2303; Merged image of FITC and DAPI shows localization of HNTs in or on the nuclei. Images were taken 120 hr after addition of FITC labelled HNTs coated with natural polyelectrolytes to CRL-2303 cells. Scale bar = 50 um. 85
- Figure 5.8:** Effect of 1 ug/mL concentration of HNT, CPT, HNT-CPT, and Nat LbL HNT-CPT on CRL-2303 cells after 24 hr (top) and 96 hr (bottom). Images shown are representatives of multiple wells (n = 3) and multiple platings of cells for each condition tested. Scale bar = 100 um. 86
- Figure 5.9:** Effect of 5 ug/mL concentration of HNT, CPT, HNT-CPT, and Nat LbL HNT-CPT on CRL-2303 cells after 24 hr (top) and 96 hr (bottom). Images shown are representatives of multiple wells (n = 3) and multiple platings of cells for each condition tested. Scale bar = 100 um. 86
- Figure 5.10:** Viability assay of the long-term sustained release of anticancer drug (camptothecin) from encapsulated HNTs coated with natural polyelectrolytes using LbL technique in glioma cells..... 87
- Figure 6.1:** Panel (a) Cellulose matrix at the macroscale, showing from left to right, cellulose biohybrids incorporating CuHARS, Fe₂O₃NPs/CuHARS, and cellulose alone, respectively. The 3rd sample (rightmost sample) is a fragment of the constructed cellulose matrix alone. Metric scale below the matrix discs indicates diameter of approximately 2 cm for each disc. Panel (b) Cellulose matrix sample incorporating susceptible Fe₂O₃NPs/CuHARS suspended by a permanent bar magnet. . 93
- Figure 6.2:** Incorporation of cellulose with CuHARS. Blue arrows indicate CuHARS (dark and straight structures), and yellow arrowheads indicate cellulose fibers (light, curved structures). Image obtained using inverted light microscopy. Scale bar = 50 um. 94
- Figure 6.3:** Cellulose films testing with cells in defined microenvironments. Cellulose matrix materials alone were tested for compatibility with cell culture conditions. The bottom portion of the image shows the cellulose matrix and top portion shows brain tumor cells. Blue arrowheads indicate cellulose fibers and stars indicate edges of glioma cells. Scale bar = 50 um. 96

- Figure 6.4:** Cellulose films testing with cells in defined microenvironments. Cellulose-CuHARS biohybrids. The bottom portion shows the cellulose-CuHARS matrix and the top portion shows glioma cells with some released CuHARS. To evaluate integration into the matrix of smaller size biohybrids, CuHARS were sonicated as previously described [120] before they were combined with cellulose. White arrows indicate CuHARS and stars indicate edges of glioma cells. Scale bar = 50 μm 96
- Figure 6.5:** Cellulose-CuHARS- $\text{Fe}_2\text{O}_3\text{NPs}$ biohybrids. Bottom portion shows the cellulose-CuHARS- $\text{Fe}_2\text{O}_3\text{NPs}$ matrix and top portion shows glioma cells with some released CuHARS. For these integrated hybrids, CuHARS were not sonicated before mixing with cellulose. Therefore, some very long CuHARS were successfully integrated into the cellulose matrix, as indicated. Blue arrows indicate CuHARS and stars indicate edges of glioma cells. Scale bar = 50 μm 97
- Figure 6.6:** Phase contrast microscopy images of a co-culture experimental model with 1:3 ratio of glioma cells and normal brain astrocytes at 3, 24, 48, and 72 hr timepoints. Scale bar = 100 μm 98
- Figure 6.7:** Phase contrast microscopy image of a co-culture of normal brain astrocytes and glioma cells with 1 $\mu\text{g}/\text{mL}$ concentration of sonicated CuHARS at 3, 24, 48, and 72 hr timepoints. Scale bar = 100 μm 99
- Figure 6.8:** Bright field microscopy image of a co-culture of normal brain astrocytes and glioma cells with 1 $\mu\text{g}/\text{mL}$ concentration of sonicated CuHARS (yellow arrows) at 3, 24, 48, and 72 hr timepoints. Scale bar = 100 μm 100
- Figure 6.9:** Phase contrast microscopy image of a co-culture of normal brain astrocytes and glioma cells with 5 $\mu\text{g}/\text{mL}$ concentration of sonicated CuHARS at 3, 24, 48, and 72 hr timepoints. Scale bar = 100 μm 101
- Figure 6.10:** Bright field microscopy image of a co-culture of normal brain astrocytes and glioma cells with 5 $\mu\text{g}/\text{mL}$ concentration of sonicated CuHARS (yellow arrows) at 3, 24, 48, and 72 hr timepoints. Scale bar = 100 μm 102
- Figure 6.11:** Phase contrast microscopy image of a co-culture of normal brain astrocytes and glioma cells with 10 $\mu\text{g}/\text{mL}$ concentration of sonicated CuHARS at 3, 24, 48, and 72 hr timepoints. Scale bar = 100 μm 103
- Figure 6.12:** Bright field microscopy image of a co-culture of normal brain astrocytes and glioma cells with 10 $\mu\text{g}/\text{mL}$ concentration of sonicated CuHARS (yellow arrows) at 3, 24, 48, and 72 hr timepoints. Scale bar = 100 μm 104
- Figure 6.13:** Total area covered by 1, 5, and 10 $\mu\text{g}/\text{mL}$ sonicated CuHARS at 3, 24, 48, and 72 hr timepoints. 105
- Figure 6.14:** Total number of objects covered by 1, 5, and 10 $\mu\text{g}/\text{mL}$ sonicated CuHARS at 3, 24, 48, and 72 hr timepoints. 106

Figure 6.15: Size distribution of 1 ug/mL sonicated CuHARS at 3, 25, 48, and 72 hr.	107
Figure 6.16: Size distribution of 5 ug/mL sonicated CuHARS at 3, 24, 48, and 72 hr.	108
Figure 6.17: Size distribution of 10 ug/mL sonicated CuHARS at 3, 24, 48, and 72 hr.	109
Figure 7.1: Schematic diagram of interaction of non-degradable and degradable biomaterials with brain cells and their outcome features.....	113
Figure F.1: An example to import an image to Image Pro-Plus 7.0 to calculate the area of β -gal staining.....	132
Figure F.2: An example to apply mask to the image to calculate the area of β -gal staining.....	132
Figure F.3: An example to export the data to Excel spreadsheet using Image Pro Plus version 7.0.....	133

LIST OF TABLES

Table 2.1: Chemical properties of glutamate	22
Table 2.2: Chemical properties of choline chloride	31
Table 3.1: Total area of the image covered by different densities of gliomas (CRL-2303) and astrocytes at 3 days <i>in vitro</i> (div) (in %).....	46
Table 5.1: Analysis of total number of objects, average area, average roundness, and Nuclear Area Factor (NAF) (n = 6) for microglial cells treated with nanofilms made of CuNps and various concentrations of STS.	81

ACKNOWLEDGMENTS

I would like to express my gratitude towards all those who made it possible for me to complete this dissertation. I reserve my first and foremost acknowledgement for my advisor, Dr. Mark A. DeCoster, for supporting me throughout my doctoral research. His valuable advice, constant encouragement and guidance immensely contributed to my professional advancement. I would like to thank Dr. Steven Jones, Dr. Teresa Murray, Dr. Yuri Lvov, and Dr. Pedro Derosa for their patience and willingness to be part of my advisory committee.

I would like to thank each member of my research group for their help and cooperation throughout this work. Special thanks to Nam Nguyen and Zach Norcross for their suggestions and positive comments. I want to mention Kahla St. Marthe, Neela Prajapati, Elnaz Khezerlou, Anik Karan, and Kyle Rugg for being wonderful labmates. I would also like to thank Dr. Margarita Darder, visiting scientist from Spain, for teaching me the techniques for cellulose preparation. Her guidance, insight and helpful discussions laid the foundation of a whole new set of experiment with cellulose fibers. I would like to acknowledge Dr. Jessica L. Scoggin, Chao Tan, Dr. Prabhu Arumugam and Dr. Teresa Murray for our insightful discussions during our collaboration.

I would like to acknowledge Dr. James Spaulding and Emily Born for their generous help and support.

I would also like to thank Dr. Raghuvara Yendluri, Dr. Renata Minullina, and Dr. Lvov for their collaboration and willingness to make me a part of their research work.

I would like to express my wholehearted gratitude to my friends for their support and encouragement throughout my studies at Louisiana Tech University. Lastly, I have no words to express how grateful I am for my parents and family members without whose support and blessings I would not have achieved anything in my life. I would also like to apologize every member of my family for not being able to be with them all these years.

CHAPTER 1

INTRODUCTION

1.1 Motivation

Brain tumors account for almost 90% of all central nervous system (CNS) tumors. Brain tumors are different from other tumors because they rarely spread to distant organs. However, they can also grow and metastasize to neighboring areas, thereby destroying normal brain cells. The brain tumor microenvironment consists of a network of various cell types such as microglia, endothelial cells, cancer cells, and astrocytes [1]–[3]. **Figure 1.1** shows the schematic representation of some major cell types that comprises tumor microenvironment in the brain.

Co-culture systems are widely used to study cell-cell interaction between two, or more populations of cells. Hurst *et al.* [4] co-cultured immortalized vascular endothelial and C6 glioma cells to study cell-cell interactions and found that endothelial cells exhibited changes in morphology that occurred only in the presence of glioma cells. The advantage of co-culture systems is that they mimic the *in vivo* models, however, it is complicated to achieve a stable system because of the varying growth rate of the different populations of cells. Additionally, two populations of a co-culture system form a co-operative relationship whereas more than two populations may be challenging [5].

Gliomas are the most aggressive primary tumors in the brain. Astrocytes, star-shaped normal glial cells in the brain, play a major role in tumor pathogenesis. Gliomas

are the result of malignant transformation of astrocytes [6]. During a diseased state of the brain such as cancer, both cancer cells and healthy brain cells such as astrocytes are present. In a brain tumor microenvironment, malignant cancer cells and astrocytes communicate with each other through gap junction [2]. Studies have shown that astrocytes themselves may become transformed into various types of brain tumors, including gliomas [7].

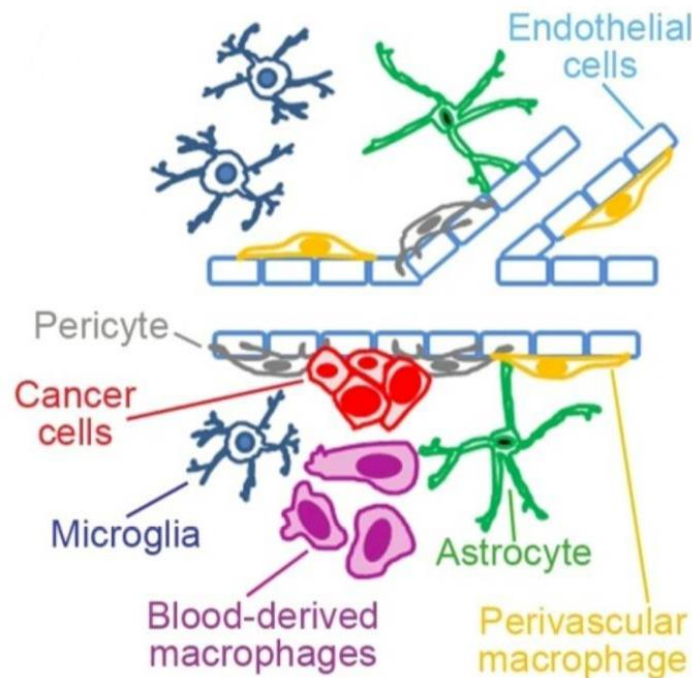


Figure 1.1: Schematic diagram of some major cell types that comprises tumor microenvironment in the brain [8].

In this research, a mixed co-culture experimental setup comprised of glioma cells and normal brain astrocytes was created to mimic a brain tumor microenvironment. This experimental model will provide an excellent platform to understand the interaction between two heterogeneous population of cells. Moreover, this co-culture experimental

model will expand our knowledge in studying the dynamic relationship between glioma cells and normal brain astrocytes. It will further elucidate mechanisms that lead to glioma proliferation in a brain tumor microenvironment. However, because the two cell types grow at different rates, the cell microenvironment must be set up with different ratios of cells for a stable co-culture system. Additionally, whereas a stain for Glial Fibrillary Acidic Protein (GFAP) can be used to visualize glial cells in a single cell system, further staining is needed in a co-culture model because GFAP is expressed by numerous cell types in the CNS, including astrocytes and glioma cells [9], [10]. Thus, another staining called β -galactosidase (β -gal) will be employed, in addition to GFAP stain to distinguish between the normal brain cells and brain tumor cells. β -gal, which is widely used to demonstrate specific gene expression, stains only the glioma cells in our model [11]. Further, possibility to identify cell types according to the size of the nuclei will be considered in a co-culture experimental model.

Glutamate is a major excitatory neurotransmitter in the brain. Jacobs *et al.* [7] showed that astrocytes have increased glutamate uptake in comparison to glioma cells whereas glioma cells release glutamate, thus promoting the growth of glioma [12]. Prakash *et al.* [13] have reported that epileptic seizures are prevalent among patients with glial tumors. However, little has been explored in studying the uptake of glutamate in co-culture of glioma cells and normal brain astrocytes. Glutamate uptake studies in co-culture are important to understand how glutamate is regulated in the brain during diseased state. Thus, glutamate uptake will be analyzed in the co-culture experimental model using a quantitative colorimetric detection kit.

1.2 Objectives

In a diseased state of the brain such as cancer, the behavior of the cells is modified by the interaction between healthy and normal cells (i.e. between tumor cells and normal brain astrocytes). The objective of this research is to create a mixed co-culture of normal brain astrocytes and brain tumor cells to mimic brain tumor microenvironment and study cell-cell interactions. This will further reveal the mechanisms of tumor invasion in a co-culture model and elucidate tumor progression. Glutamate must be present in the right concentrations, in the right places, for the right amount of time in the brain. Glutamate can be toxic if its concentration is too high in the brain. Next, glutamate uptake will be studied in individual as well as mixed cultures. Morphology of astrocytes were observed by blocking the sodium-dependent transporters which are responsible for glutamate uptake from the extracellular environment. Additionally, brain cell microenvironment was modified using different engineered micro/nanomaterials. This will help answer questions such as how glutamate is regulated in the brain and give us ideas to generate and modify brain cell microenvironment. Furthermore, potential applications of a novel biohybrid material CuHARS will be explored and degradation of sonicated CuHARS will be investigated. The following experiments were developed to test the following hypotheses:

Hypothesis 1

A mixed co-culture experimental model is useful to study the interactions between normal brain astrocytes and glioma cells. We further hypothesize that tumor cells invade the surrounding area in a co-culture experimental model.

Hypothesis 2

A co-culture experimental model is used to study glutamate uptake in a brain tumor microenvironment. Furthermore, the presence of glioma cells will affect the rate of uptake of glutamate by normal astrocytes.

Hypothesis 3

Engineered micro/nanomaterials can be used to modify brain cell microenvironments. This modification will result in apoptosis or necrosis of the cells (altered growth).

Hypothesis 4

CuHARS can be incorporated with cellulose to a construct stable matrix for delivery to cells.

1.3 Dissertation Overview

Chapter 1 provides the motivation, objectives for the project, and an overview of the dissertation. Chapter 2 provides background and literature review on relevant research work involving a major excitatory neurotransmitter, glutamate, glutamate transporters, the glutamate-glutamine cycle, and *in vitro* co-culture methods. Chapter 3 describes development of a mixed co-culture model consisting of glioma cells and astrocytes to engineer the tumor microenvironment and study whether glioma cells manipulate astrocytes to increase their invasiveness. Chapter 4 outlines glutamate uptake in normal brain astrocytes and glioma cells (CRL-2303) individually as well as in a co-culture model. Chapter 5 talks about new approaches to modify brain cells using engineered nanomaterials to regulate glutamate in the brain. Chapter 6 portrays the potential applications of a novel biohybrid material named as CuHARS such as its incorporation to a non-degradable material for drug delivery and degradation of sonicated CuHARS in a co-culture model.

CHAPTER 2

BACKGROUND AND LITERATURE REVIEW

2.1 Gliomas

Gliomas are brain tumors that originate from glial cells, the most abundant cell types in the central nervous system (CNS). Gliomas account for 70% of the brain tumors and are the most common and aggressive primary tumors often diagnosed in older adults [14].

Gliomas can be low grade (slow growing) or high grade (fast growing). The symptoms of glioma are headaches, seizures, problems with speech, memory loss, physical weakness, and personality changes among others. The treatment for a glioma depends on its grade and may include surgery, radiation therapy, or chemotherapy.

CNS tumors are classified into Grades I through IV [15]:

Grade I tumors are also called Pilocytic Astrocytoma. They are slow growing and benign tumors. They are more common in children than adults. They occur in the cerebellum or brain stem, and sometimes in the cerebral hemispheres. Most are highly treatable and curable.

Grade II tumors are also known as Low-grade Astrocytoma and are slow. They rarely spread to other parts of the CNS. Grade II gliomas are most common in young adults aged between 20 to 50. They can either be benign or malignant.

Grades III are also known as Anaplastic Astrocytoma. These tumors grow faster and are more aggressive than Grade II Astrocytomas and can invade neighboring tissue. They are more common in men than women.

Grade IV tumors are also called Glioblastoma Multiforme (GBM). They are the most common primary brain tumor. GBM usually spreads quickly and invades other parts of the brain. They are most common in older people and less common in children and can recur after initial treatment. GBM is the most lethal form of brain cancer.

2.2 Astrocytes

Astrocytes are the most abundant glial cells in the CNS [10], [16], [17]. The astrocytes resembles a star, hence they are also known as star-shaped cells [18]. They perform numerous functions in the brain including removal of glutamate from the extracellular compartment, metabolic support, free radical scavenging, water transport, and maintaining homeostasis [17], [19]. Two basic types of astrocytes exist, fibrous (in white matter) and protoplasmic (in grey matter), as shown in **Figure 2.1** [20], [21]. The two types of astrocytes differ in the density, length, and surface area of their processes.

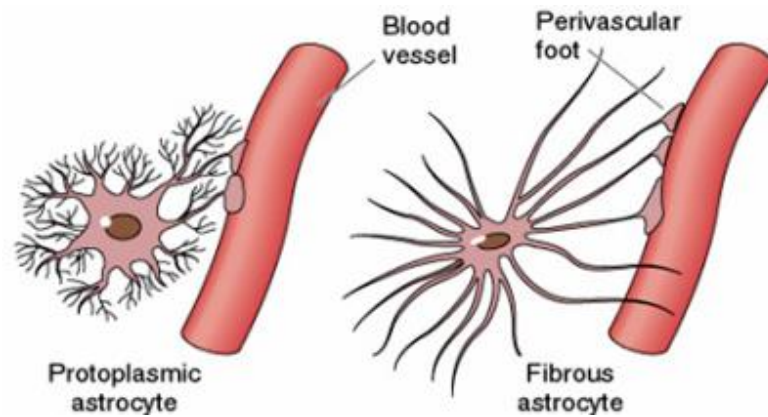


Figure 2.1: Major types of astrocytes

2.3 Cells

2.3.1 CRL-2303 Glioma Cell Line

The CRL-2303 (C6/lacZ7) cell line is derived from the C6 cell line (N-nitrosomethylurea induced glial rat). The cell line expresses the lacZ gene: E. coli derived beta-galactosidase. The glioma cell line produces beta-galactosidase (β -gal), and when treated with an organic compound called X-Gal, produces an insoluble blue product called 5,5'-dibromo-4,4'-dichloro-indigo and stains the glioma cells indigo blue color. This characteristic allows the cells to be visualized once they are stained and facilitate image analysis by differentiating the glioma cells from normal brain astrocytes in co-culture studies [22]. They are a naturally adherent cell line with a fibroblast like morphology. **Figure 2.2** shows images of CRL-2303 cell line *in vitro*. **Figure 2.2 (a)** shows CRL-2303 cell line pre X-gal treatment, and **Figure 2.2 (b)** shows the same cells post X-gal treatment, with indigo blue staining.

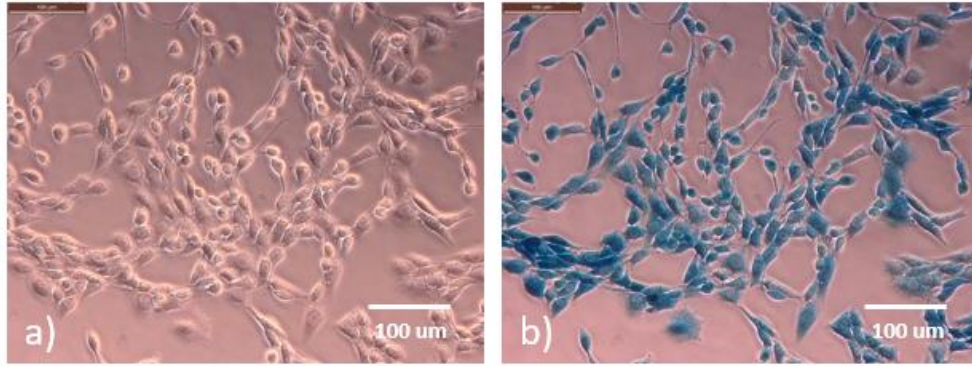


Figure 2.2: Phase contrast microscopy of CRL-2303 glioma cell line a) Pre X-gal treatment b) Post X-gal treatment. Scale bar = 100 µm.

2.3.2 Rat Astrocytes

Rat astrocytes can be derived from primary, newborn rat (Sprague/Dawley) brain cortices. They have broad flat morphology and they are adherent cells. They express glial fibrillary acidic protein (GFAP), an intermediate filament protein that is specific to astrocytes in the nervous system [23]. **Figure 2.3** shows representative images of the rat astrocytes *in vitro*. **Figure 2.3 (a)** shows normal astrocytes, and **Figure 2.3 (b)** shows the same cells, stained for GFAP. Negative controls for specificity of staining will be shown later in this dissertation.

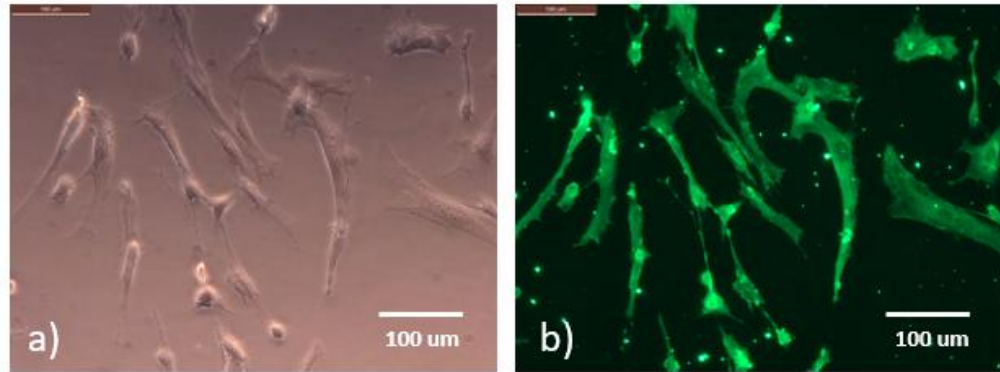


Figure 2.3: Rat Astrocytes a) Phase contrast microscopy before GFAP staining b) Fluorescence microscopy after GFAP staining. Scale bar = 100 μm .

2.4 Co-culture

Co-culture is a technique to grow two or more distinct cell types in a culture dish [24] with some degree of contact between them. Co-culture approaches provide an excellent model for studying cellular interactions between two or more different populations of cells. Some cell types may act differently when cultured in a different environment as opposed to their original growth condition [25]–[27]. A single cell type may not accurately represent the physiological relevance in *in vivo* studies especially in the brain [5], therefore a mixture of cells will allow for studying heterotypic cell-cell interactions. Moreover, in some cases, the presence of more than one type of cell might improve the cultivation as they exhibit *in vivo* physiological behavior [28]–[30]. Hence, a co-culture set-up is beneficial for studying cell-cell interactions, and engineering complex systems composed of multiple cell types. For example, immortalized human umbilical vein endothelial cells (HUVEC-304) when co-cultured with rat C6 glioma cells creates a barrier very similar to blood-brain barrier that is not generated in the absence of glioma cells [4]. However, creation of a co-culture experimental model can be complicated with

each cell type behaving in a specific manner with different growth rates. Usually, co-culture set-ups with two cell populations are predictable and form a stable system whereas more than two cell populations tend to lead to a more chaotic cell growth [31]. For example, Hatherell *et al.* [32] carried out a three-dimensional mono-, bi- and tri-culture models of the blood-brain barrier and concluded that a bi-cultivation model was the most successful among all. Another important factor to be considered for co-culture model is the selection of a growth media that best suits all the types of cells [5], [33].

Depending on the ultimate application of co-culture, the experimental set-up for a two-dimensional *in vitro* co-culture model can be divided into two modes as shown in

Figure 2.4;

- 1) with cell-cell contact; where the population of cells are mixed
- 2) without cell-cell contact; where the populations of cells are partially separated

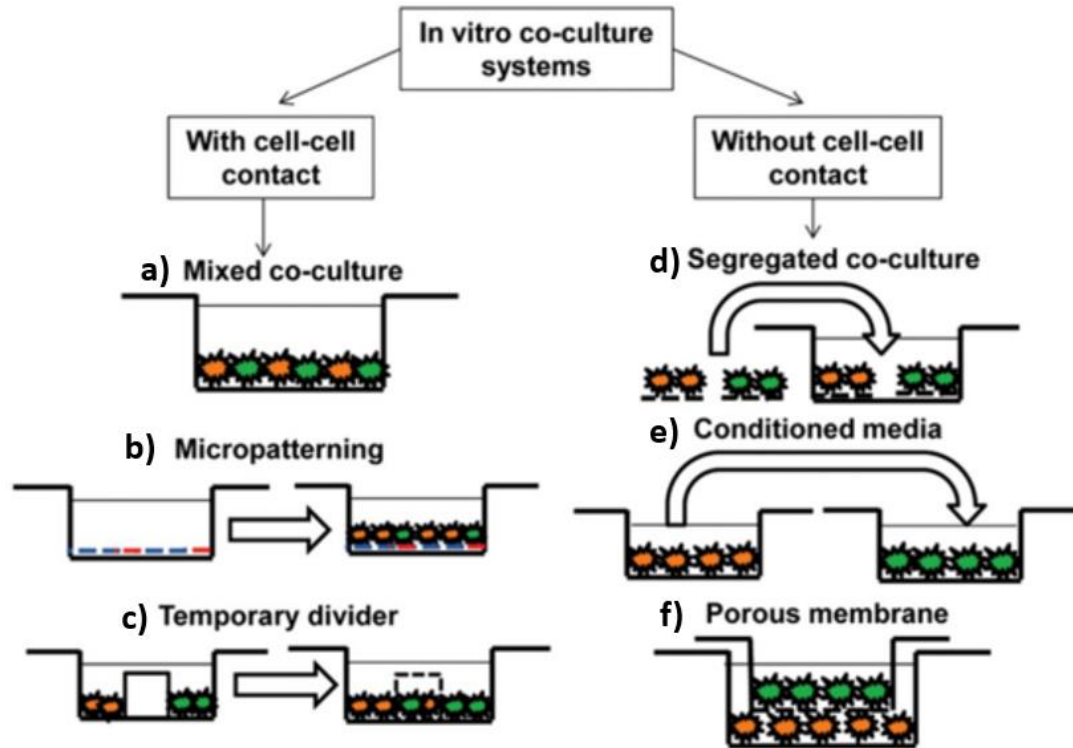


Figure 2.4: Schematic of a two-dimensional *in vitro* co-culture systems to evaluate cell-cell interactions a) Mixed co-culture; b) Micropatterning; c) Temporary divider; d) Segregated co-culture; e) Conditioned media; f) Porous membrane [34].

2.4.1 Cultures with Cell-cell Contact

2.4.1.1 Mixed co-culture

In a mixed co-culture (**Figure 2.4 a**), at least two equal or different population of cells of interest are kept together such that they are in contact with each other forming a monolayer of cells. Mixed co-culture is one of the simplest co-culture methods where the cell suspensions of the cell populations of interest are combined at the desired co-culture ratio. The seeding densities of each cell population can be adjusted accordingly [34]. One type of cell population can be seeded directly with the monolayer of another cell population. If the two cell populations are similar, supplementary growth factors can be

used. However, in case of two distinct cell populations, the selection of appropriate growth media is required. Guguen-Guillouzo *et al.* [35] showed that the mixed co-culture of adult rat hepatocytes with another liver epithelial cell type improved the maintenance and reversibility of active albumin secretion.

2.4.1.2 Micropatterning

In a micropatterned experimental set-up (**Figure 2.4 b**), contact between cell populations is allowed but controlled by a surface pattern. Micropatterning can be done on glass or plastic substrates. This technique offers a great potential for generating different patterns shapes and sizes, and controlling the organization of co-cultures spatially [36]. The outcome of the culture depends on the type of micropattern as it will determine diffusion rates and level of separation or contact between cell populations. Fukuda *et al.* [37] applied layer-by-layer technique to create micropatterned cellular co-cultures that included three extracellular matrix components: hyaluronic acid, fibronectin, and collagen.

2.4.1.3 Temporary divider

A temporary divider (**Figure 2.4 c**) is used as a physical barrier between different cell populations and can be removed afterwards to permit cell migration and physical contact. A temporary divider will help to control cell-cell contact along with spatial and temporal cell seeding pattern. In addition, this technique allows the manipulation of heterotypic and homotypic interactions of cell populations; however, it is a bit challenging as the individual cell compartments need to be completely sealed. Furthermore, the properties of the divider determine the cell response and soluble factor interactions. Wang *et al.* [38] employed a hydrogel insert as a divider for 7 days to

separate fibroblasts and osteoblasts. They demonstrated the migration of fibroblasts and osteoblasts into the interface region and proved that this co-culture model served as an excellent representation for studying the mechanism of formation of soft tissue-to-bone interface.

2.4.2 Cultures without Cell-cell Contact

2.4.2.1 Segregated co-culture

A segregated co-culture (**Figure 2.4 d**) is usually employed by forming individual monolayers of desired cell types in their own environment on tissue culture coverslips to prevent cell-cell contact and putting them together in the same environment later. The advantage of this technique is that it is possible to analyze the response of the subpopulation of cells in co-culture. However, this technique might be laborious as it requires a multi-stage cell seeding procedure. Also, long term physical contact between the cell populations cannot be prevented as the cells eventually migrate, forming a heterogeneous culture on the coverslips [34]. D'andrea *et al.* [22] used this approach to determine the interactions between chondrocytes and synovial cells.

2.4.2.2 Conditioned media

In conditioned media co-culture (**Figure 2.4 e**), the culture media of one cell type is introduced into the culture of another type. Conditioned media studies help to detect soluble factor effects in co-culture media. A drawback of this method is deficiency of nutrition in one of the cell types as it obtains conditioned media instead of their own growth media [34]. The cells must adapt to a new environment with different growth supplements. This method can be advantageous for some cell types such as fibroblasts, osteoblasts and bone marrow stromal cells as reported by Wang *et al.* [39].

2.4.2.3 Porous membrane

Indirect co-cultures that use porous membranes (**Figure 2.4 f**) to keep the different cell populations physically, but not chemically apart have shown promising results *in vitro*. The membrane which acts as a physical barrier can be made of a transparent film and allows light to pass through so that cells at both the bottom well plate and insert are visible through light microscope. The porous membrane is usually made of polyester and the pore size and pore density can be selected according to the application [24]. The pore density allows for diffusion of molecules across the membrane and the exchange of soluble factors [40]. One of the benefits of porous membrane insert co-culture systems, over other methods is bi-directional signaling between the cell populations. In addition, cellular changes can be detected on a population-specific basis [41]. Snow *et al.* [42] investigated the paracrine signaling between ovarian cancer cells and fibroblasts using porous tissue culture inserts.

2.5 Co-culture of Astrocytes and Gliomas

A co-culture of rat brain astrocytes and gliomas represents a good experimental model for resembling tumor microenvironment as gliomas are a type of brain tumor derived from malignant transformation of astrocytes [43]. Since the growth rate of these two different cell types varies [44], optimization of population ratios is important so one cell type does not monopolize the culture [5], [45]. Astrocytes become reactive when they are around glioma cells, further justifying the prospect of glioma-astrocyte interactions [44], [46]. Gagliano *et al.* [43] reported that astrocytes interact with glioma cells via gap junctions and growth factors. Moreover, glioma cells are known to produce factors which in turn causes astrocytes to produce matrix metalloproteinase-2 (MMP-2),

an enzyme involved in the breakdown of extracellular matrix (ECM). Further, ECM degradation causes glioma cells to proliferate by converting pro-MMP-2 to its activated form [47]. Hence, in a co-culture model with rat brain astrocytes and glioma cells, the later abnormal cancer cells create an environment where they can thrive, ultimately increasing their own invasiveness [44], [47].

Figure 2.5 is a schematic diagram of normal rat brain astrocytes alone, gliomas alone, and normal rat brain astrocytes and gliomas when they are put together.

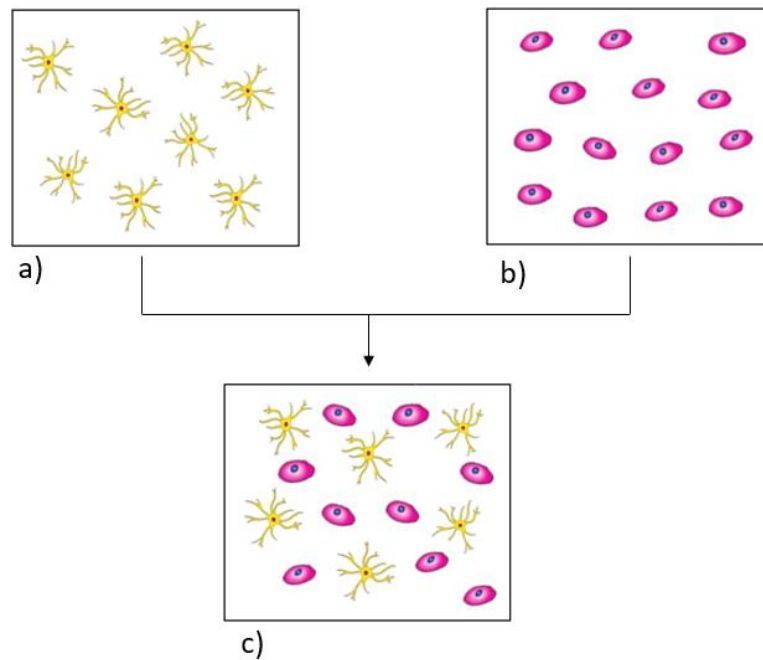


Figure 2.5: Schematic representation of a) normal rat brain astrocytes; b) glioma cells (CRL-2303); c) co-culture of normal rat brain astrocytes and glioma cells.

According to Gullotta *et al.* [48], GFAP is considered as a glial-specific protein rather than astrocytic-specific. GFAP is visualized in all grades of gliomas. Some authors have indicated an inverse relationship between the degree of malignancy and the intensity

of GFAP expression, while others have reported that no correlation exist between malignancy and GFAP expression [9], [49]. β -gal has been widely used to stain only the glioma cells [22].

2.6 Neurotransmitters

Neurotransmitters are chemical messengers that transmit signals from a neuron to another neuron or other target cell across a chemical synapse. Most of the neurotransmitters are the size of a single amino acid, but some are the size of larger proteins or peptides. After neurotransmitters are synthesized in the presynaptic neuron, they are packaged and stored in synaptic vesicles [50]. When the threshold action potential is reached, they are released by an active transport mechanism known as exocytosis into the synaptic cleft [50], [51]. After they are released into the synaptic cleft, they bind with neurotransmitter receptors in the postsynaptic terminal [52]. The interaction between a neurotransmitter and its receptor is often explained by “lock and key” model [53]. The receptor which acts as a “lock” can only be activated by a neurotransmitter which acts as a “key” if it fits perfectly into the “keyhole” (neurotransmitter binding site) of the lock. Most of the neurotransmitters can bind to and activate more than one type of receptors. However, an electrical signal (action potential) is necessary to release a neurotransmitter.

Figure 2.6 is a schematic representation of a chemical synapse through which signals are transmitted from one neuron to another.

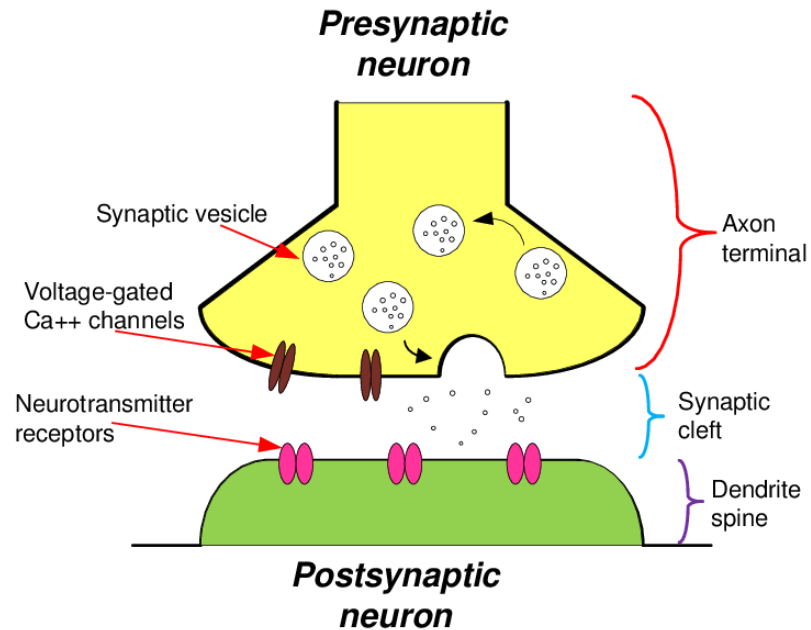


Figure 2.6: Schematic representation of a chemical synapse [54].

Neurotransmitters that excite other neurons when released and that trigger action potentials are known as excitatory neurotransmitters. Neurotransmitters that inhibit the generation of action potentials are known as inhibitory neurotransmitters. Some neurotransmitters can both excite and inhibit action potentials. **Figure 2.7** shows the classification of neurotransmitters as excitatory properties, inhibitory properties, or both.

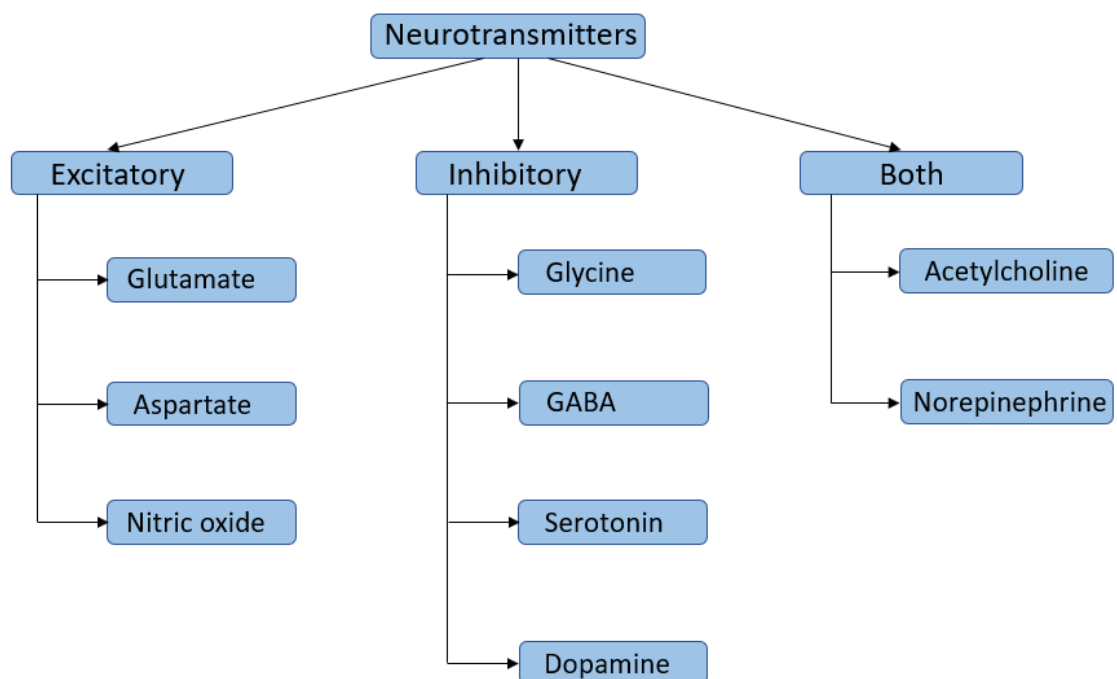


Figure 2.7: Classification of Neurotransmitters

2.6.1 History of the Discovery of Neurotransmitters

Acetylcholine, which acts as both excitatory and inhibitory neurotransmitter, was one of the first neurotransmitters discovered in 1921 [55], [56]. Otto Loewi and Henry Dale received the Nobel Prize in Physiology or Medicine in the year 1936 for their experiments with acetylcholine. Another neurotransmitter, norepinephrine, which falls under the same category, was discovered in 1946 [55]. In 1950, dopamine, an inhibitor which plays a major role in controlling brain's reward and pleasure centers, was discovered [57]. In 1950, Eugene Roberts discovered GABA as an inhibitory neurotransmitter [58]. In 1960, serotonin was found to be present in the brain, but at the time, it was not considered as a neurotransmitter. In 1995, Bernard Steve Brodie used a special fluorometric assay to study serotonin in the brain. In 1950s, Robert Furchgott

demonstrated that nitric oxide can act as a “messenger molecule” in controlling the dilation of blood vessels [59]. The role of glycine as a neurotransmitter emerged in 1965 when Aprison and Werman found out that the concentration of glycine is higher in the spinal cord tissue. The advent of glutamate as a neurotransmitter was not discerned until the early 1980s [60], although the role of glutamate in metabolism was well-known [61]. Hayashi conducted experiments with sodium glutamate and observed convulsions in mammals, such as dogs, monkeys, and men with excess glutamate. He later concluded that glutamate was a neurotransmitter in the mammalian CNS [62].

2.6.2 Fate of a Neurotransmitter

Neurotransmitter released at a synapse, must be removed by one of four processes:

1. Binding to its receptor on the postsynaptic neuron leading to the generation of an action potential.
2. Enzymatic degradation by enzymes in the synaptic cleft on the plasma membrane of both the neurons. For example, acetylcholinesterase breaks down acetylcholine.
3. Reuptake by active transport, being taken back up into the presynaptic neuron (recycled), which is the most common fate.
4. Diffusion i.e. loss into the extracellular fluid (ECF).

Figure 2.8 shows the schematic representation of the fate of neurotransmitter after it is released.

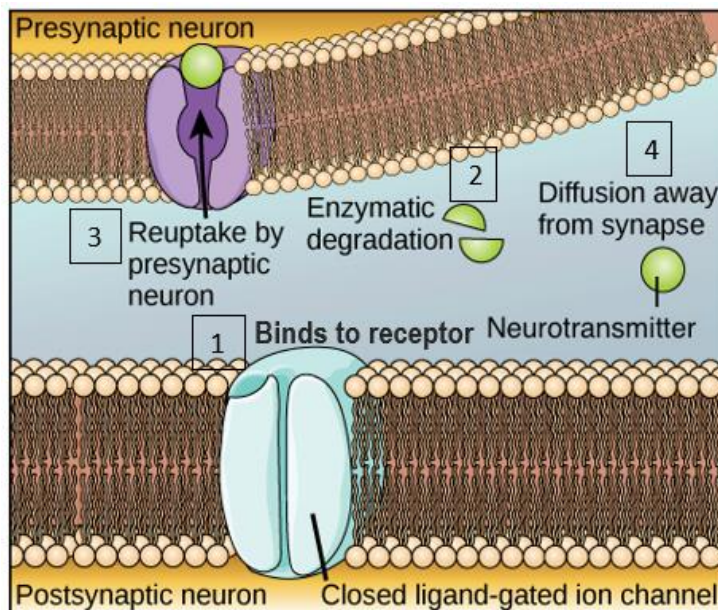


Figure 2.8: [Modified] Schematic representation of the fate of neurotransmitter after it is released [63].

2.7 Glutamate

Glutamate, an abundant amino acid [64] and a major excitatory neurotransmitter in the central nervous system [51], [65], [66] is crucial in learning and memory [61]. High concentrations of glutamate are present in the synaptic vesicles where they are stored as small packages in the mammalian brain [67]. However, the extracellular concentration of glutamate must be kept low [66], [68], [69] as excessive glutamate can cause a rise in Ca^{2+} and excitotoxicity [24], [70] wherein the neurons become too excited, leading to nerve damage or death [51], [66]. The intracellular glutamate concentration is generally three orders of magnitude higher than the extracellular concentration [27] [50], [71]. High levels of glutamate have been linked to neurological disorders such as seizures, autism, multiple sclerosis. Glutamate is cleared from the synapse by active transport mechanisms [70].

2.7.1 Chemistry of Glutamate

The properties of glutamate are shown in **Table 2.1**.

Table 2.1: Chemical properties of glutamate

Property	Value
IUPAC Name	Sodium 2-Aminopentanedioate
Molecular Formula	C ₅ H ₈ NO ₄ Na
Molar Mass	169.111 g/mol
Appearance	white crystalline powder
Solubility in water	740 g/L
Melting point	449.6°F

The chemical structure of glutamate is shown in **Figure 2.9**.

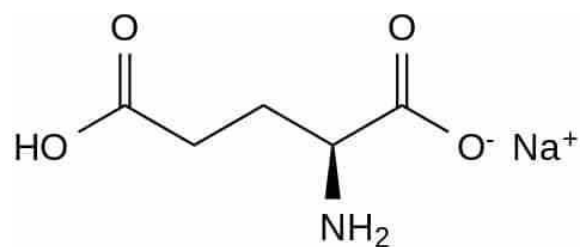


Figure 2.9: Chemical structure of Glutamate

2.7.2 Chemistry of Glutamine

The chemical structure of glutamine is shown in **Figure 2.10**.

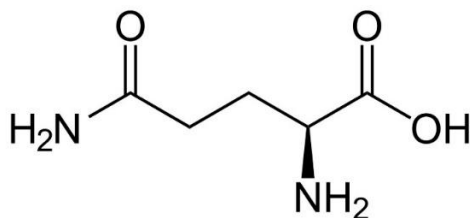


Figure 2.10: Chemical structure of Glutamine

2.7.3 Glutamate Receptors

Because glutamate receptor proteins are present on the cell surface, they are capable of being active only when triggered from the outside. However, activating too much glutamate receptors can cause excitotoxicity of neurons. Glutamate is released from the presynaptic terminal into the extracellular fluid, activating glutamate receptors [51]. The glutamate receptors are categorized as ionotropic and metabotropic receptors. N-methyl-D-aspartate (NMDA) receptors, AMPA (α -amino-3-hydroxy-5-methyl-4-isoxazole propionic acid) receptors/ kainate receptors falls under ionotropic receptors. Metabotropic receptors belong to subfamily C of G protein-coupled receptors (GPCRs) and are named as mGluR#1-8 [65], [71]. Most of the cells express a minimum of one type of glutamate receptor. Glutamate mediates excitatory neurotransmission by binding to one of the three families of glutamate receptors. During seizure, there is overexcitation of glutamate receptors.

2.7.4 Glutamate Transporters

Although there exist five subtypes of Na⁺ dependent glutamate transporters on both neurons and astrocytes [65], [66], [72], astrocytes are primarily responsible for the glutamate uptake in the brain [68]. Situated on the plasma membrane of neurons and glial cells, Na⁺ dependent glutamate transporters (**Figure 2.11**) are also known as Excitatory Amino Acid Transporters (EAATs) [73], [74]. EAATs are responsible for clearing glutamate by reuptaking from the synaptic cleft into neuronal and glial cells and terminating glutamatergic synaptic transmission, thus preventing glutamate spillover outside of the synapse [70], [72]. Glutamate neurotransmission must be terminated to prevent excitotoxicity by controlling the level of glutamate concentration in extracellular space [74], [75]. The five subtypes of Na⁺ dependent glutamate transporters characterized in humans are EAAT1-EAAT5 [73], [76]. Out of all the glutamate transporters, subtypes EAAT1 and EAAT2, also known as glutamate-aspartate transporter (GLAST) and glutamate transporter 1 (GLT-1) respectively, are primarily present in astrocytes, microglia, and oligodendrocytes (membranes of glial cells) [68], [77], [78]. They play a crucial role in maintaining low level of extracellular glutamate concentrations. The maximum glutamate reuptake (~90%) is achieved by EAAT2, thus preventing glutamate neurotoxicity [69], [79]. EAAT1 and EAAT3 (also known as excitatory amino acid carrier 1 (EAAC-1)) are widely present in the CNS whereas EAAT4 and EAAT5 are predominantly found in cerebellar Purkinje cells and retina, respectively [71], [73], [77], [80]. According to glutamate transport rates and anion currents, EAAT groups are classified into two groups: EAAT1-3 are the efficient glutamate transporters with small anion currents and EAAT4-5 are low capacity transporters with anion conductance [64].

Mim *et al.* [78] demonstrated that the rate of glutamate transport varies although the transport mechanism is same for all the glutamate transporters. The glutamate transporters EAATs 1-3 are 5-10 times faster than EAAT4.

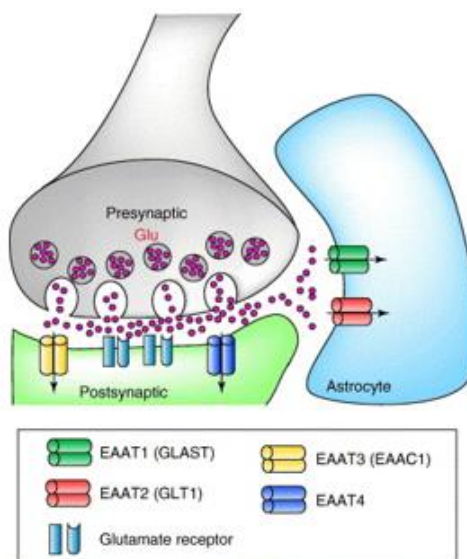


Figure 2.11: Schematics demonstrating sodium-dependent glutamate transporters (EAAT1-EAAT4) and glutamate receptor [81].

2.7.5 Low Affinity Transporters

Low affinity, high capacity transporter EAAT2 is the foremost glutamate transporters that comes into contact with presynaptically released glutamate. These low affinity transporters clear most of the glutamate release effectively until the glutamate concentrations are high and slow down when they get low. Therefore, the rate-limiting step is trapping of glutamate by the glutamate transporters whereas glutamate translocation comparatively does not take much time [78].

2.7.6 High Affinity Transporters

EAAT4 removes the glutamate molecules that were not uptaken by glial transporters and are capable of diffusing to a distant site (away from synaptic contacts). The primary purpose of EAAT4 is to inhibit the glutamate spillover to neighboring synapses and maintain the extracellular glutamate concentration at a submicromolar level. Due to its low glutamate uptake capacity, EAAT4 is not directly associated in terminating the synaptic transmission process. The rate of glutamate binding for EAA4 is one molecule in every 100 ms at 0.5 uM concentration [78].

2.8 Mechanism of Glutamate Removal

High concentrations of intracellular glutamate normally do not pose a threat whereas high extracellular concentrations of glutamate are harmful to neurons which might lead to nerve damage or death [66]. As a result, glutamate should be periodically cleared from the extracellular space to maintain low concentrations. Since no enzymes present in the synapse can metabolize glutamate, cellular uptake is the only method to remove glutamate extracellularly. The glutamate taken up by cells in the process of clearing from the extracellular fluid may be recycled for protein synthesis or energy metabolism. In nerve terminals, the glutamate taken up is reused as transmitter via glutamate-glutamine shuttle [82], [83]. Failure to uptake glutamate increases the level of glutamate in the extracellular fluid within a short period of time. The process of glutamate removal is carried out due to simple diffusion from the synaptic clefts. However, diffusion acts fast only over very short distances (only as far as a few hundred nanometers). The extracellular glutamate concentration outside synapses should be low

for effective synaptic removal mechanism via diffusion. However, concentrations of extracellular glutamate might rise under disease conditions [66].

2.9 Glutamate-Glutamine Cycle

The voltage gated sodium (Na^+) and potassium (K^+) channels generate action potential in the presynaptic neuron and neurotransmitters, such as glutamate, released from the synaptic vesicles (**Figure 2.12**). The uptake of glutamate by astrocytes is a negative feedback as it maintains the homeostasis in the brain. The glutamate is transported via glutamate transporters EAAT1 and EAAT2 and it is converted into glutamine using an enzyme glutamine synthetase. The glutamine is transported to the neurons where it is converted back to glutamate. This process is called the glutamate-glutamine cycle. However, the failure of astrocytes to take up glutamate, leads to the activation of AMPA and NMDA receptors in the postsynaptic neuron, and in turn to the overexcitation of neurons in the postsynaptic terminal which might lead to epileptic seizures and other abnormal conditions in the brain [84].

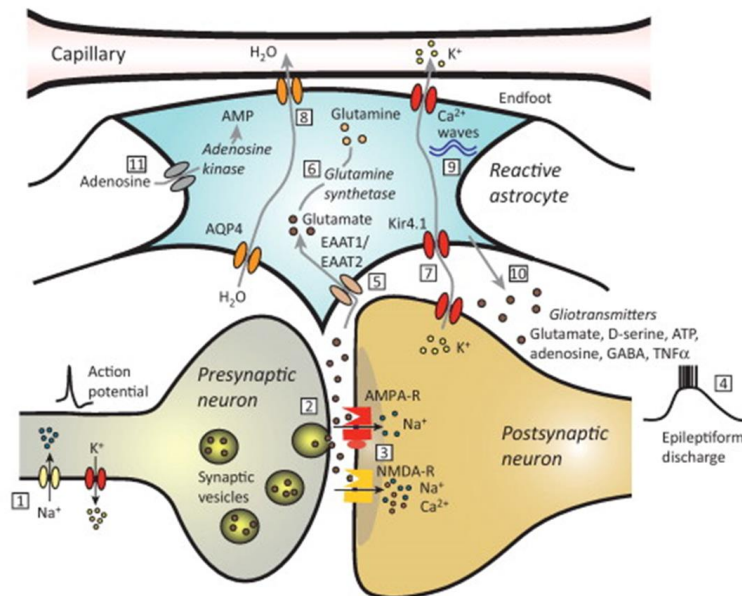


Figure 2.12: Schematic illustration of the release of neurotransmitters from the synaptic vesicles, glutamate-glutamine cycle, and generation of epileptic discharge [84].

2.10 Role of Glutamate in Epilepsy and Seizures

Excess levels of extracellular glutamate causes excitotoxicity leading to disease conditions such as seizures and epilepsy [66]. Epileptogenesis is a state caused due to seizures persisting for a long duration causing modifications to neuronal and glial expression of glutamate EAATs and receptors [85]. Glutamate released from the synapses, which act on ionotropic and metabotropic receptors, plays a key role in the initiation of seizure.

2.11 Gliomas and Excitotoxicity

Gliomas (brain tumors) are originated due to uncontrolled proliferation of glial cells, primarily from astrocytes [66]. Astrocytes uptake extracellular glutamate and maintain homeostasis in the normal brain [16], [68]. In contrast, glioma cells are unable

to uptake extracellular glutamate but instead further release glutamate which might overwhelm and kill the neurons, thereby resulting in seizures and other abnormal conditions in the brain [86]. Almost 80% of individuals that suffer from brain cancer experience at least one seizure during their life time [87]. Glioma cells are deficient in GLT-1, and GLAST is underexpressed in their plasma membrane due to mislocalization in the nuclei [66]. As a result, 50% of the glutamate transport is achieved by Na⁺-independent cystine-glutamate exchanger (system X_c⁻). The increased proportion of Na⁺-independent transport implies that Na⁺-dependent glutamate uptake is downregulated whereas Na⁺-independent system is upregulated in glioma cells [66]. This altered transport eventually leads to the accumulation of glutamate in the extracellular fluid and further causes excitotoxic neuronal death [88].

2.11.1 The Cystine/Glutamate Antiporter System (X_c⁻)

System X_c⁻ is a Na⁺-independent cystine-glutamate exchanger found in both astrocytes and gliomas, however it is upregulated in glioma cells. A cystine-glutamate exchanger releases glutamate in exchange for cystine being imported [89]. This cystine acts as a precursor for the synthesis of reducing agent glutathione (GSH), which is also an antioxidant. The imported cystine is then reduced to cysteine within the cell and released into the extracellular space as shown in **Figure 2.13**. The cysteine further oxidizes to cystine and again serves as a substrate for cystine-glutamate exchange [66]. In gliomas, almost half of the glutamate transport relies on Na⁺ independent cystine-glutamate exchange (x_c⁻) [66], [90]. Recent studies have shown that glioma cells release glutamate and causes excitotoxic neuronal cell death, thus creating more room for tumor expansion [90], [91].

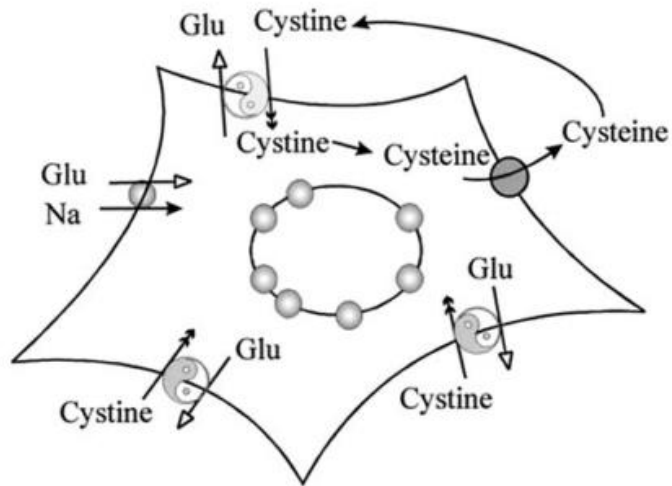


Figure 2.13: Xc⁻ system in glioma cells [66].

2.12 Mechanism to Block Sodium-Dependent Transporters

2.12.1 Locke's Solution

Locke's solution is an aqueous solution usually comprised of sodium chloride, calcium chloride, potassium chloride, sodium bicarbonate, and glucose adjusted to pH 7.4 [92]. Because Locke's solution lacks serum and phenol red, it is suitable for most fluorescence experiments as it eliminates auto-fluorescence or quenching.

2.12.2 Chemistry of Choline Chloride

The properties of choline chloride are shown in **Table 2.2**.

Table 2.2: Chemical properties of choline chloride

Property	Value
IUPAC Name	(2-Hydroxyethyl)trimethylammonium chloride
Molecular Formula	C ₅ H ₁₄ ClNO
Molar Mass	139.62 g/mol
Appearance	white or deliquescent crystals
Solubility in water	very soluble (>650 g/l)
Melting point	575.6°F (302°C)

The chemical structure of choline chloride is shown in **Figure 2.14**.

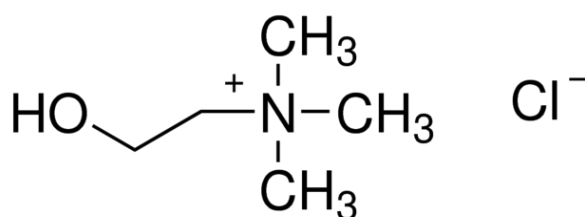


Figure 2.14: Chemical structure of choline chloride

Astrocytes uptake glutamate using sodium-dependent transporters. This sodium-dependent glutamate uptake mechanism can be blocked by removing extracellular sodium and replacing it with sodium-free medium. Glutamate uptake was carried out by

replacing sodium chloride with choline chloride in Locke's solution. Rosenberg *et al.* [93] found that in astrocyte-rich cultures, sodium replacement caused inactivation of sodium-calcium exchange, making them more sensitive to glutamate.

2.13 MTT Assay

The MTT assay can be used to evaluate the metabolic activity of cells. MTT [3-(4,5-dimethylthiazol-2-yl)-2,5-diphenyltetrazolium bromide] is yellow in color, and it is reduced to non-water-soluble purple formazan crystals in living cells as shown in **Figure 2.15**. After it is solubilized with organic solvent, the purple formazan product is dissolved and converted into a colored solution. The formazan product can be determined by using a spectrophotometry at 595 nm. MTT reduction is a measure of cellular metabolism which correlates to cellular toxicity. Only metabolically active cells reduce MTT to formazan product [94]. Ciapetti *et al.* [95] used the MTT assay to measure the compatibility of cells with different metals and polymers using MTT assay.

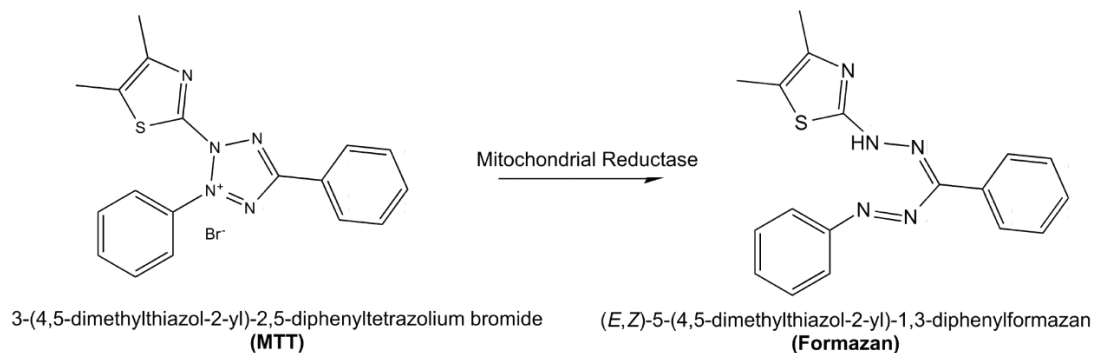


Figure 2.15: Reaction scheme for MTT reduction [96].

2.14 Apoptosis

Apoptosis, also known as programmed cell death, is a normal process that occurs in multicellular organisms for their development and continuation of life [97], [98]. Morphological changes during apoptosis include cell shrinkage, nuclear fragmentation, and chromatin condensation. Apoptosis can be initiated either through intrinsic or extrinsic pathway. Cell death is caused by activating caspases or enzymes that cause degradation of proteins. Morphological changes in cell culture caused by apoptosis can be visualized under microscope within few hr. Cell and nuclei shrinkage can be used as a measure to quantify the extent of apoptosis in culture using image analysis. Nuclear Area Factor (NAF) [99] can be a beneficial tool to quantify apoptotic cells and it is given by the product of area and roundness of the nuclei. NAF will be calculated in this project to evaluate apoptosis induced by staurosporine, an apoptotic agent.

2.15 Necrosis

Necrosis is a form of cell death caused by injury or other factors such as infection, toxins, or trauma [100]. Morphological changes during necrosis include cell swelling, plasma membrane rupture and loss of intracellular contents. Cellular leakage may cause an inflammatory response. In contrast to apoptosis, necrosis is uncontrolled cell death.

CHAPTER 3

USE OF A TWO-DIMENSIONAL *IN VITRO* CO-CULTURE MODEL WITH NORMAL BRAIN ASTROCYTES AND GLIOMA CELLS FOR ENGINEERING THE TUMOR MICROENVIRONMENT

3.1 Introduction

Gliomas are primary malignant brain tumors and they originate from neoplastic transformation of astrocytes [43], [66]. However, the mechanisms by which glioma cells migrate and invade healthy cells is yet to be understood [101]. The reactive astrocytes around the glioma cells suggests that these two cell types could be interacting [47], [102]. The mode of communication between the gliomas and normal brain astrocytes are thought to be via gap junctions and growth factors. Moreover, the mechanism underlying the role of gap junctions in the interaction of astrocytes with glioma cells and tumor invasiveness is yet to be explored [103].

The microenvironment for cancer, includes both tumor cells and healthy cells. A co-culture model is a useful system to study cell-cell interactions between different cell populations *in vitro*. Some cell types exhibit different behavior than their desired physiological behavior in the presence of another cell population. In some instances, the cell populations vary in their growth rates making one of the cell type dominant over the other [5]. Engineering a co-culture environment, where both tumor and normal cells grow together, will help understand the mechanisms of cancer.

Herein, a mixed co-culture model of normal brain cells and tumor cells was created to engineer the tumor microenvironment and to study whether glioma cells become more invasive by manipulating astrocytes. This co-culture system may serve as a useful tool in studying the interactions of glioma cells with normal brain cells.

3.2 Materials and Methods

3.2.1 Cell Culture

CRL-2303 (C6/lacZ7) rat glioma cells were obtained from American Type Culture Collection (ATCC) and seeded at densities 4,000 and 8,000 cells per mL in a 48-well plate and grown in CRL-2303 culture media (**Appendix A, Section A.1**).

Primary astrocytes from newborn rat tissues were seeded at densities 12,000 and 24,000 cells per mL in a 48-well plate, and grown in astrocyte growth media (**Appendix A, Section A.2**).

For a co-culture experimental model, a mixed co-culture method was employed. Glioma cells (CRL-2303) and normal brain astrocytes were seeded in the ratio 1:3 in their respective growth media into the same well with direct cell-cell contact in a 48-well cell culture plate (Griener) and allowed to grow in an incubator with 5% CO₂ at 37 °C for 3 days. The ratio of 1:3 was determined experimentally due to the fast growth rate of glioma vs. astrocytes.

To demonstrate tumor invasiveness over time, glioma cells (CRL-2303) and normal brain astrocytes were seeded in the ratio 1:4 in a 24-well cell culture plate in the same conditions as mentioned above. Further, the ability of reduced fetal bovine serum (FBS) to induce senescence [104] in glioma cells was tested.

3.2.2 Cell Fixation

After 3 days *in vitro*, the growth medium from the cells was aspirated and washed twice with 500 uL 1X PBS. Cells were fixed (**Appendix B**) using the fixation solution from β -gal kit such that it covers the entire well and the plate was kept at room temperature for 10 minutes. The cells were rinsed twice with 500 uL 1X PBS again.

3.2.3 GFAP Staining

To confirm normal *in vitro* characteristics, cells were stained using indirect immunofluorescence for glial fibrillary acidic protein (GFAP), a cytoskeletal protein found specifically in glial cells. Cells were stained using Anti-GFAP, antibody produced in rabbit as 1° Ab from Sigma-Aldrich (Sigma Product #G9269), and Alexa Fluo® 488 goat anti-rabbit IgG (H+L) as 2° Ab from Invitrogen Molecular Probes (Invitrogen Product #A-11035) (**Appendix C**).

3.2.4 β -gal Staining

As the GFAP stained both astrocytes and glioma cells, CRL-2303 cells were counterstained with β -gal staining to distinguish between the cell types in a co-culture experimental model (**Appendix D**). The β -galactosidase Reporter Gene Staining Kit was obtained from Sigma-Aldrich (Sigma Product #GALS).

3.2.5 DAPI Staining

Nuclei were stained with 4,6-diamidino-2-phenylindole (DAPI) to confirm cell viability and to compare the nuclei of glioma cells and astrocytes in a co-culture experimental model (**Appendix E**).

3.2.6 Microscopy

Microscopic images of the cells were recorded using a Leica DMI 6000B inverted microscope. β -gal staining was viewed using phase-contrast microscopy whereas GFAP staining was viewed using fluorescence settings. For fluorescent imaging, a Leica EL6000 light source was used. For GFAP imaging, excitation in the blue portion of the light spectrum (~475 nm) was required. To view DAPI-stained nuclei, excitation light in the ultraviolet range (~400 nm) was required. GFAP emits green light and DAPI emits blue light.

3.2.7 Image Analysis

All image analysis was done with Image-Pro Plus version 7.0 developed by Media Cybernetics. The total area covered by glioma cells and normal brain astrocytes was determined by analyzing the GFAP and β -gal staining for each image (**Appendix F**). The ratio was then calculated to give the percentage of glioma cells and normal brain astrocytes that cover the total area. For images stained with DAPI, the total number of nuclei (objects) and the total area covered by nuclei were calculated. To verify if the ratio for the co-culture changes over time as the glioma cells grow fast, the percentage of area covered by glioma cells is calculated from the β -gal stained images.

3.3 Results

3.3.1 GFAP Staining

Figures 3.1 and **3.2** show images of different densities of normal brain astrocytes before and after GFAP staining. **Figures 3.3** and **3.4** show images of different densities of glioma cells before and after GFAP staining. In all figures, the left panel shows phase contrast images before GFAP staining and the right panel shows fluorescence images of

the same fields after GFAP staining. The images in the top row are positive control with both primary and secondary antibodies (1° Ab + 2° Ab) and they stained positive for GFAP staining. The images in the bottom rows are negative control with no primary antibody (1° Ab) and they did not show any staining.

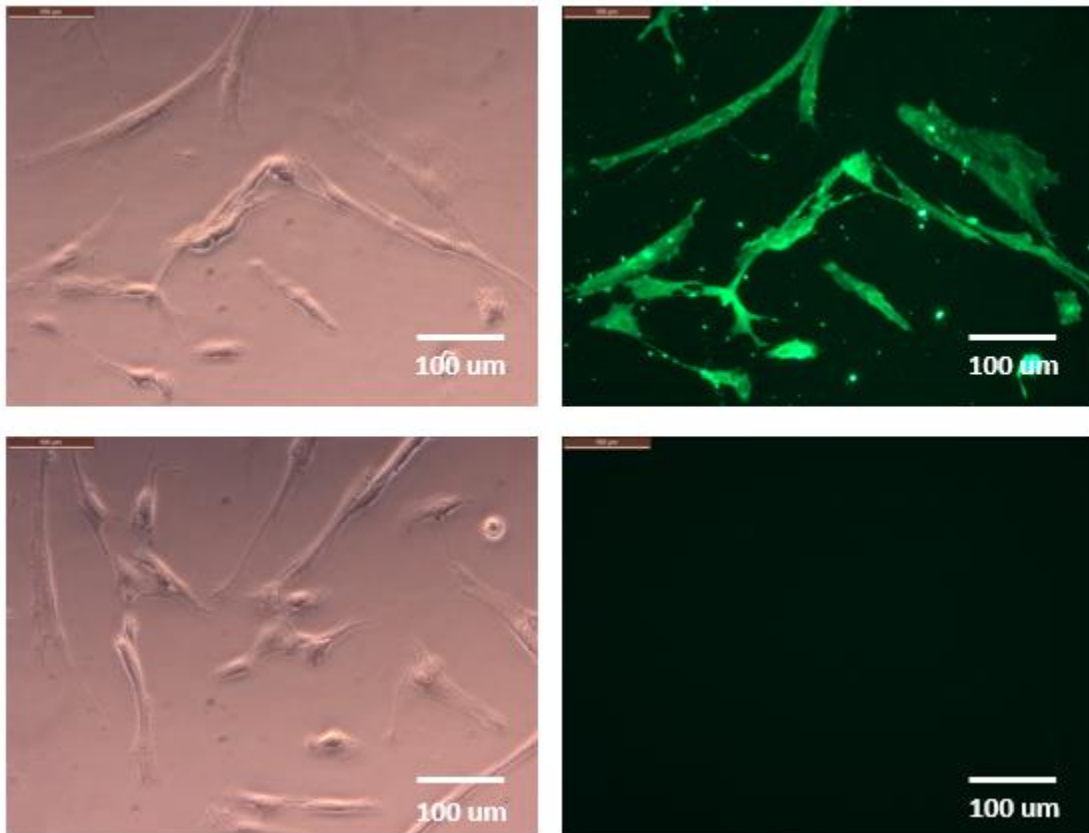


Figure 3.1: GFAP staining for 12,000 normal brain astrocytes cells per mL. The left panel shows phase contrast images before GFAP staining and the right panel shows fluorescence images after GFAP staining. The images in the top row are positive control with both primary and secondary antibodies (1° Ab + 2° Ab) and the images in the bottom row are negative control with no primary antibody (1° Ab). Scale bar = 100 μ m.

Fine astrocyte processes stained with GFAP were observed under fluorescence microscopy as shown in top rows (**Figures 3.1** and **3.2**).

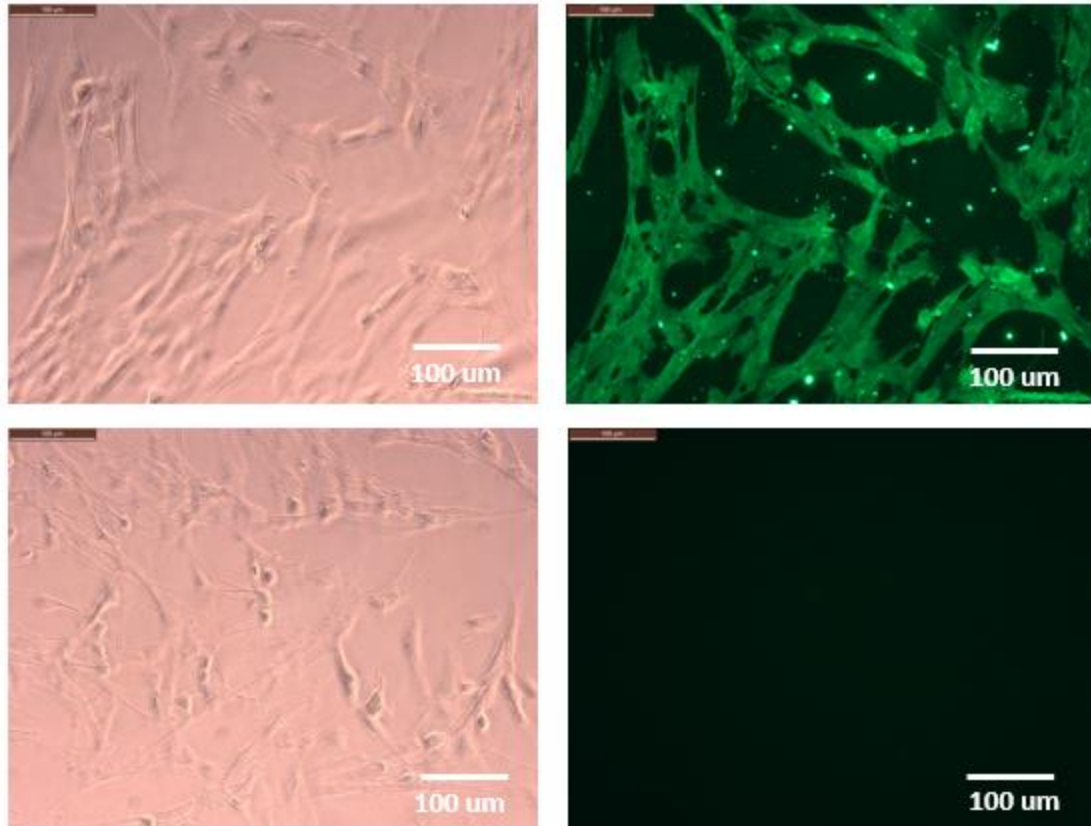


Figure 3.2: GFAP staining for 24,000 normal brain astrocytes cells per mL. The left panel shows phase contrast images before GFAP staining and the right panel shows fluorescence images after GFAP staining. The images in the top row are positive control with both primary and secondary antibodies (1° Ab + 2° Ab) and the images in the bottom row are negative control with no primary antibody (1° Ab). Scale bar = 100 μ m.

Different densities of glioma cells (CRL-2303) were stained with GFAP. **Figure 3.3** shows phase contrast images and fluorescence images of 4,000 glioma cells per mL before and after GFAP staining.

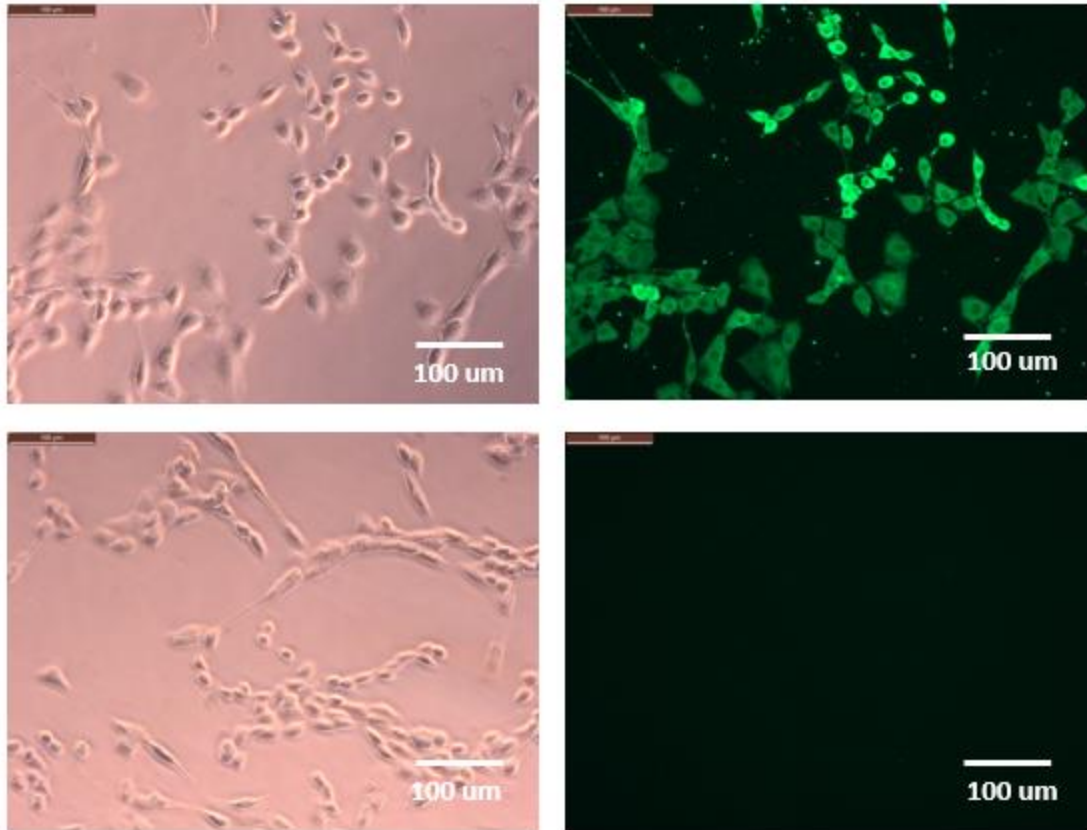


Figure 3.3: GFAP staining for 4,000 glioma cells (CRL-2303) per mL. The left panel shows phase contrast images before GFAP staining and the right panel shows fluorescence images after GFAP staining. The images in the top row are positive control with both primary and secondary antibodies (1° Ab + 2° Ab) and the images in the bottom row are negative control with no primary antibody (1° Ab). Scale bar = 100 μ m.

Next, the density of glioma cells (CRL-2303) was doubled and stained with GFAP. **Figure 3.4** shows phase contrast and fluorescence images of 8,000 glioma cells per mL before and after GFAP staining.

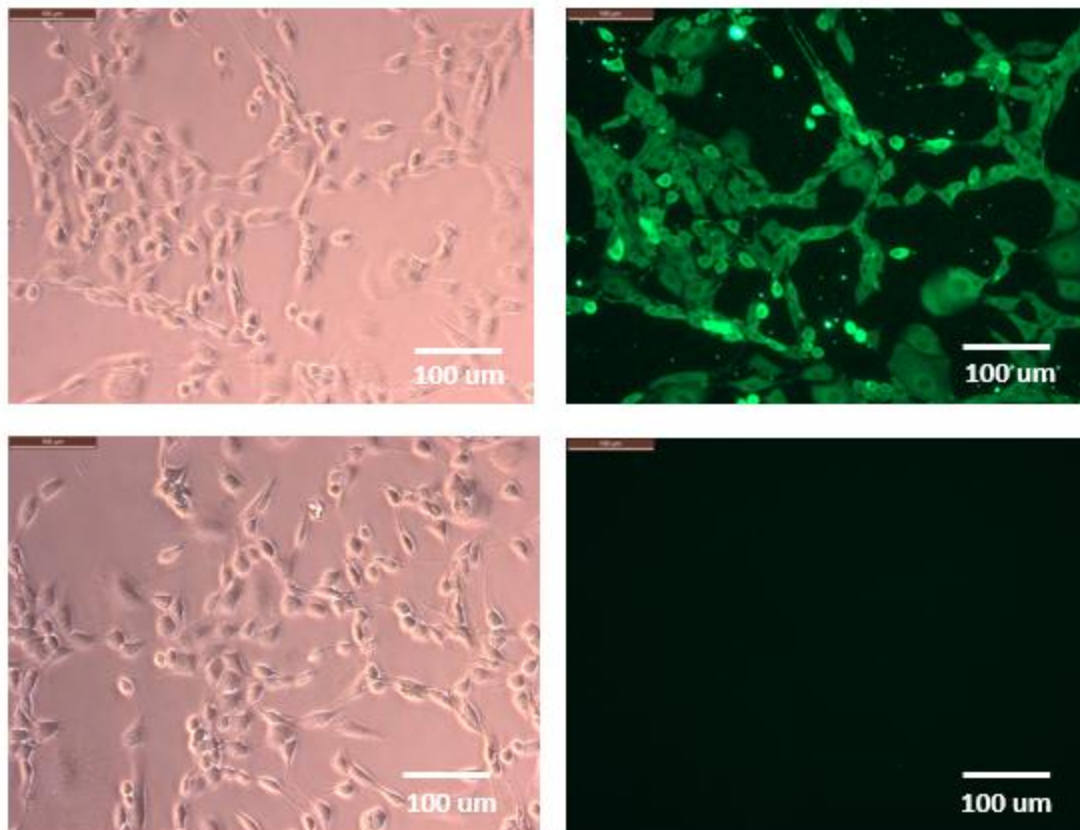


Figure 3.4: GFAP staining for 8,000 glioma cells (CRL-2303) per mL. The left panel shows phase contrast images before GFAP staining and the right panel shows fluorescence images after GFAP staining. The images in the top row are positive control with both primary and secondary antibodies (1° Ab + 2° Ab) and the images in the bottom row are negative control with no primary antibody (1° Ab). Scale bar = 100 μ m.

Although GFAP is a specific marker for astrocytes, gliomas stained positive for GFAP staining as well because the gliomas are derived from astrocytes. Thereafter, different densities of gliomas were stained with β -gal.

3.3.2 β -gal Staining

Glioma cells (CRL-2303) were stained with a β -gal staining kit and the cells were visualized under the microscope. **Figure 3.5** shows phase contrast microscopy images for

4,000 cells per mL glioma cells before and after β -gal staining. The β -gal stained the glioma cells with an indigo blue color under phase contrast microscopy.

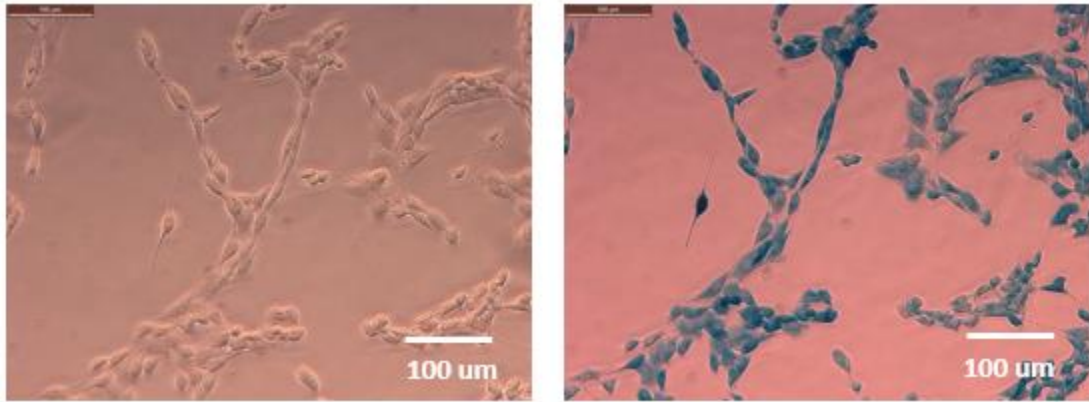


Figure 3.5: β -gal staining for 4,000 glioma cells (CRL-2303) per mL. The left panel shows the image before β -gal staining and right panel shows the same image after β -gal staining. All the images are obtained using phase contrast microscopy. Scale bar = 100 μ m.

Next, the density for glioma cells was doubled and stained with β -gal. **Figure 3.6** shows phase contrast microscopy images for 8,000 cells per mL glioma cells before and after β -gal staining.

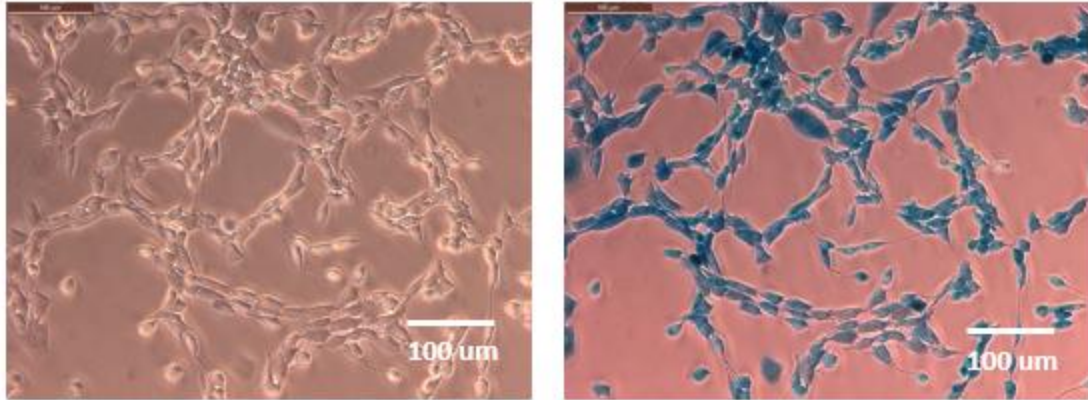


Figure 3.6: β -gal staining for 8,000 glioma cells (CRL-2303) per mL. The left panel shows the image before β -gal staining and the right panel shows the same image after β -gal staining. All the images are obtained using phase contrast microscopy. Scale bar = 100 μ m.

3.3.3 Staining Co-culture with GFAP and β -gal

Figure 3.7 shows co-culture of 4,000 glioma cells (CRL-2303) per mL and 12,000 normal brain astrocytes per mL. The left panels show phase contrast microscopy images before they were stained with GFAP and β -gal. In the co-culture experimental model, both normal brain astrocytes and glioma cells (CRL-2303) stained positive for GFAP staining as shown from the middle panel (top row), the top row is positive control with both primary and secondary antibodies (1° Ab + 2° Ab) and the bottom row is negative control with no primary antibody (1° Ab). The images in the right panel are the same fields after the cells were stained with β -gal. Gliomas stained positive where as normal brain astrocytes stained negative for β -gal staining as shown in right panels.

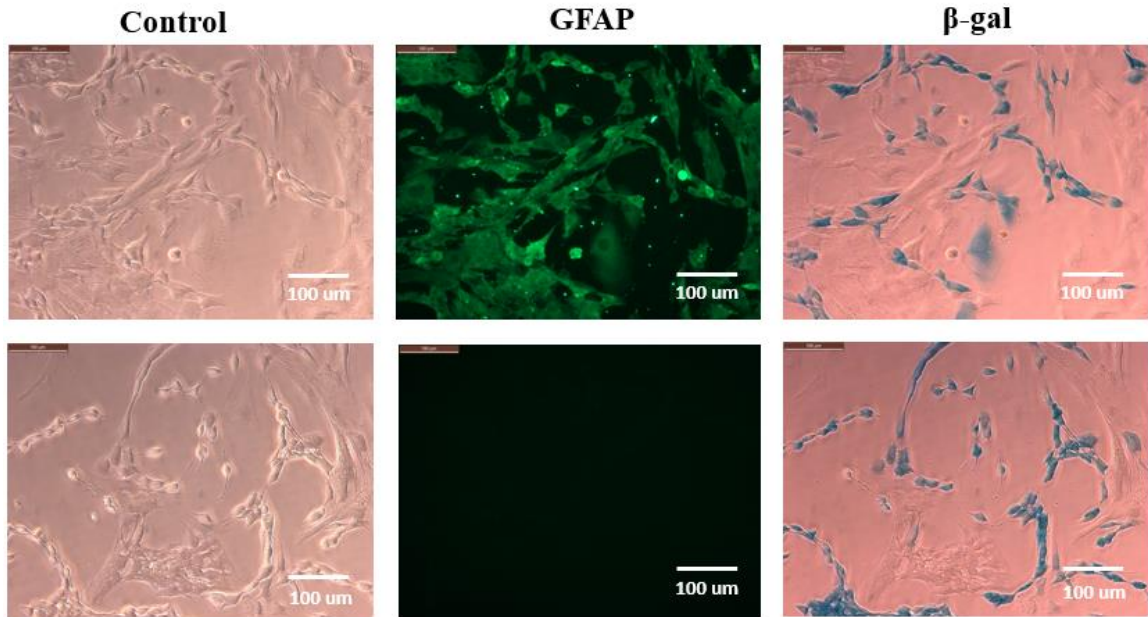


Figure 3.7: Control (no staining), GFAP and β -gal staining for co-culture of 4,000 glioma cells (CRL-2303) per mL and 12,000 normal brain astrocytes per mL. The left panel (Control) and the right panel (after β -gal staining) are the images obtained with phase contrast microscopy. The middle panel (after GFAP staining) are the images obtained with fluorescence microscopy, the top row is positive control with both primary and secondary antibodies (1° Ab + 2° Ab) and the bottom row is negative control with no primary antibody (1° Ab). Scale bar = 100 μ m.

Figure 3.8 shows co-culture of 8,000 glioma cells (CRL-2303) per mL and 24,000 normal brain astrocytes per mL.

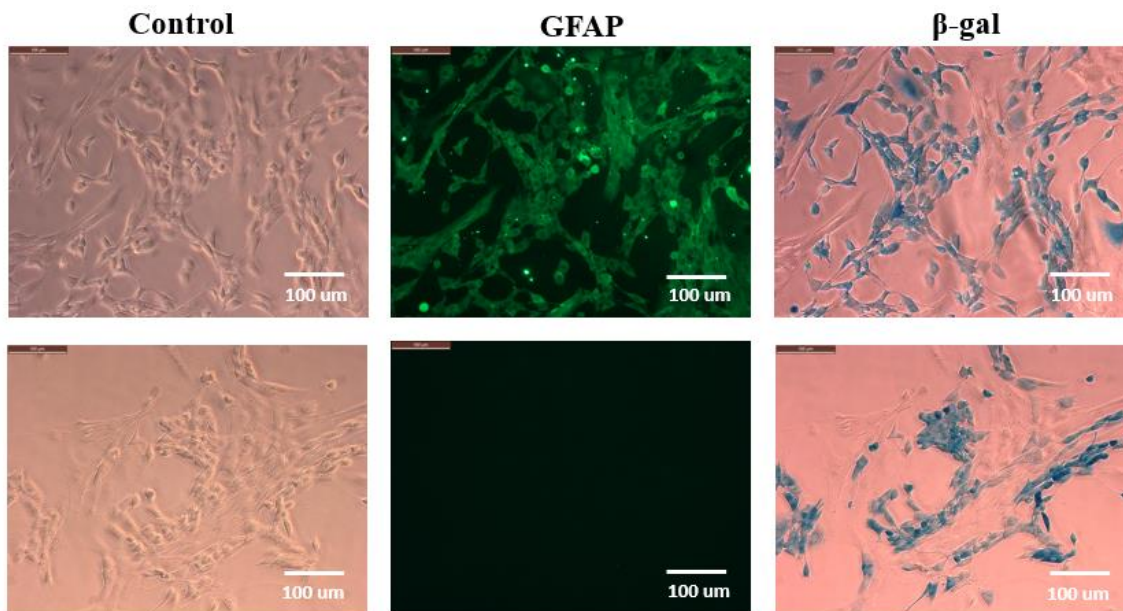


Figure 3.8: Control (no staining), GFAP and β -gal staining for co-culture of 8,000 glioma cells (CRL-2303) per mL and 24,000 normal brain astrocytes per mL. The left panel (Control) and the right panel (after β -gal staining) are the images obtained with phase contrast microscopy. The middle panel (after GFAP staining) are the images obtained with fluorescence microscopy, the top row is positive control with both primary and secondary antibodies (1° Ab + 2° Ab) and the bottom row is negative control with no primary antibody (1° Ab). Scale bar = 100 μ m.

There were no notable changes in morphology in the co-culture of glioma cells with astrocytes as compared to glioma cells alone and astrocytes alone (**Figures 3.7 and 3.8**).

After staining with GFAP and β -gal, the percentage of total area of the image covered by different densities of CRL-2303 and astrocytes at 3 days *in vitro* (div) were calculated using Image-Pro Plus version 7.0 and the results are as shown in **Table 3.1**.

Table 3.1: Total area of the image covered by different densities of gliomas (CRL-2303) and astrocytes at 3 days *in vitro* (div) (in %)

4k CRL-2303	8k CRL-2303	12k Astros	24k Astros	4k CRL-2303 + 12k Astros		8k CRL-2303 + 24k Astros	
				CRL-2303	Astros	CRL-2303	Astros
12.2	34.4	21.0	45.7	7.01	40.7	14.8	37.5
10.2	34.1	25.5	41.1	9.03	21.4	28.1	15.9
13.9	32.0	25.4	47.4	10.0	40.3	11.7	39.3

As shown in **Table 3.1**, after 3 div, the total area of the image covered by gliomas (CRL-2303) increased by almost three-fold whereas the total image area covered by astrocytes increased by almost two-fold as the density of the cells was increased two times when they were cultured alone. This is due to the fast growth of gliomas than astrocytes. Also, the cell bodies of astrocytes are bigger than gliomas, hence they occupy more area than gliomas. However, when the densities of both cell populations were doubled, the culture become crowded and much more variation was observed. Thus, the cells behave differently in a co-culture setup. The total area of the image covered by gliomas decreased when the cells were in co-culture with astrocytes as compared to when they were cultured alone. Hence, we concluded that the presence of astrocytes creates less room for gliomas to grow at 3 days *in vitro*, but gliomas take over the astrocytes over time as shown later in this chapter.

3.3.4 Identifying Cell Types Using Size and Shape of Nuclei

Cells were stained with DAPI after 3 div to compare the nuclei of glioma cells and astrocytes in a co-culture experimental model. **Figure 3.9** shows the images for qualitative morphological analysis of DAPI-stained nuclei for different densities of

glioma cells alone, normal brain astrocytes alone, and co-cultured glioma cells with astrocytes.

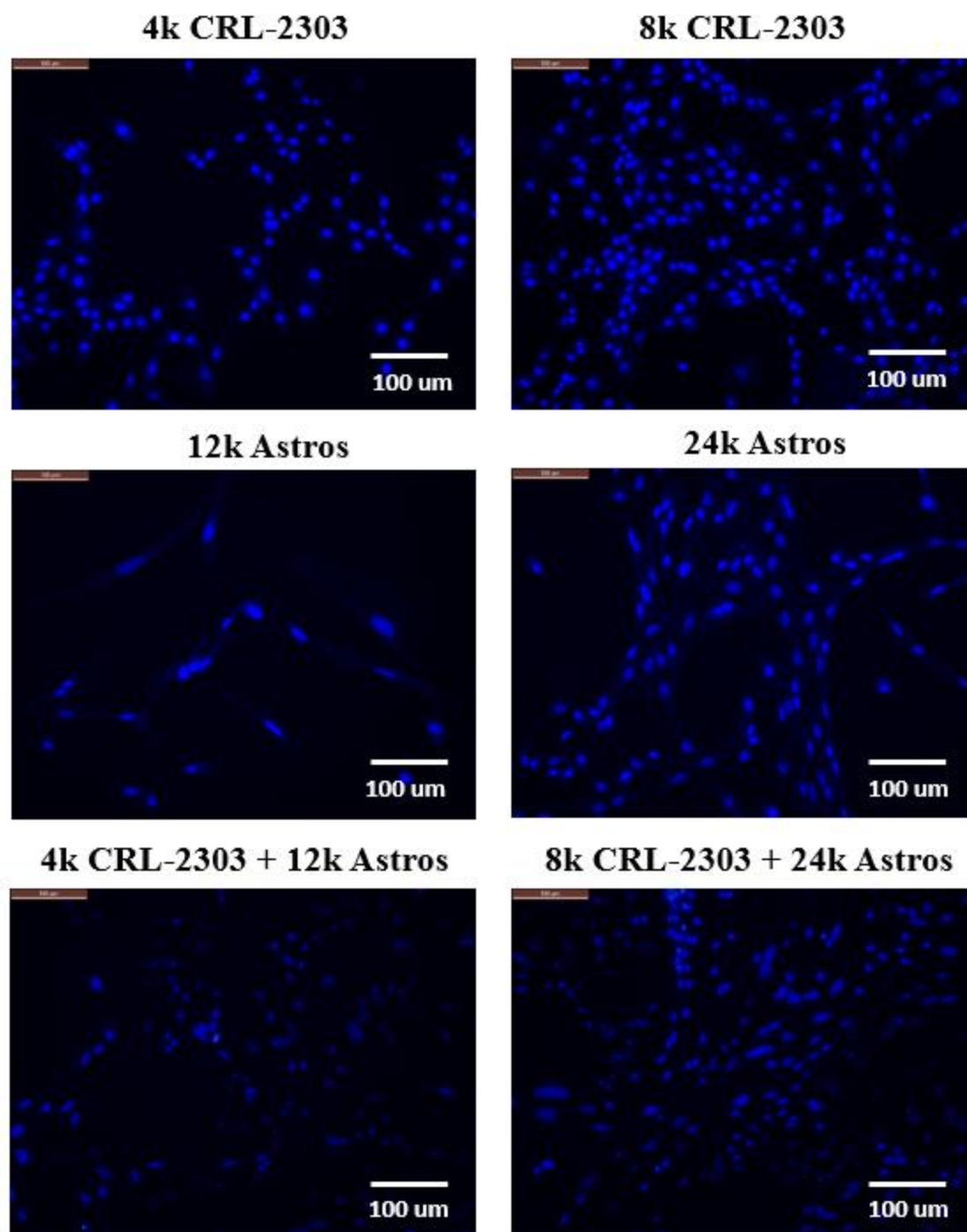


Figure 3.9: Fluorescence images of DAPI-stained nuclei for different densities (per mL) of glioma cells alone (CRL-2303), normal brain astrocytes alone, and co-cultured glioma cells and astrocytes. Scale bar = 100 μ m.

Figure 3.9 shows the nuclei of astrocytes are larger than those of glioma cells (CRL-2303) and that they are elongated in shape irrespective of the different densities of cells. There were no differences in the nuclei of cells in co-culture as compared to when they were cultured alone. Hence, the shape and size of the DAPI-stained nuclei are useful factors to distinguish the glioma cells and the astrocytes in a co-culture model. However, a brighter nuclear staining was observed for astrocytes than glioma cells in a mixed culture because β -gal, which was used to stain glioma cells, quenches the DAPI staining.

Figure 3.10 are the images for distinguishing normal brain astrocytes from glioma cells based on the size and shape of nuclei in a co-culture model. These results are further supported with the same images from β -gal staining.

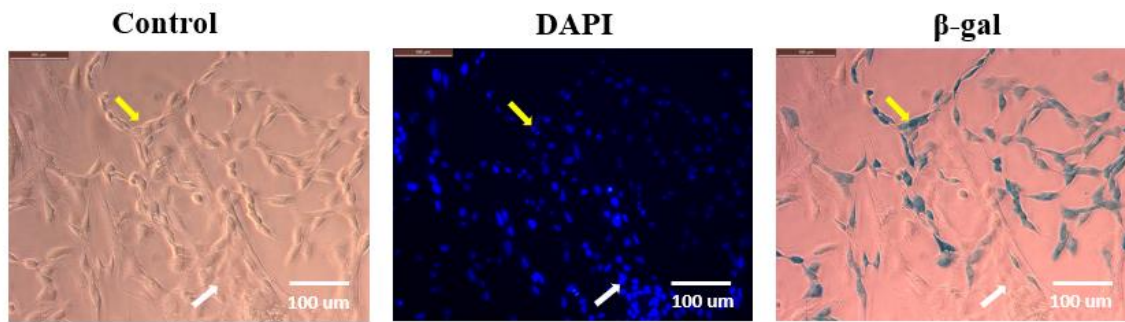


Figure 3.10: Control, DAPI-stained nuclei, and β -gal staining for co-culture of 4,000 cells per mL gliomas (CRL-2303) and 12,000 cells per mL normal brain astrocytes. Left panel represents phase contrast images (Control), middle panel shows fluorescent images of DAPI-stained nuclei, and right panel shows the same phase contrast images after staining with β -gal. Yellow arrows show glioma cells and white arrows show normal brain astrocytes. Scale bar = 100 μ m.

Next, the densities of cells in co-culture were increased and the microscopic images were obtained as shown in **Figure 3.11**.

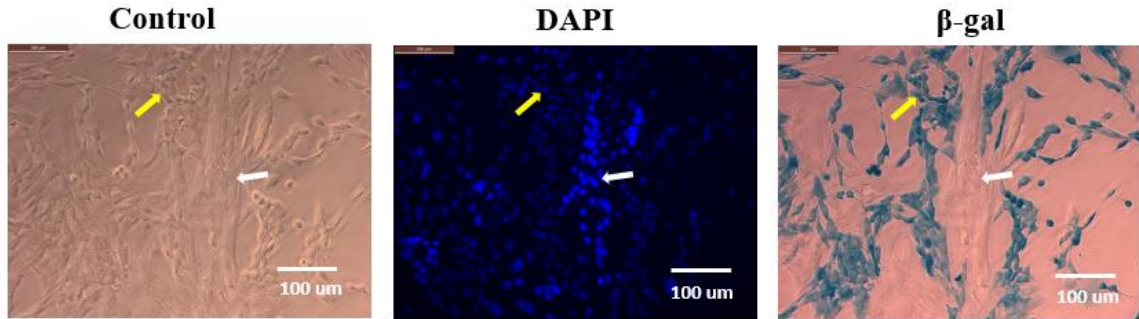


Figure 3.11: Control, DAPI-stained nuclei, and β -gal staining for co-culture of 8,000 cells per mL gliomas (CRL-2303) and 24,000 cells per mL normal brain astrocytes. Left panel shows phase contrast images (Control), middle panel shows fluorescent images of DAPI-stained nuclei, and right panel shows the same phase contrast images after staining with β -gal. Yellow arrows show glioma cells and white arrows show normal brain astrocytes. Scale bar = 100 μ m.

Yellow arrows point to glioma cells, where the nuclei are characterized by their smaller size, fainter appearance, and the take up of β -gal stain. White arrows point to normal brain astrocytes with elongated bright nuclei and lack of β -gal stain.

The average number of nuclei (objects) and average area covered by cells were studied for two different densities of glioma cells alone, normal brain astrocytes alone, and co-culture of both cells. **Figure 3.12** shows the average number of nuclei after three days for various seeding densities of glioma cells alone, normal brain astrocytes alone, and co-culture of both cells. When the seeding densities of cells were doubled, the number of nuclei in glioma cells after three days increased by more than two-fold, whereas the number of nuclei in astrocytes did not change significantly. This result indicates that glioma cells grow faster than astrocytes. However, the number of nuclei remained constant with the increasing densities of cells in co-culture. It was observed that with the increasing number of both gliomas and astrocytes in a co-culture setup, the cells eventually reach confluence and cease to grow.

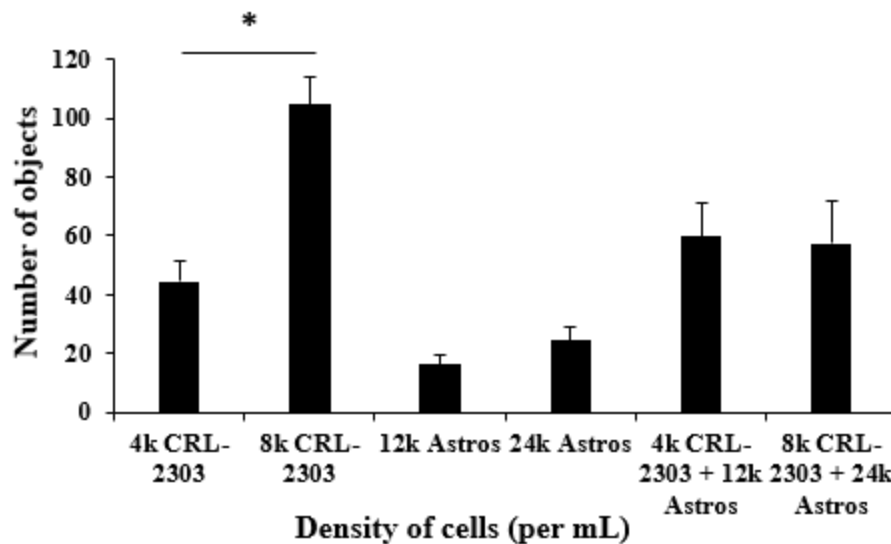


Figure 3.12: Average nuclei number covered by gliomas alone, normal brain astrocytes alone, and co-culture of gliomas with astrocytes after 3 days *in vitro* (div). Error bars indicate standard deviation (SD); * $P < 0.05$, $n = 9$.

Figure 3.13 shows the average nuclei area after three days covered by various seeding densities of glioma cells alone, normal brain astrocytes alone, and co-cultures of glioma cells and astrocytes. The average nuclei area covered by glioma cells cultured alone was approximately 1,600 square pixels, whereas the average nuclei area covered by normal brain astrocytes cultured alone was approximately 4,000 square pixels. Results showed that the average area covered by nuclei of normal brain astrocytes was almost 60% more than glioma cells. For co-culture of both glioma cells and astrocytes, the average area covered by nuclei was 2,500 square pixels, which was 56% larger than the area covered by glioma cells alone. As expected, the varying seeding densities of cells did not affect the average nuclei area for each cell type. The average nuclei area covered by cells was not significant within the same cell type but significant with different cell populations.

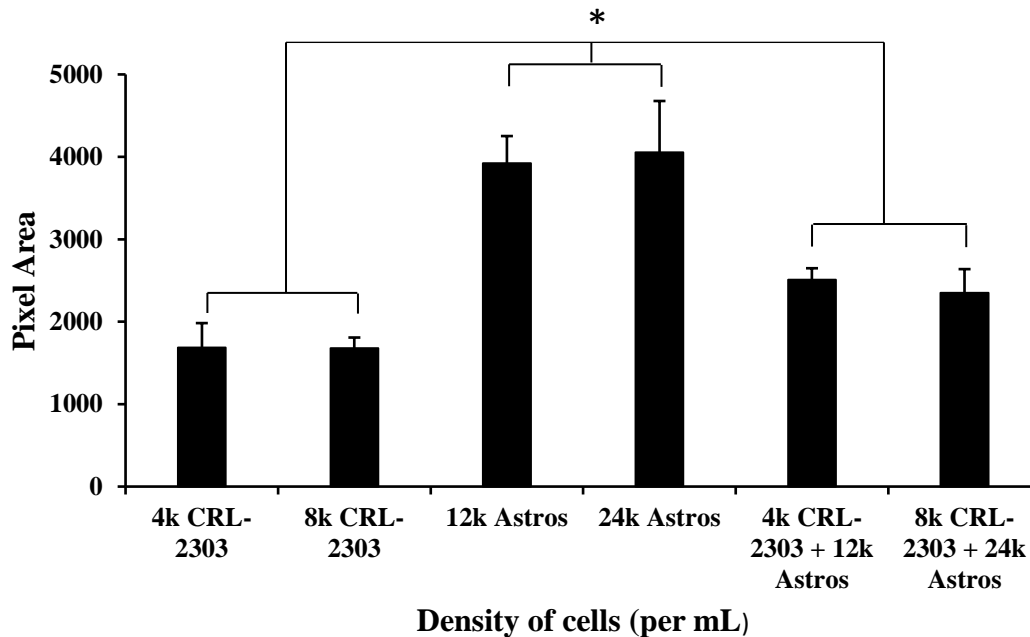


Figure 3.13: Average nuclei area covered by gliomas alone, normal brain astrocytes alone, and co-culture of gliomas with astrocytes after 3 days *in vitro* (div). Error bars indicate standard deviation (SD); * $P < 0.05$, $n = 9$.

From **Figures 3.12** and **3.13**, the cell nuclei of astrocytes in monocultures occupy more cell area than the cell nuclei of glioma cells in monoculture because the average area of nuclei for astrocytes is larger than that of glioma cells even though astrocyte culture has fewer nuclei than the glioma cell culture. The gliomas have much smaller nuclei than astrocytes.

3.3.5 Tumor Invasion in Co-culture

Next, it was hypothesized that the tumor invasiveness increases over time in a co-culture model. To demonstrate this, β -gal staining was used as shown in **Figure 3.14** and the percentage area of the image covered by glioma cells was calculated over 8-day period as demonstrated in **Figure 3.15**.

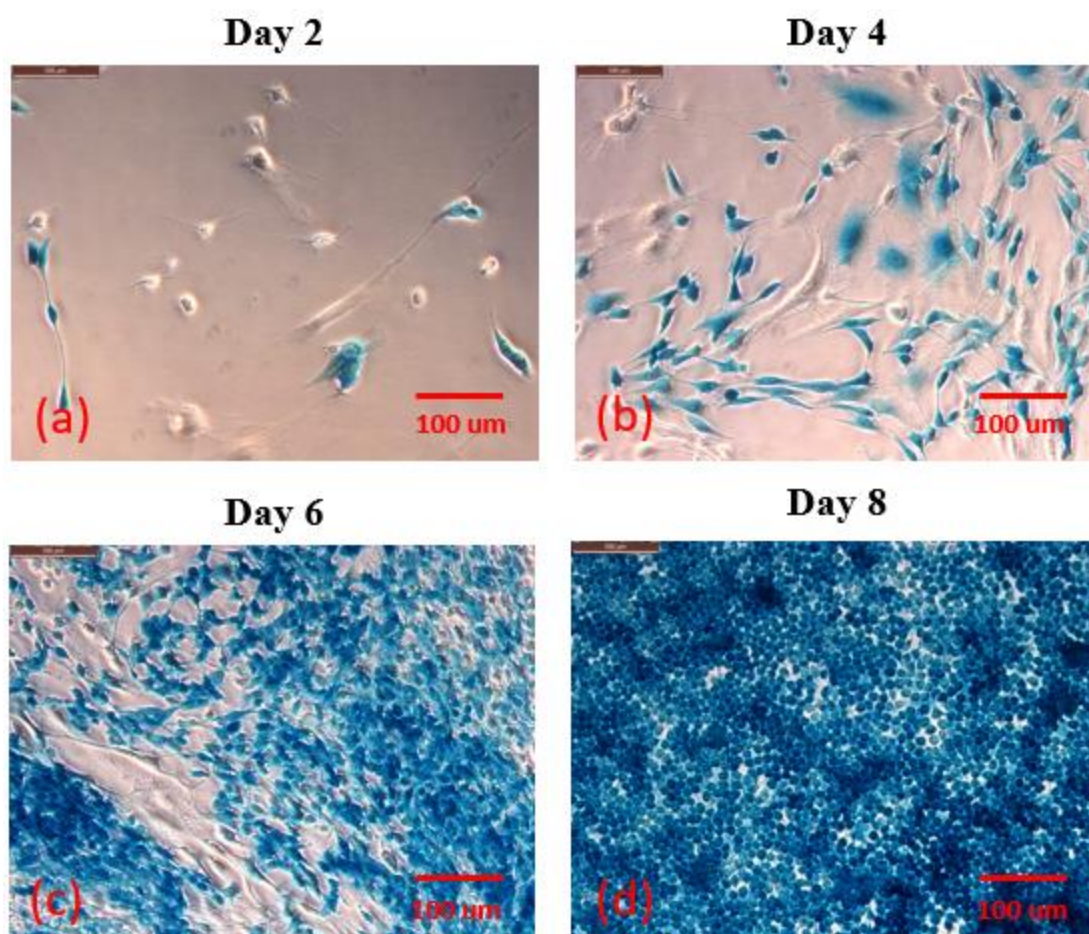


Figure 3.14: β -gal staining on co-culture of 3,000 glioma cells (CRL-2303) per mL and 12,000 normal brain astrocytes per mL at a) Day 2, b) Day 4, c) Day 6, and, d) Day 8. Scale bar = 100 μ m.

Glioma cells are stained indigo blue by the β -gal staining. The images show that glioma cells dominate the co-cultures. Whereas the astrocytes outnumber glioma cells at Day 2, by Day 8 the tumor cells are so numerous that they may be inhibiting the growth of normal brain astrocytes.

These results are shown quantitatively in **Figures 3.15** and **3.16**. **Figure 3.15** shows the graph for total area coverage by β -gal staining in a co-culture model over 8-

day period, demonstrating an increase from 1.8% to 90.7%. In contrast, the total area without staining decreased by an order of magnitude, as shown in **Figure 3.16**.

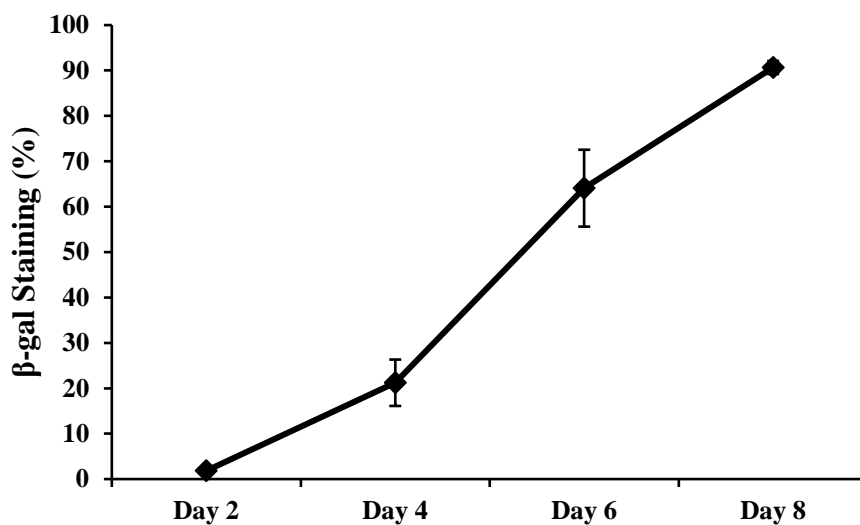


Figure 3.15: Total area coverage (%) by β -gal staining on co-culture of 3,000 glioma (CRL-2303) cells per mL and 12,000 normal brain astrocytes per mL over time.

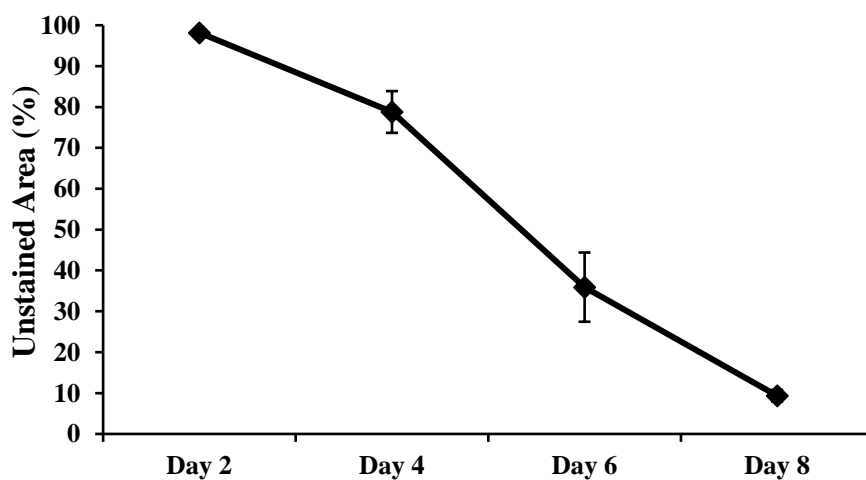


Figure 3.16: Total unstained area (%) on co-culture of 3,000 glioma cells (CRL-2303) per mL and 12,000 normal brain astrocytes per mL over time.

Part of the non-stained area is astrocytes, while the rest is surface area that is not covered by cells at all. As the cells become more confluent, this open area decreases. The chart shows, however, that the ratio of the area covered by glioma cells to area covered by astrocytes is increasing, given that the ratio of cells at seeding is 1 to 4, whereas the area coverage at Day 8 is at least 10 to 1.

Changes in shape and size of cells were observed over time, so DAPI staining was used to compare the nuclei over time and the results are shown in **Figure 3.17**.

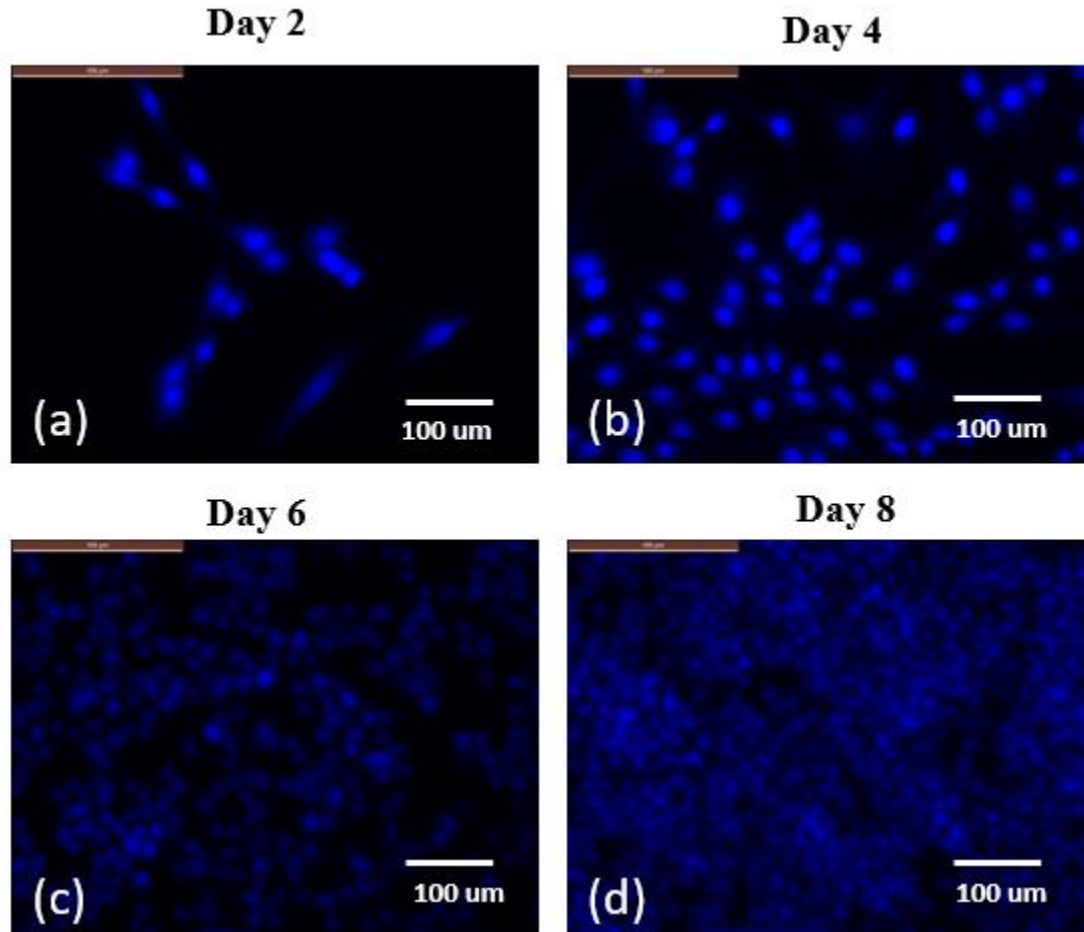


Figure 3.17: DAPI staining on co-culture of 3,000 glioma cells per mL (CRL-2303) and 12,000 normal brain astrocytes per mL at a) Day 2, b) Day 4, c) Day 6, and, d) Day 8. Scale bar = 100 μm.

Figures 3.14 and **3.17** show that the cell bodies and nuclei get smaller over time. The number of nuclei were comparatively less on Day 2 than on Days 4, 6 and 8. By Day 8, the nuclei of the cells were packed, and the shape of the nuclei were rounder.

3.4 Conclusion and Discussion

Due to the different growth characteristics of the cell lines, a co-culture experimental model can be complex. Here, a co-culture model of normal brain astrocytes and brain tumor cells was developed. In this co-culture model, the brain tumor cells grow rapidly due to autocrine and paracrine signaling between cells [2], whereas the normal brain astrocytes proliferated more slowly. Here, GFAP and β -gal staining were used to distinguish between the two populations of cells in a co-culture model.

GFAP, a marker for glial cells stained positive for both normal brain astrocytes and brain tumor cells. One of the reasons behind positive staining of glioma cells for GFAP is that glioma cells are derived from glial cells [43], [90], [91]. In this study, β -gal was used to stain only the glioma cells but not normal brain astrocytes. Normal brain astrocytes stained negative to β -gal whereas brain tumor cells turned indigo blue color. The β -gal kit is extremely sensitive to fixatives. Ma *et al.* tested the effect of different fixatives and reported that Carnoy's solution hampered the β -gal activity [105]. Our data suggest that GFAP should be done prior to β -gal staining as quenching and downregulation of GFAP were observed in glioma cells after β -gal staining. Nuclear shape and size are distinct properties of any cell type [106] and may be useful in distinguishing between the different cell populations.

Initially, the astrocytes thrive in the presence of glioma cells creating less room for the gliomas to grow, but later the gliomas take over the astrocytes. Astrocytes secrete

matrix metalloproteinase (MMP-2) precursor and it is thought that glioma cells use MMP-2 dependent pathway to exploit astrocytes for tumor invasiveness [107]. Results showed that the presence of glioma cells suppress the growth of healthy brain cells over time, thus facilitating tumor invasiveness. These findings are consistent with the reports from Gagliano *et al.* [44], [45]. Since astrocytes have the ability to proliferate, they might be transformed into glioma overtime as the cellular origins of gliomas are astrocyte precursor cells. The interaction of astrocytes with tumor cells via gap junctions causes an increase in intracellular calcium causing difficulties in chemotherapeutic treatments. Recent studies have shown that glioma cells release glutamate at sufficiently large concentrations to cause neuronal cell death [108]. Glioma invasion might also be linked to astrocytes going through phenotype modification/ transformation and the tumor cells losing their expression over time. Moreover, studies have shown that sulfasalazine can cause inhibition of glioma invasion [108], [109].

Fetal bovine serum (FBS) did not induce senescence in glioma cells [104]. It was noted that the glioma cells might lose expression over time and might not stain all the cells with indigo blue color. Thus, a mixed co-culture experimental model of normal brain cells and tumor cells is suitable to study cell-cell interactions in tumor microenvironment. Further, the model serves as a useful tool in understanding the growth of tumor in the brain.

CHAPTER 4

STUDYING GLUTAMATE UPTAKE IN A CO-CULTURE EXPERIMENTAL MODEL OF NORMAL BRAIN ASTROCYTES AND GLIOMA CELLS

4.1 Introduction

Glutamate is the major excitatory neurotransmitter in the brain. Glutamate transporters EAAT1 and EAAT2, primarily found in astrocytes, clear glutamate from the extracellular space by a glutamate uptake mechanism [74], [110]. Under normal physiological conditions, the concentration of glutamate in the brain is tightly regulated [7]. However, gliomas release glutamate through system x_c^- cystine-glutamate transporter [111].

Brown *et al.* [112] showed enhanced uptake of glutamate by astrocytes when astrocytes were co-cultured with cerebellar neurons. Failure to uptake glutamate from the extracellular space causes excitotoxicity to the neurons which might lead to disease conditions such as seizure and epilepsy [85]. In a diseased state such as cancer, both glioma cells, and normal brain astrocytes are present. However, glutamate uptake in systems containing both astrocytes and glioma cells has not been studied. A clear understanding of the glutamate uptake in the presence of both cell types is essential to controlling glutamate toxicity.

Here, glutamate uptake was measured in normal brain astrocytes and glioma cells (CRL-2303) individually as well as in the co-culture model developed as discussed in

Chapter 3. The aim of this study was to investigate glutamate uptake in the presence of both astrocytes and glioma cells. Further, we observed the morphological changes in astrocytes in sodium-free medium by blocking sodium-dependent transporters.

4.2 Materials and Methods

4.2.1 Cell Culture

CRL-2303 (C6/lacZ7) rat glioma cells were obtained from American Type Culture Collection (ATCC) and seeded in a 24-well plate at densities 50,000, 100,000, and 200,000 cells per mL in growth media containing DMEM-high glucose, including 4500 mg/L glucose, L-glutamine, and sodium bicarbonate, without sodium pyruvate (Sigma-Aldrich) with fetal bovine serum (10% v/v), MEM non-essential amino acid solution 100x (1% v/v), and penicillin/streptomycin (0.5% v/v) added (**Appendix A, Section A.1**).

Astrocytes from primary newborn rat tissues were seeded at densities 50,000, 100,000, and 200,000 cells per mL in a 24-well plate, grown in Nutrient Mixture F-12 Ham plus L-glutamine and sodium bicarbonate (Sigma-Aldrich) with horse serum (5% v/v), fetal bovine serum (5% v/v), and penicillin/streptomycin (0.5% v/v) (**Appendix A, Section A.2**), and placed in an incubator with 5% CO₂ and 37 °C until they reached ~80% confluency.

For a co-culture experimental model, normal brain astrocytes and glioma cells (CRL-2303) were seeded in the ratio 3:1 into the same well in their respective growth media with direct cell-cell contact in a 48-well cell culture plate (Griener) and allowed to grow in an incubator for 3 days. After that, glutamate assay was performed to measure the glutamate uptake in co-culture.

4.2.2 Glutamate Assay

For quantitative colorimetric determination of glutamate, an Enzychrom™ Glutamate Assay Kit (#EGLT-100) was obtained from BioAssay Systems and used according to standard protocols. Cells were preincubated with 100 μ M glutamate for 5 hr in an incubator maintained at 5% CO₂ and 37 °C. Then, 20 μ L sample was transferred to a 96-well plate and 80 μ L working reagent was added on top of it. Standard curves (100-400 μ M) were prepared as well. The plate was slightly tapped to mix the sample and reagent briefly and thoroughly. Spectrophotometric measurements were carried out using ThermoScientific Multiskan Spectrum. Optical densities for time “zero” (OD₀) and after a 30-min incubation (OD₃₀) were measured at 565 nm. For the standard and sample wells, OD₀ was subtracted from OD₃₀. Glutamate levels in the media were determined.

4.2.3 Sodium (Na⁺) Transport Test

Choline Chloride (MW=139.62 g/mol) was obtained from Sigma-Aldrich (St. Louis, MO). The exposure medium was Locke’s solution (**Appendix A, Section A.4**) whereas sodium chloride was replaced with choline chloride for sodium-transport experiments.

4.2.4 MTT Assay

MTT [3-(4,5-dimethylthiazol-2-yl)-2,5-diphenyltetrazolium bromide] was obtained from Thermo Fisher Scientific (Waltham, MA). MTT assay is a biochemical assay used to determine the metabolic rate of cells. To determine if the presence of glutamate had any effect on cells, MTT assay was carried out in the presence and absence of 100 μ M glutamate. The stock concentration (5 mg/mL) of MTT, a yellow tetrazole, was diluted in DMEM without phenol red to obtain a final concentration of 1.25 mg/mL.

After that, media was aspirated from each well and 400 uL of MTT was added. The well plate was wrapped with aluminum foil and placed in the incubator for 60 minutes. After the incubation period, purple colored formazan crystals were observed, and they were dissolved with 300 uL of 91% isopropyl alcohol and mixed to lyse the cells. The samples were measured at 570 nm using a 96-well microplate plate reader (Thermoscientific Multiskan Spectrum). The absorbance values were assumed to be directly proportional to the number of viable cells.

4.2.5 Statistics

Data analysis was performed in Microsoft Excel and the significance of the test results was analyzed using Students t-test. A p-value less than 0.05 was considered statistically significant.

4.3 Results

4.3.1 Glutamate Uptake

After 3 days *in vitro*, 100 uM glutamate was added to different densities of normal brain astrocytes and glioma cells and incubated at 37 °C and 5% CO₂ for 5 hr. Microscopic images were recorded to observe the changes in morphology of cells before and after addition of glutamate. **Figure 4.1** shows the morphological changes in normal brain astrocytes before and after preincubation with 100 uM glutamate.

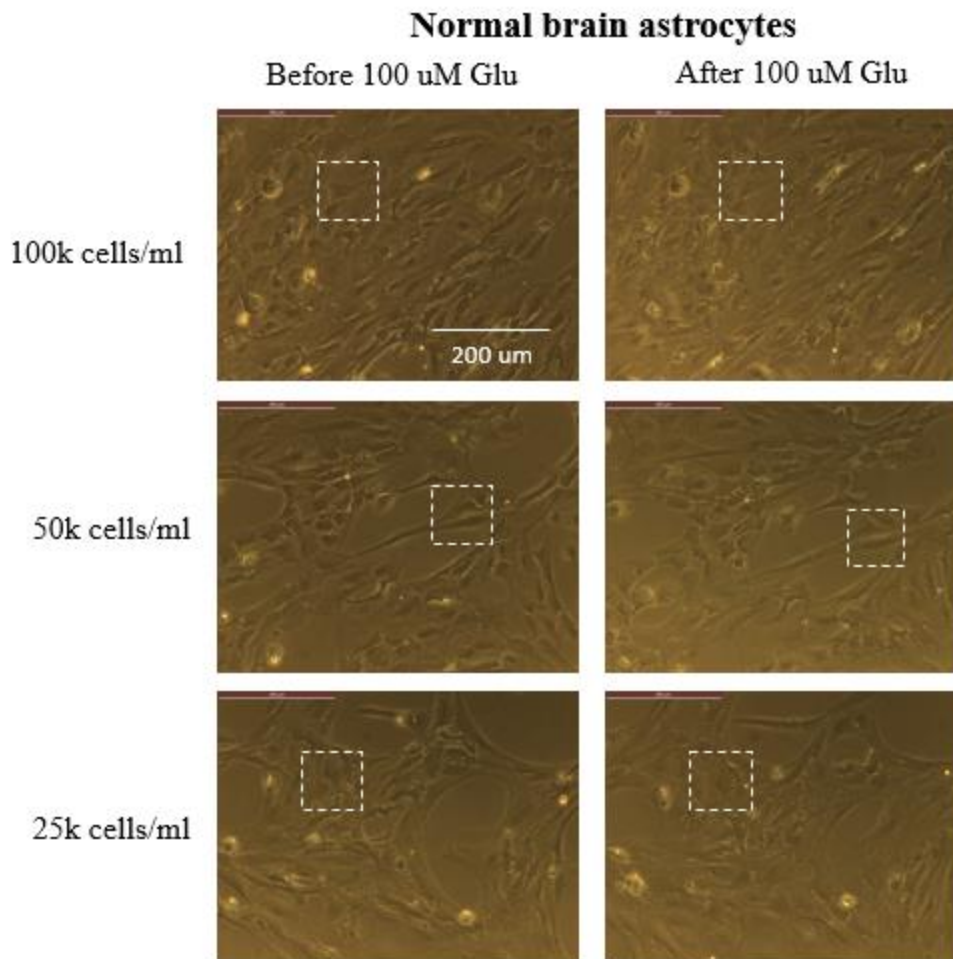


Figure 4.1: Microscopic images of 100k, 50k and 25k cells per mL normal brain astrocytes after 5 days *in vitro* (div) before and after preincubation with 100 uM glutamate for 5 hr at 37 °C. Scale bar = 200 um. Dotted square lines mark the same area between the left and right image and show that the morphology of the cells remained the same before and after addition of 100 uM glutamate.

Next, different densities of glioma cells were preincubated with 100 uM glutamate for 5 hr at 37 °C and 5% CO₂. Microscopic images of the same area of the wells were recorded before and after addition of 100 uM glutamate. The microscope's internal coordinate system was used to take images at specific locations at several time points. **Figure 4.2** shows the morphological changes in glioma cells before and after

preincubation with 100 μ M glutamate. The addition of 100 μ M glutamate did not cause any visible signs of cellular stress over 5 hr.

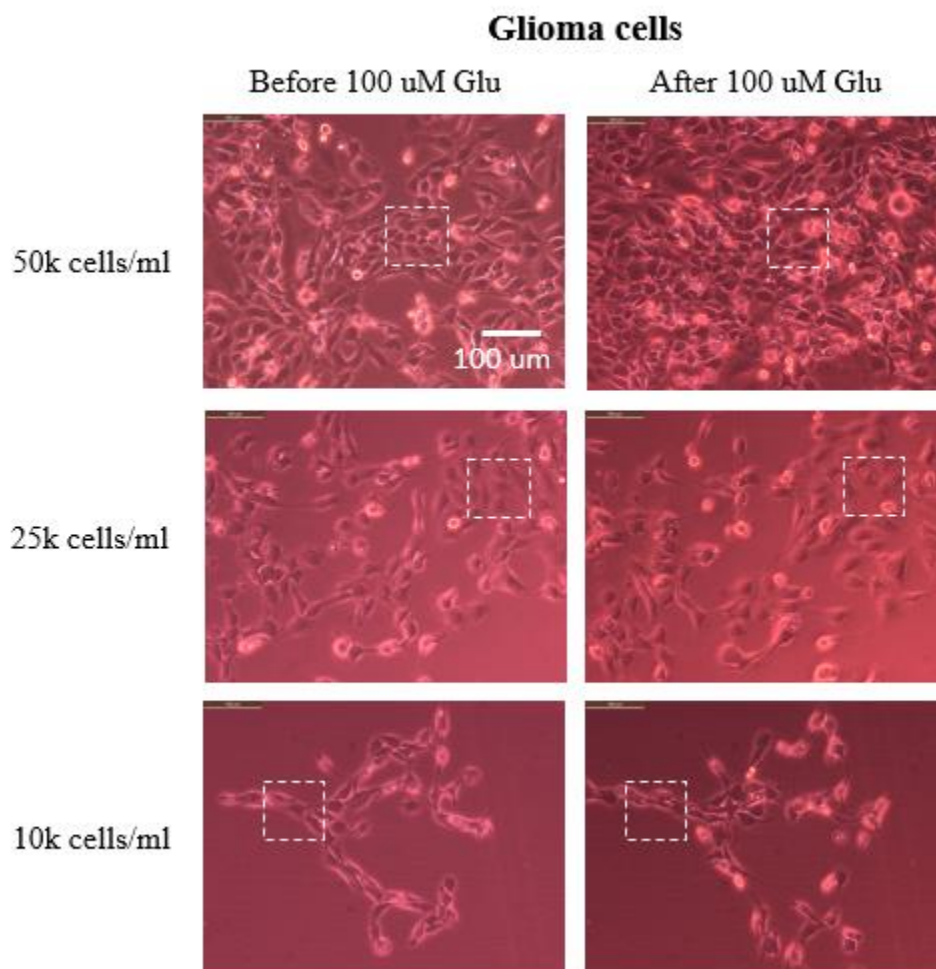


Figure 4.2: Microscopic images of 50k, 25k and 10k cells per mL glioma cells (CRL-2303) after 3 days *in vitro* (div) before and after preincubation with 100 μ M glutamate for 5 hr at 37 $^{\circ}$ C. Scale bar = 100 μ m. Dotted square lines mark the same area between the left and right image and show that the morphology of the cells remained the same before and after addition of 100 μ M glutamate.

Next, an Enzychrom™ Glutamate Assay Kit was used to measure the amount of extracellular glutamate. **Figure 4.3** shows the glutamate uptake by different densities of normal brain astrocytes and glioma cells grown in monoculture.

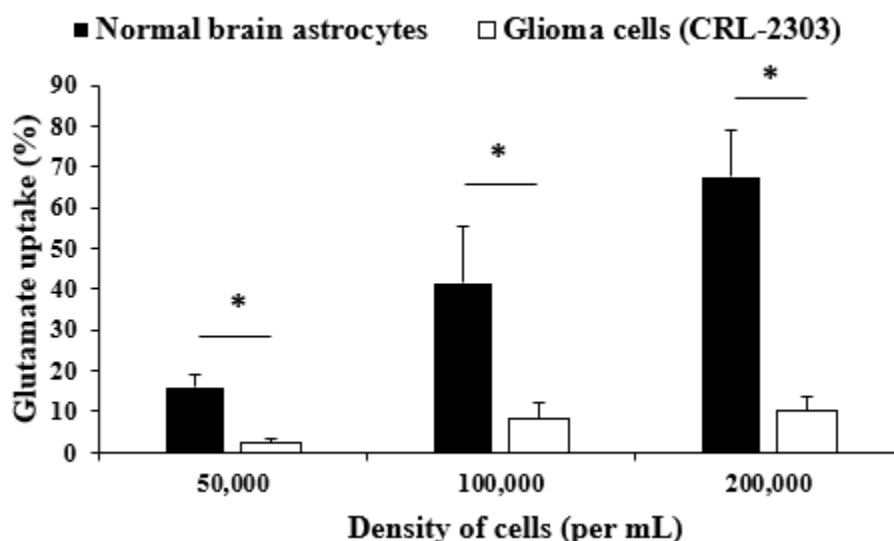


Figure 4.3: Percentage of glutamate uptake by different densities of normal brain astrocytes and glioma cells (CRL-2303) at 3 days *in vitro* (div) after preincubation with 100 μ M Glu for 5 hr at 37 °C. Error bars indicate standard deviation (SD); * $P < 0.05$, $n = 3$.

Glutamate uptake by normal brain astrocytes and glioma cells increased in a density-dependent manner. For 200k, 100k, and 50k cells per mL, normal brain astrocytes showed glutamate uptake of 67.7%, 41.7%, and 15.9% respectively. In contrast, under the same conditions, glioma cells showed 10.1%, 8.2% and 2.5% respectively. The ratio of uptake for glutamate between normal brain astrocytes and glioma cells was about 6:1 for a seeding of 200k cells per mL, about 5:1 for a seeding of 100k cells per mL and then 6:1 again when the seeding density was 50k cells per mL. Therefore, glutamate uptake by

normal brain astrocytes exhibited approximately a six-fold increase compared to glioma cells for all three densities of cells used. These data show that the uptake of glutamate is greatly lower in glioma cells compared with normal brain astrocytes. An increased number of astrocytes leads to more glutamate uptake from the extracellular fluid. This increase may be caused by the increase in sodium-dependent transporters EAAT1 and EAAT2 as the density of astrocytes is increased.

Figure 4.4 shows the morphological changes in co-culture consisting of various densities of glioma cells and normal brain astrocytes before and after preincubation with 100 uM glutamate.

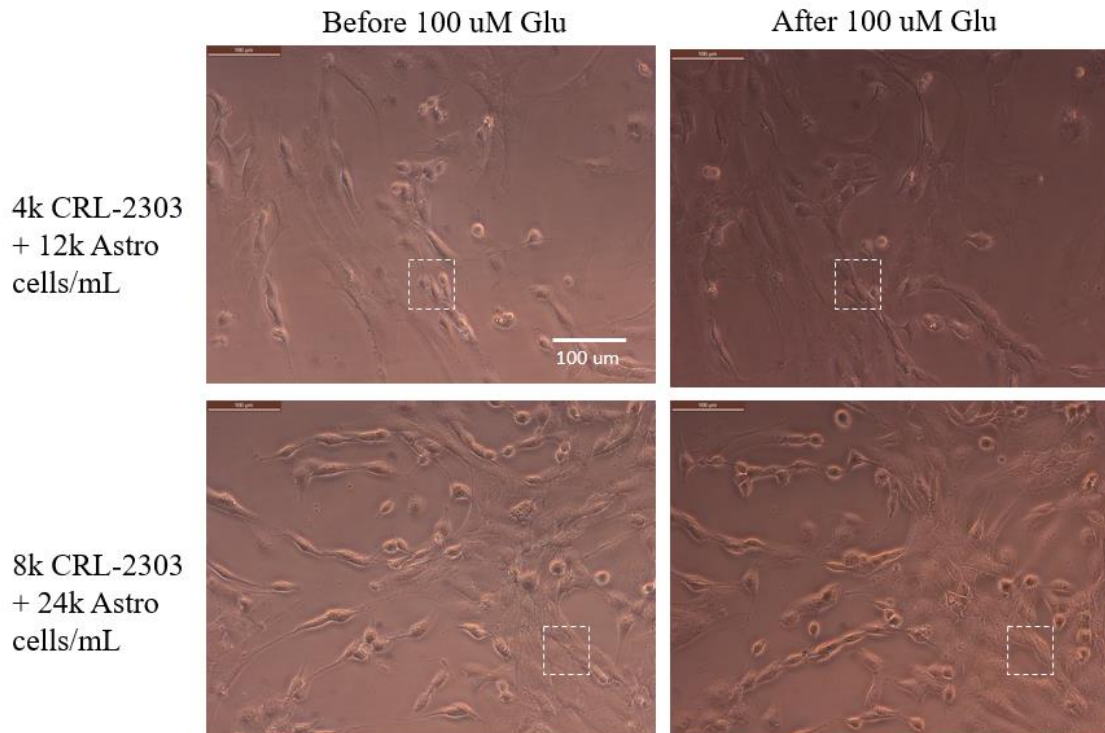


Figure 4.4: Microscopic images of co-culture of 4,000 glioma cells per mL and 12,000 normal brain astrocytes per mL, and 8,000 gliomas per mL and 24,000 normal brain astrocytes per mL at 3 days *in vitro* (div) before and after preincubation with 100 uM glutamate for 5 hr at 37 °C. Scale bar = 100 um. Dotted square lines mark the same area between the left and right image and show that the morphology of the cells remained the same before and after addition of 100 uM glutamate.

The addition of 100 uM glutamate did not lead to visible signs of cellular stress in co-culture after 5 hr. The slight change in cell morphology was attributed to the normal continued growth of the cells.

The glutamate uptake was repeated, as explained earlier, in a co-culture of normal brain astrocytes and glioma cells.

Figure 4.5 shows the glutamate uptake by different densities of normal brain astrocytes and co-culture of normal brain astrocytes and glioma cells.

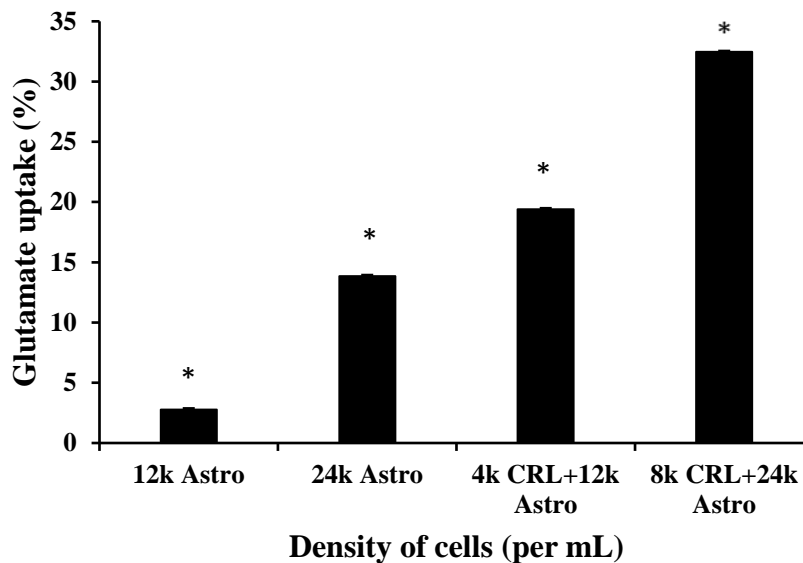


Figure 4.5: Percentage of glutamate uptake by different densities of normal brain astrocytes and glioma cells, 3 days *in vitro* (div) after preincubation with 100 μ M Glu for 5 hr at 37 °C. Error bars indicate standard deviation (SD); * $P < 0.05$, $n = 3$.

The uptake of glutamate by astrocytes after 3 div was 2.77% for cells seeded at 12,000 cells per mL and 13.85% for cells seeded at 24,000 cells per mL. The co-culture of 4,000 cells per mL CRL-2303 and 12,000 cells per mL astrocytes saw an increase in uptake of glutamate by seven-fold and reached 19.4% as compared to 12,000 cells per mL astrocytes alone. The co-culture of 8,000 cells per mL CRL-2303 and 24,000 cells per mL astrocytes had a glutamate uptake of 32.5% as compared to 12,000 cells per mL astrocytes alone. Surprisingly, the co-culture of astrocytes with brain tumor cells enhanced the uptake of glutamate. This enhancement indicates the complex interplay between upregulation of glutamate uptake and the composition of different cell types in co-cultures. In case of co-cultures, as the brain tumors progress, there might be more mass of cells and that might have affected the astrocytes. These data also suggest that the impaired uptake by gliomas might have caused the astrocytes to work harder in uptaking more glutamate.

4.3.2 Cell Metabolism

To study possible effects of glutamate on the cells, MTT assay was used to further examine the metabolism of cells. **Figure 4.6** shows the metabolism of cells with and without 100 μ M glutamate. The data show no significant difference in the metabolism of cells with and without 100 μ M glutamate.

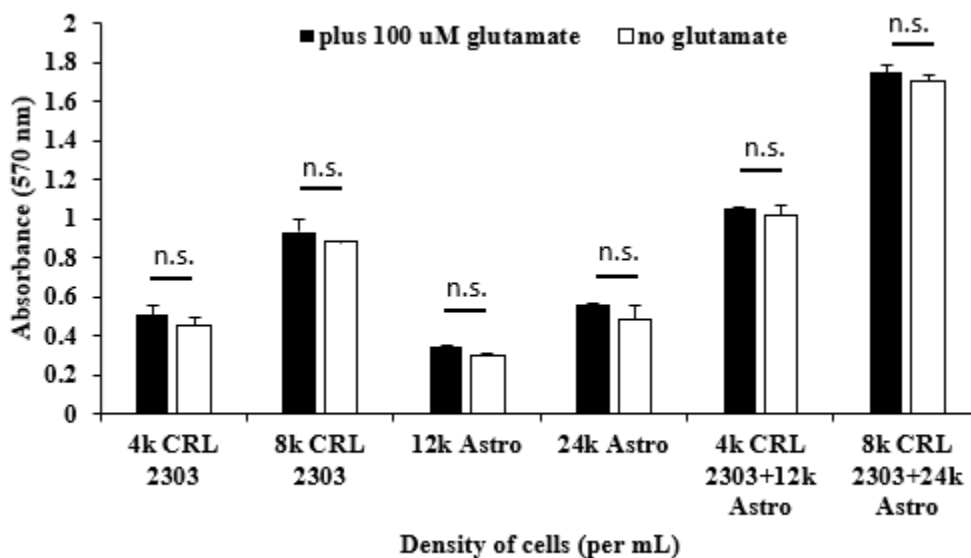


Figure 4.6: MTT assay as a measure of cell metabolism with and without 100 μ M glutamate. Error bars indicate standard deviation (SD); n.s.= not significant at $P < 0.05$, $n = 4$.

In all cases, the metabolism increased with seeding density. While the mean values of metabolism increased with the addition of glutamate, the effect was not statistically significant. This study indicates that the glutamate did not cause cell injury, and that glutamate was being taken up. Further, metabolism of glioma cells was higher than that of astrocytes, even with lower gliomas seeding density because the glioma cells have higher proliferation ability than astrocytes.

Next, the contribution of Na⁺-dependent transporters was examined for glutamate uptake. Sodium-dependent transporters were blocked by substituting choline for sodium in Locke's solution. An inverted microscope was used to examine changes in the morphology of astrocytes after the media was replaced with Locke's solution with and without sodium. Locke's solution with sodium chloride was used as the solution for sodium-containing media whereas choline chloride replaced sodium chloride for sodium-free media. **Figure 4.7** shows microscopic images of 3 days old astrocyte cells after placing them in the solution containing sodium and sodium-free media and incubated at 37°C and 5% CO₂ for 5 hr.

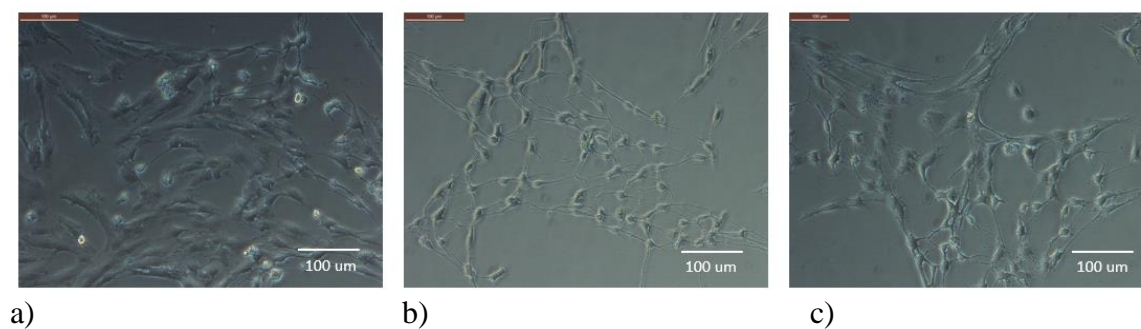


Figure 4.7: 5k/well normal brain astrocytes a) Control (Astrocyte medium), b) LKS (sodium chloride), c) LKS (choline chloride) at 3 days *in vitro* (div) post 5 hr after replacement of complete astrocyte media. Scale bar: 100 μm.

Morphological changes in the cells after replacement of complete astrocyte medium with solution containing sodium and sodium-free media for 5 hr indicated cell stress. The cell bodies shrank as they were exposed to prolonged incubation with Locke's solution with and without sodium.

4.4 Conclusion and Discussion

The morphology of both normal brain astrocytes and brain tumor cells from microscopic images captured before and after preincubation of 100 μ M glutamate for 5 hr suggests no signs of cell stress. The glutamate uptake by normal brain astrocytes was density dependent. As the number of normal brain astrocytes increased, the percentage of glutamate uptake escalated. It has been reported that the presence of GLAST on the cell surface of astrocytes increases the number of glutamate binding sites thereby speeding up the glutamate uptake [76].

Extracellular glutamate uptake was much smaller for glioma cells than for normal brain astrocytes. Results indicated that these type of glioma cells have minimum or no glutamate clearing capacity from the extracellular environment. This result was consistent with the findings as reported by Ye *et al.* [111], however, there was no glutamate release by glioma cells from our experiments. This might be due to the variation in glioma cell lines used by different research laboratories. As observed from the results from this study and from the previous chapter, it was concluded that tumor invasion is not necessarily linked with release of glutamate from gliomas. The impaired uptake of glutamate by glioma cells could be caused by mislocalization of glutamate transporters in cell nuclei. Moreover, co-culture of glioma cells with astrocytes showed enhanced uptake of glutamate by astrocytes as compared with uptake by astrocytes alone. The presence of glioma cells in a co-culture model may thus cause astrocytes work harder.

Glutamate tended to slightly increase the metabolism of cells. While the metabolism for glioma cells increased, astrocyte metabolism decreased, even though the density of astrocytes was more than glioma cells. Numerous studies have reported that

GLAST and GLT-1 are the major Na dependent transporters in astrocytes. Thus, complete media in astrocytes was replaced with Locke's solution with and without sodium. Interestingly, cell stress was observed in both conditions. The hypothesis for contribution of Na⁺-dependent transporters for glutamate uptake was tested, however, large changes in morphology of the cells prevented the results from being conclusive.

CHAPTER 5

APPROACHES FOR MODIFICATION OF BRAIN CELLS USING ENGINEERED MICRO/ NANOMATERIALS

5.1 Introduction

Many remarkable developments have been made in the field of micro- and nanotechnologies in the last few decades. The advances in micro- and nanotechnologies are expected to open new possibilities and applications in tissue engineering and drug delivery [113]. Apoptosis plays an important role in the developmental process of an organism. Apoptosis can be used as a tool for cell patterning to alter the tissue shape [114], [115]. A possible method by which to modulate apoptosis, and hence the morphological characteristics of brain cells is to use nanofilms created from materials such as copper nanoparticles (CuNps) and staurosporine (STS). STS is a non-specific protein kinase inhibitor which acts as a potent apoptotic stimulus [116]. These approaches will provide a better understanding on modifying the brain microenvironment.

Another method of changing the brain cell microenvironment is use of halloysite nanotubes (HNTs) as nanocontainers. Halloysite nanotubes are the aluminosilicate clay, chemically similar to kaolin, and found naturally in the earth in abundant quantities [117]. These nanotubes have outer diameter 50 ± 5 nm; inner lumen 10 - 15 nm; and length 1200 ± 300 nm. The outer surface of HNTs is composed of SiO_2 (negative charge)

and the inner core is composed of Al_2O_3 (positive charge). The hollow lumens of halloysites can load and then provide sustained release of biomacromolecules such as proteins, DNA, drugs, and antibacterial agents. As an example, they have been studied for delivery of the poorly soluble drug camptothecin, an anticancer drug, that is capable of causing apoptosis but that has been underutilized because it is poorly soluble in water [118]. In the current study, camptothecin (CPT) was loaded in the hollow lumen of HNTs, encapsulated them with natural polyelectrolytes using layer-by-layer (LbL) assembly and delivered them to glioma cells. In this experiment, engineered micro/nanomaterials CuNps, STS, and HNTs were used to modify the behavior of brain cells.

5.2 Materials and Methods

5.2.1 Creating Nanofilms

Nanofilms were fabricated in the center of a 24-well cell culture plate (Griener). Prior to fabrication, the center of the well was marked with a sharpie from the bottom of the well plate. Nanofilms were created by dropping 20 μL volume of nanomaterials such as CuNps and STS in the marked area and they were baked for 6 h at 37 $^\circ\text{C}$ in a laboratory oven (Quincy Lab, Inc, Model 10). After baking, the plates were stored in room temperature until cells were plated.

5.2.2 Chemicals

To create nanofilms, chemicals such as CuNps and STS were obtained from Sigma-Aldrich. For drug delivery, halloysite nanotubes were obtained from Henan Province of China. Camptothecin was obtained from MP Biomedicals, LLC, Santa Ana, California, USA, and dissolved in dimethyl sulfoxide (DMSO). Polyelectrolytes used in this study diethyl aminoethyl ethyl dextran (DEAE dextran), sodium alginate, poly-1-

lysine-block-co-polymer with polyethylene glycol (PLB), and Fluorescein isothiocyanate-PAH were purchased from Sigma-Aldrich. Other components used for this study such as DAPI (4',6-Diamidino-2-Phenylindole, Dihydrochloride), MTT were also purchased from Sigma Aldrich. All chemicals were used without any further processing. LUDOX TM 40 silica nanoparticles of diameter 5 nm were used to visualize polymer coating on halloysite nanotubes.

5.2.3 Preparation of Halloysite Drug Composites

12.5 mg of camptothecin were dissolved in 1 mL of DMSO to obtain saturated solutions. 25 mg of halloysite was added to this solution and mixed to obtain a homogeneous suspension. Aggregates were removed by sonicating for 5-10 min. The suspension was placed in vacuum for three 1 hr cycles, and then overnight to ensure maximum loading. The sample was removed and washed with ethanol to remove excess drug adsorbed. The sample was dried in a vacuum desiccator overnight and powdered. Drug loading efficiency was determined using thermogravimetric analysis.

5.2.4 LbL Assembly on Halloysite

2 mg/mL concentration of halloysite loaded with camptothecin was prepared in phosphate buffer saline (PBS). It was properly dispersed by sonicating for 5-10 min. Stock concentration of 30 mg/mL of DEAE Dextran, sodium alginate and PLB were individually prepared. The required amount of each polyelectrolyte was added to the halloysite mixture. It was then sonicated for 5 min and the zeta potential was measured to confirm complete charge reversal. No washing step was done after each layer was added, except for the last layer of PLB at 7000 rpm for 3 min.

5.2.5 Cell Culture

To testing the nanofilms, microglia (CRL-3265) were obtained from American Type Culture Collection (ATCC) and cultured in microglia media (**Appendix A, Section A.3**). Cells were placed on top of the baked nanofilms. For drug delivery tests, rat brain glioma cells (CRL-2303) were obtained from ATCC and cultured in CRL-2303 media (**Appendix A, Section A.1**). Cells were plated at a density of 10,000 cells per mL onto a 24-well cell culture plate and grown in an incubator at 37 °C in 5% CO₂. After two days, the cells were treated with various concentrations (1-5 ug/mL) of free drug (CPT) or layer-by-layer coated halloysites loaded with camptothecin. Morphological studies were carried out at 24 hr and 96 hr timepoints. MTT assay was performed each day until 192 hr. The cell culture media was not replenished during the entire experiment.

5.2.6 Microscopy

HNTs were imaged with both Scanning Electron Microscope (SEM) and Transmission Electron Microscope (TEM). Cells were imaged with light microscopy. The dried samples, prepared on silicon wafer, were gold sputter coated at 15mA for a thickness of ~10 nm and the nanotubes were observed under SEM, at 3 KV. Then, silica nanoparticles were coated on polyelectrolyte coated halloysite and, a diluted HNT suspension was placed onto formvar-coated copper grids (Agar), left to evaporate, and imaged with TEM at 120 V accelerating voltage. The microscopic images of cells were obtained with Leica DMI 6000B, captured every 24 hr after the cells were treated with samples to compare the morphological changes with the results from biochemical assays.

5.2.7 MTT Assay

The MTT assay has been described in Section 4.2.4.

5.3 Results

5.3.1 Creating Nanofilms

Nanofilms were created by dropping 20 uL volume of CuNps or STS in the marked area and baked for 6 h at 37 °C in a laboratory oven. **Figure 5.1** shows the drying pattern of CuNps under the inverted microscope.

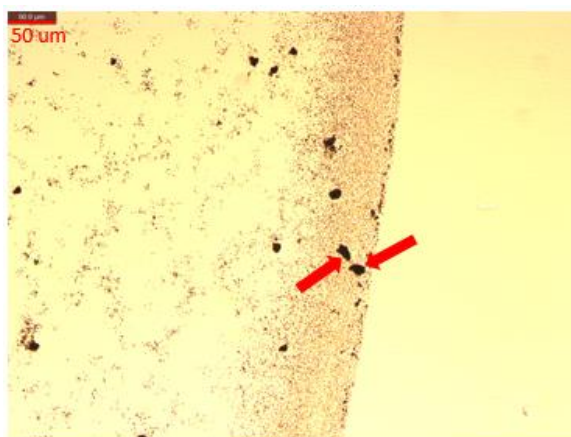


Figure 5.1: Drying pattern of 100 ug/mL CuNps nanofilms after baking for 6 hr. Red arrows indicate aggregates of copper nanoparticles. Scale bar = 50 um.

Since nanoparticles have very high surface area to volume ratio, nanofilms made of CuNps showed some agglomeration. Nanofilms made of STS were clear in color. After baking, microglia cells were placed on top of these nanofilms.

5.3.2 Effect of Nanofilms on Cells

Figure 5.2 shows phase contrast microscopy of microglia cells after they were seeded on top of the nanofilms created with 100 ug/mL copper nanoparticles or three concentrations of STS (500 nM, 1 uM, and 2 uM) at three timepoints (4, 24, and 48 hr).

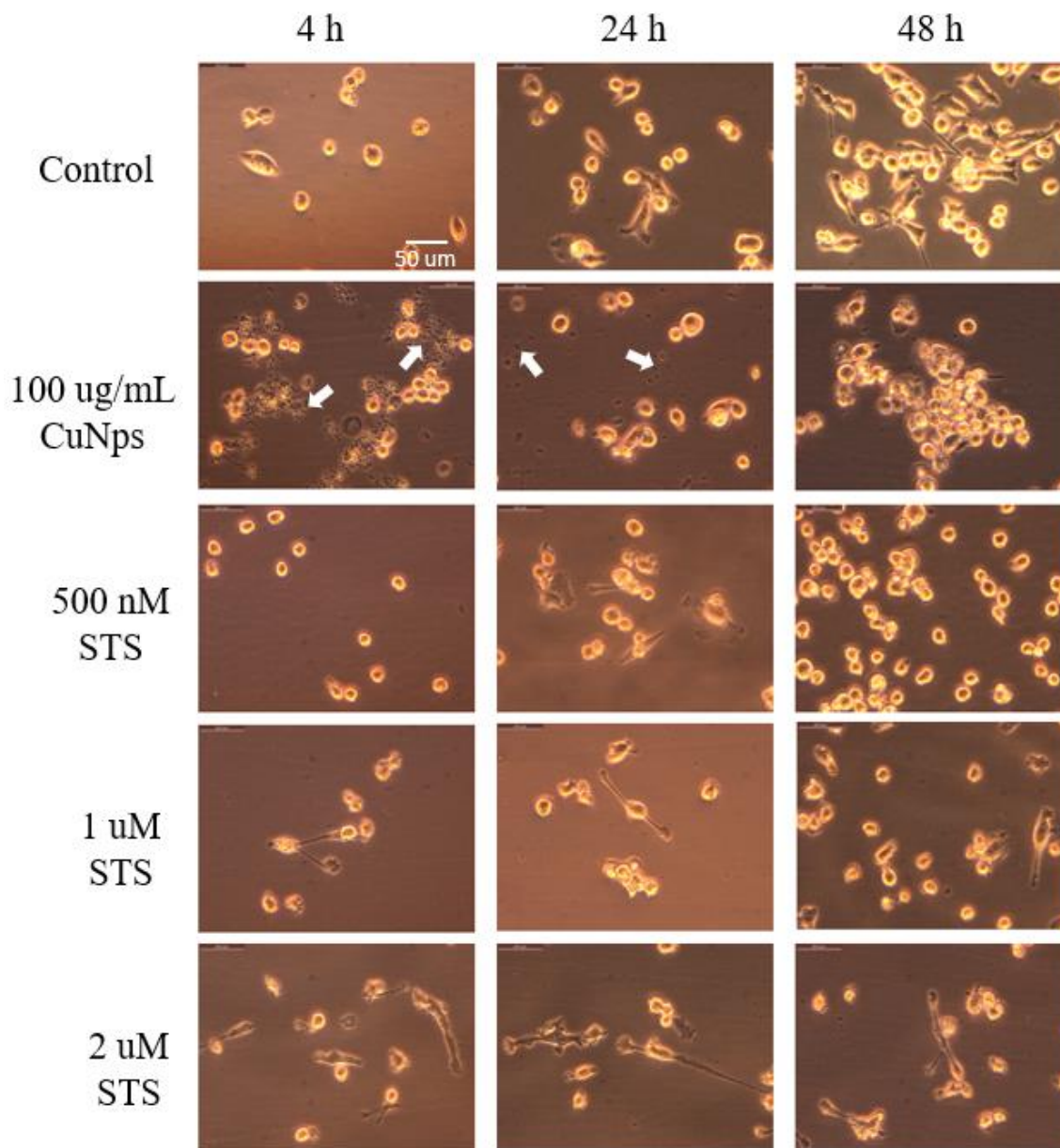


Figure 5.2: Representative images of microglia cells after they were seeded on top of the nanofilms created with 100 ug/mL CuNps or various concentrations of STS (500 nM, 1 uM, and 2 uM). The images were obtained using phase contrast microscopy at 4, 24, and 48 hr respectively. Scale bar = 50 um.

At 4 hr timepoint, the copper nanoparticles were still evident (**Figure 5.2**, second row) whereas they start clearing up after 24 hr and completely disappear at 48 hr. The

cells became more circular with no processes and more clumped at 48 hr as compared to 4 hr timepoint. The morphological differences are more pronounced for microglia cells treated with 1 μ M and 2 μ M STS as compared to the control at 4 hr. Cells treated with 500 nM STS exhibit few, relatively short but thick extensions at 24 hr but the processes disappear at 48 hr. In contrast, cells treated with 1 μ M and 2 μ M STS have large and thin processes with a branch-like appearance at all timepoints.

Figure 5.3 shows the phase contrast and fluorescence images of DAPI-stained nuclei of the cells treated with nanofilms made of control (water), 100 μ g/mL CuNps, 500 nM STS, 1 μ M STS, and 2 μ M STS. The number of nuclei decreased dramatically in the cells treated with 100 μ g/mL CuNps and the cells were clumped after 72 hr as compared to the control. Treatment with 500 nM STS slightly decreased the number of cells, whereas treatment with 1 and 2 μ M STS decreased the number of cells dramatically. However, cells treated with STS exhibited no clumping.

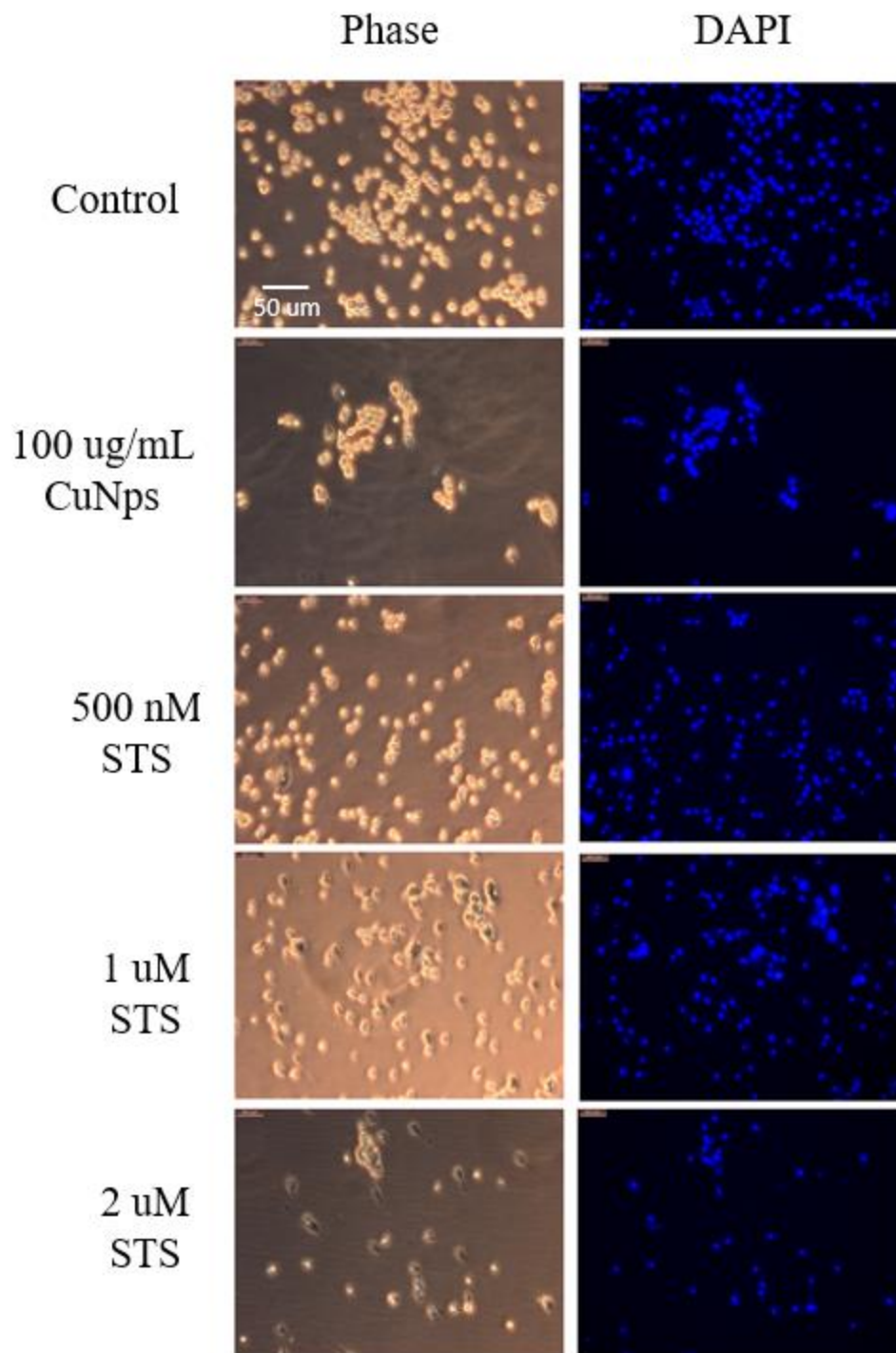


Figure 5.3: Phase contrast and fluorescence images of microglia after DAPI staining at 72 hr. 20,000 cells/mL were plated after creating nanofilms with 100 ug/mL CuNps (positive control) and different concentrations of STS (500 nM, 1 uM, and 2 uM). Scale bar = 50 um.

Table 5.1 shows the data obtained from the analysis of total number of objects, average area, average roundness, and NAF for microglial cells treated with nanofilms made of CuNps and various concentrations of STS after the nuclei were stained with DAPI. The total number of objects was the highest in the control. Although the total number of objects treated with 100 ug/mL CuNps was the least of all the conditions tested, the average area of the cells was relatively high. It was hypothesized that the cells treated with CuNps undergo necrosis, thereby causing an increase in cellular area. As a result, NAF increased, and higher NAF is an indicator of necrosis. NAF is given by the product of the average area and the average roundness of nuclei [99]. The number of objects decreased significantly when the cells were treated with 1 uM STS and 2 uM STS as compared to 500 nM STS. As the concentration of STS increased, the average area covered by the cells decreased. However, the roundness of nuclei did not change noticeably, although the morphology of the cells changed drastically with higher concentration of STS as mentioned earlier. NAF decreased in all three concentrations of STS as compared to control and 100 ug/mL CuNps. Thus, it can be concluded that STS induced apoptosis to the cells as NAF goes down during apoptosis.

Table 5.1: Analysis of total number of objects, average area, average roundness, and Nuclear Area Factor (NAF) (n = 6) for microglial cells treated with nanofilms made of CuNps and various concentrations of STS.

	No. of objects	Average Area	Average Roundness	NAF
Control	309	578	1.21	699
100 ug/mL CuNps	31	733	1.15	843
500 nM STS	231	494	1.13	558
1 uM STS	79	481	1.13	544
2 uM STS	66	463	1.14	528

5.3.3 Drug Delivery Using Halloysite Nanotubes

LbL-coated halloysite nanotubes were loaded with camptothecin in collaboration with Dr. Lvov's lab at Louisiana Tech University. **Figure 5.4 A-B** shows the schematic of halloysite nanotubes depicting their characteristics and dimensions. **Figure 5.4 C-D** shows the SEM and TEM images of halloysite nanotubes.

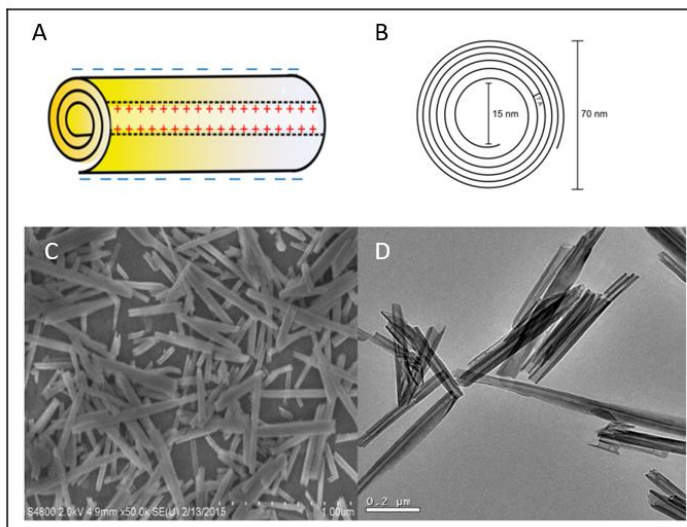


Figure 5.4: (A-B) Schematic of halloysite nanotube depicting characteristics and dimensions of halloysite nanotubes (C) SEM image of halloysite nanotubes (D) TEM image of halloysite nanotubes.

Figure 5.5 shows the schematics illustrating the loading of camptothecin inside the lumen of halloysite nanotubes followed by deposition of natural polyelectrolytes and FITC using layer-by-layer (LbL) technique and delivering them to brain tumor cells (CRL-2303).

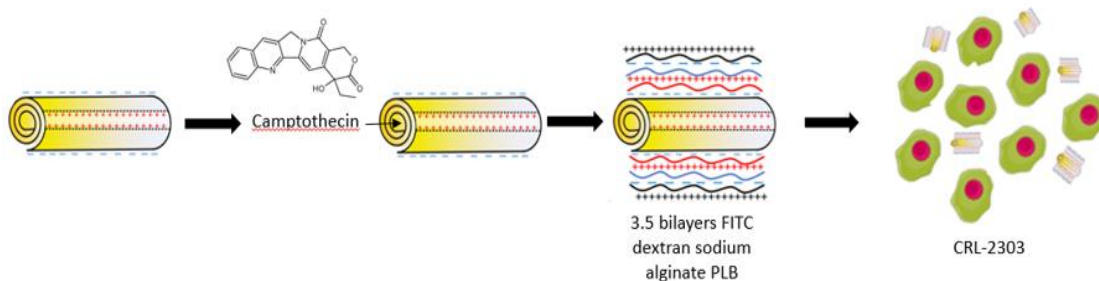


Figure 5.5: Schematics illustrating the loading of camptothecin inside the lumen of halloysite nanotubes followed by deposition of natural polyelectrolytes and FITC using layer-by-layer (LbL) technique and delivering them to brain tumor cells (CRL-2303).

Each polyelectrolyte (PE) was added using a non-washing method by slowly titrating the required amount for complete charge reversal. The alternation of positive and negative values of zeta potential confirms the shell formation on the surface of halloysite. Surface charge of ± 15 mV or above but below 40 mV is considered as complete charge reversal. To make the tracking of halloysite nanotubes easier, FITC-PAH was added as first layer to aid in fluorescent imaging. Silica nano particles were diluted from a stock solution (5%) to prevent their coating in excess. A change in surface charge to negative was observed after the addition of silica.

Alternation of negative and positive values of zeta potential confirm layer by layer assembly. Zeta potential measurements indicated a change in surface charge from -30 mV in pristine halloysites to +23 mV in final cationic layer.

Figure 5.6 shows the zeta potential values after the addition of each polyelectrolyte layer showing charge reversal.

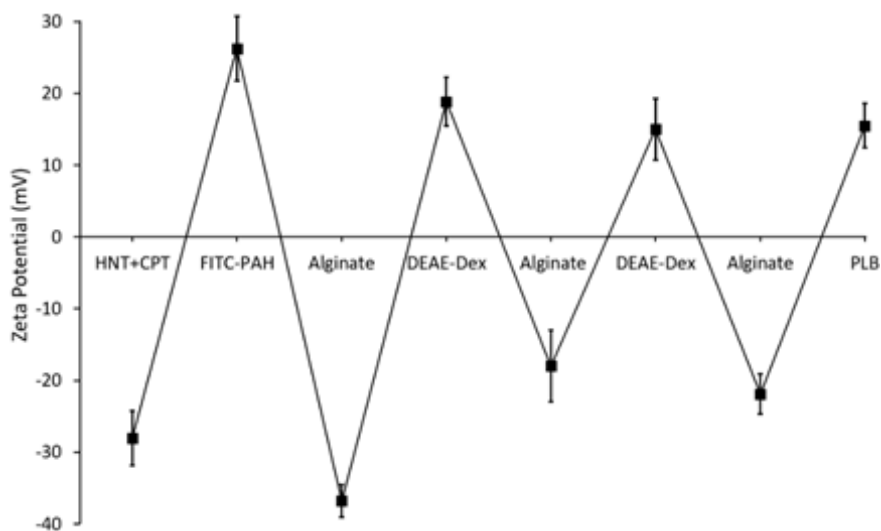


Figure 5.6: Zeta potential values after the addition of each polyelectrolyte layer showing charge reversal.

To demonstrate that the halloysite nanotubes are concentrated in or on cancer cells, HNTs coated with natural polyelectrolytes labelled with FITC were visualized under fluorescent microscope. Further, the nuclei of cancer cells were stained with DAPI, a fluorescent dye. The photomicrographs of FITC labelled HNTs coated with natural polyelectrolytes were merged with DAPI-stained nuclei and it was evident that the halloysites were present in or on cancer cells as shown in **Figure 5.7**. The FITC was very near the DAPI, and the FITC labelled halloysites were intact despite various washing/staining steps.

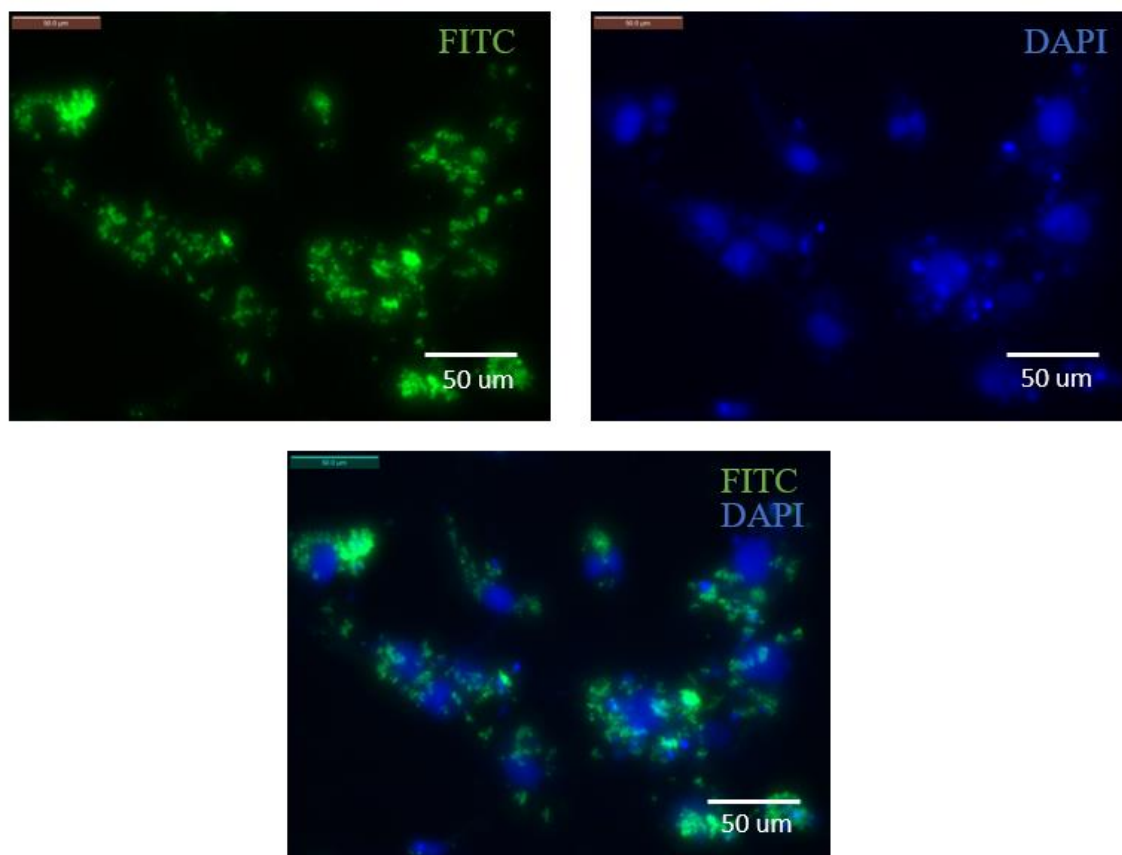


Figure 5.7: FITC labelled HNTs coated with natural polyelectrolytes (5 ug/mL); DAPI staining of CRL-2303; Merged image of FITC and DAPI shows localization of HNTs in or on the nuclei. Images were taken 120 hr after addition of FITC labelled HNTs coated with natural polyelectrolytes to CRL-2303 cells. Scale bar = 50 um.

Cell morphological changes were studied after microscopic pictures were captured for 96 hr. **Figures 5.8** and **5.9** show that the cells treated with both concentrations of bare HNT continued to grow and proliferate until 96 hr, whereas growth of cells treated with CPT, HNT-CPT, Nat LbL HNT-CPT was inhibited.

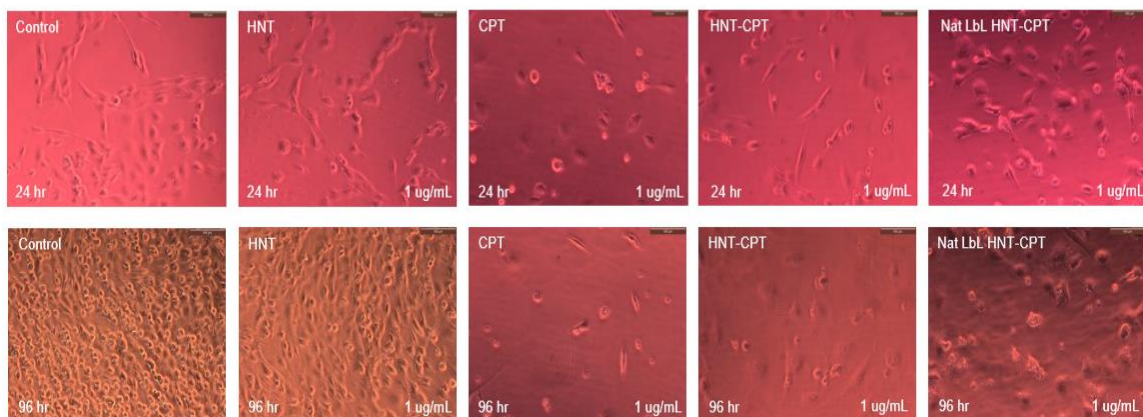


Figure 5.8: Effect of 1 $\mu\text{g}/\text{mL}$ concentration of HNT, CPT, HNT-CPT, and Nat LbL HNT-CPT on CRL-2303 cells after 24 hr (top) and 96 hr (bottom). Images shown are representatives of multiple wells ($n = 3$) and multiple platings of cells for each condition tested. Scale bar = 100 μm .

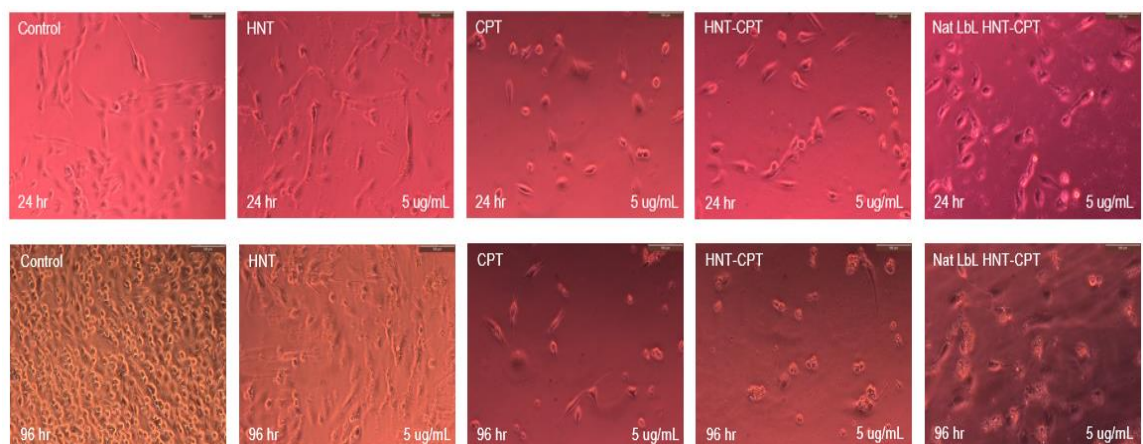


Figure 5.9: Effect of 5 $\mu\text{g}/\text{mL}$ concentration of HNT, CPT, HNT-CPT, and Nat LbL HNT-CPT on CRL-2303 cells after 24 hr (top) and 96 hr (bottom). Images shown are representatives of multiple wells ($n = 3$) and multiple platings of cells for each condition tested. Scale bar = 100 μm .

Figure 5.10 shows the viability assay demonstrating the long-term sustained release of anticancer drug (camptothecin) from encapsulated HNTs coated with natural polyelectrolytes using LbL technique in glioma cells. Cells treated with HNT decreased

sharply after 120 hr. This downturn was because the cells reach confluency and they begin to rip off from the cell culture plate as the media was not replenished. Cells treated with free drug (CPT) fail to suppress the activity of cancer cells and the cells try to bounce back. However, in comparison to CPT, Nat LbL HNT-CPT at submaximal killing concentrations (1 ug/mL) sustained suppression of glioma cell growth *in vitro* after the initial burst of inhibition.

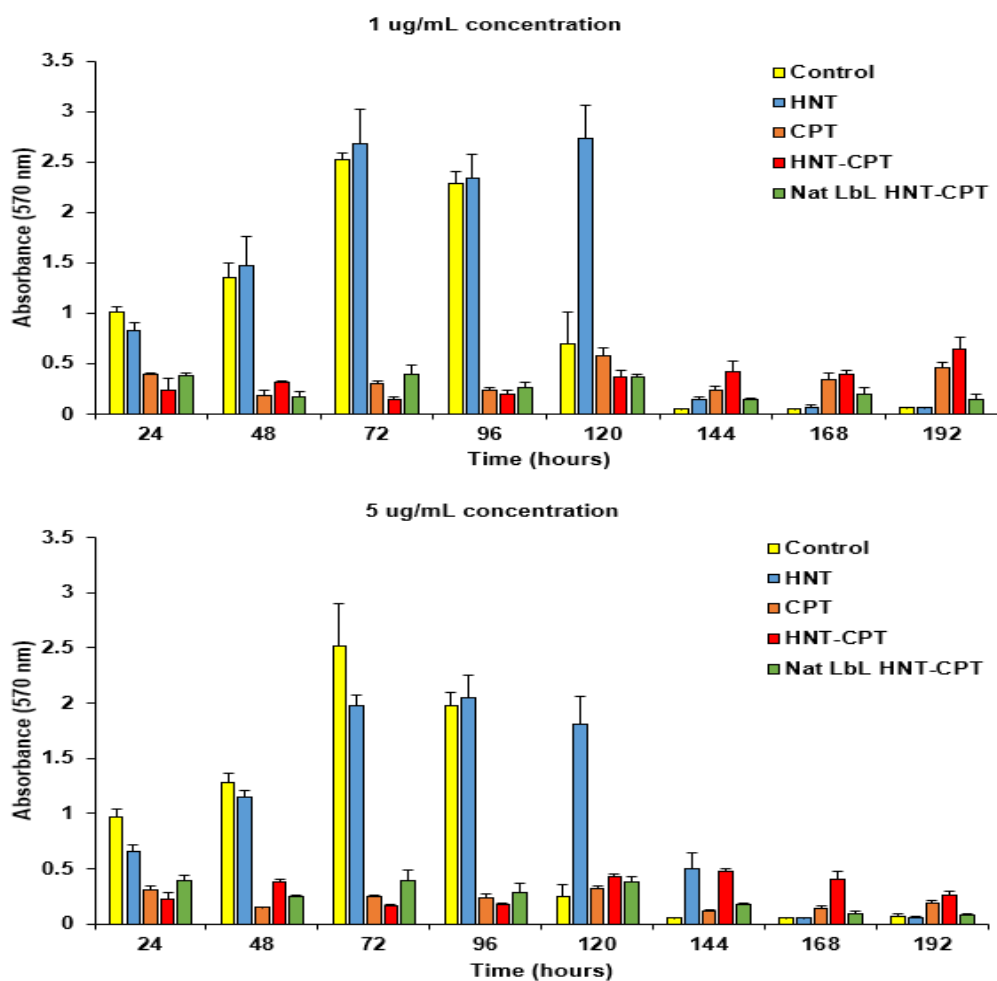


Figure 5.10: Viability assay of the long-term sustained release of anticancer drug (camptothecin) from encapsulated HNTs coated with natural polyelectrolytes using LbL technique in glioma cells.

5.4 Conclusions

Cell patterning can be achieved by inducing apoptosis as it modifies the morphological characteristics of brain cells. Here, engineered micro/ nanomaterials such as nanofilms created from CuNps and STS were used to modify brain cells. The nanofilms developed in this project allow to create boundaries, thus eliminating the need to work with the entire well as opposed to working with soluble drugs. These approaches will provide with a better understanding to change the brain microenvironment. From the calculations of NAF, we concluded that positive control (CuNps) used in this experiment caused cell death by necrosis whereas STS caused cell death by apoptosis.

Another example to change the brain cell microenvironment is using halloysite nanotubes as nanocontainers for delivery of the poorly soluble drug camptothecin. Camptothecin, an anti-cancer drug, can be loaded into the hollow nanotubes, and delivered to cancer cells. Results showed that the surface of halloysite nanotubes can be modified using natural polyelectrolytes. *In vitro* studies in cancer cells further verified that the camptothecin loaded LbL coated halloysite nanotubes show great potential for long-term release of drugs.

CHAPTER 6

POTENTIAL APPLICATIONS OF COPPER CONTAINING HIGH ASPECT RATIO STRUCTURES (CUHARS) FOR BIOMEDICAL PURPOSES

6.1 Introduction

In this chapter, the potential applications of a novel biohybrid material discovered in Dr. Decoster's laboratory at Louisiana Tech University which was named Copper containing High Aspect Ratio Structures (CuHARS) will be studied. CuHARS consist of copper and an amino acid cystine [120], and they are assembled using a bottom up approach in aqueous solution under physiological conditions [121].

Cellulose, the most abundant polysaccharide on earth, are used as scaffolds for tissue engineering, *in vitro* testing of cell models and for other medical purposes [122], [123]. Here, incorporation of CuHARS into cellulose was demonstrated to construct stable matrix for CuHARS delivery in glioma cells. Additionally, magnetically susceptible materials such as iron oxide nanoparticles ($\text{Fe}_2\text{O}_3\text{NPs}$) with CuHARS-cellulose matrix was used to spatially control CuHARS delivery.

Recently, a technique to break down CuHARS using sonication was developed, thus obtaining uniform sized CuHARS with nano-features. The interaction of sonicated CuHARS was tested in the co-culture model that we developed earlier. It was hypothesized that sonicated CuHARS are non-toxic to cells. Furthermore, degradation of

CuHARS was demonstrated for the first time in a co-culture model consisting of glioma cells and normal brain astrocytes.

6.2 Materials and Methods

6.2.1 Materials and Reagents

Whatman filters (grade-1) 32 mm with 11 μm pores were obtained from VWR. TEMPO (2,2,6,6-tetramethylpiperidine-1-oxyl (98%), sodium bromide, sodium hypochlorite (reagent grade, available chlorine 10-15%), $\text{Fe}_2\text{O}_3\text{NPs}$ (<50 nm), copper sulfate, cystine, and NaOH were from Sigma-Aldrich (St. Louis, MO, USA).

6.2.2 Sonication of CuHARS

CuHARS were synthesized with copper sulfate as starting material and cystine as the amino acid [120], [124]. Synthesis was carried out in liquid under biological conditions (37 °C) and the composites are formed by self-assembly process. Synthesized CuHARS mixtures were transferred to 0.65 mL microcentrifuge tubes (VWR, Catalog number 87003-290). They were sonicated for 20 min in Branson 1510 ultrasonic cleaner.

6.2.3 Generation of Cellulose Films and Cellulose Hybrid Materials

Cellulose fibers were obtained by TEMPO mediated oxidation from Whatman filters following the procedure described by Saito *et al.* [125]. Briefly, the filters (1 g) were suspended in 100 mL of water and converted into a pulp using a domestic blender, and then 16 mg of TEMPO and 100 mg of sodium bromide were added to the pulp under magnetic stirring at 400 rpm. The TEMPO mediated oxidation was started by adding 9 mL of sodium hypochlorite solution dropwise and the pH was maintained at 10 by adding 0.5 M NaOH solution. The process was maintained for 4 hr. The TEMPO-oxidized cellulose fibers were then centrifuged at $9,000\times g$ relative centrifugal force (rcf) for 4 min.

The resulting fibers were resuspended in water and centrifuged as above as a washing step and this process was repeated twice. Next, the fibers were resuspended in water to a concentration of around 0.4% w/v, and blended for about 1 hr to produce the mechanical defibrillation of the cellulose pulp. Finally, the suspension was centrifuged at 2,000 rcf for 4 min to remove the thicker fibers. After this process, the final concentration of the suspension was 0.3% w/v. The cellulose suspension was stored at 4° C before further experiments were carried out. The carboxyl content was determined by means of conductometric titration with 0.04 M NaOH, using a Pt conductivity cell 50-70 and GLP 31 conductivity meter from Crison, and it was found to be 1.41 mmol carboxylic groups per gram of cellulose.

The biohybrid cellulose/nanoparticles films were prepared by mixing the cellulose fibers dispersion with diverse nanomaterials to construct solid biohybrid films by simple casting and drying. Cellulose/CuHARS materials were prepared by dispersing 0.5 mL of a 1 mg/mL CuHARS solution in 4 mL of 0.3% w/v cellulose suspension. The mixture was vortexed for homogenization, and 4 mL of this liquid mixture was then placed/well in one or more of the wells of a 12-well suspension plate (Greiner) and dried in the oven at 37° C for 48 hr to produce cellulose/CuHARS biohybrid films. The content of CuHARS nano- and micro-materials in the films is about 4% of the total mass. Similarly, cellulose/CuHARS/Fe₂O₃ materials were prepared by addition of 0.5 mL of previously sonicated Fe₂O₃ nanoparticles (1 mg/mL solution) together with the CuHARS into the cellulose dispersion. In this case, the films were loaded with 3.8% CuHARS and 3.8% Fe₂O₃ nanoparticles with respect to the total mass.

6.2.4 Cell Culture

CRL-2303 glioma cells were plated at 20,000 cells/well on a 24-well cell culture plates. Cells were allowed to attach to well plates and were incubated for up to 74 h under physiological conditions in 37 °C, 5% CO₂, humidified incubators. The stability of constructed cellulose-CuHARS matrix was tested in these cells. For degradation studies, a co-culture experimental model was developed as described in Chapter 3.

6.2.5 Digital Microscopy Imaging

All images were obtained using a Leica DMI 6000B inverted microscope. Since the cellulose matrix biofilms were slightly above the Z-axis focal plane compared to the underlying cell culture area, images shown for matrix cell interactions were composed by carrying out a digital overlay function using Adobe Photoshop (Version 6.0.1). One digital image focused at the Z-plane of the cellulose matrix, and another digital image focused at the plane of the cells were combined by digital overlay.

6.2.6 Image Analysis

The software Image Pro-Plus version 7.0, developed by Media Cybernetics, was used for image analysis. Histograms were created to analyze the size distribution of different concentrations of CuHARS at various timepoints.

6.3 Results

6.3.1 Integration of CuHARS with Cellulose and Magnetic Susceptible Nanoparticles

CuHARS and Fe₂O₃NPs were incorporated into porous, non-degradable cellulose to further spatially control CuHARS delivery and CuHARS density in two and three dimensions. CuHARS-cellulose matrices were constructed using a liquid/pulp phase, and

then dried them into stable, solid films which could be easily handled (**Figure 6.1 a**). Furthermore, biohybrids of the cellulose matrix that incorporate both $\text{Fe}_2\text{O}_3\text{NPs}$ and CuHARS remained magnetically susceptible to a permanent bar magnet for at least 8 months after the fabrication of the material (**Figure 6.1 b**).

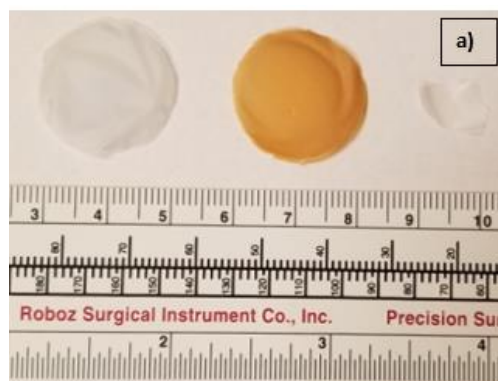


Figure 6.1: Panel (a) Cellulose matrix at the macroscale, showing from left to right, cellulose biohybrids incorporating CuHARS, $\text{Fe}_2\text{O}_3\text{NPs}/\text{CuHARS}$, and cellulose alone, respectively. The 3rd sample (rightmost sample) is a fragment of the constructed cellulose matrix alone. Metric scale below the matrix discs indicates diameter of approximately 2 cm for each disc. Panel (b) Cellulose matrix sample incorporating susceptible $\text{Fe}_2\text{O}_3\text{NPs}/\text{CuHARS}$ suspended by a permanent bar magnet.

Microscopic digital imaging of the constructed biohybrid cellulose matrices demonstrated curved, more transparent cellulose fibers integrated with straight, dark high-aspect ratio structures which were identified as the CuHARS component. As previously shown [101], the contrast provided by the copper component of CuHARS causes the material to stand out well against white light backgrounds. This contrast was confirmed in the current work upon integrating CuHARS into cellulose matrices, which were sufficiently thin to pass light, and reveal both cellulose fibers and the straight, dark contrasting CuHARS components as shown in **Figure 6.2**. Although cellulose nanofibers that produce highly transparent films were not used, the type of cellulose used in this work gives rise to films with a sufficient degree of transparency for visualization using inverted white light microscopy. A 0.1% suspension of this cellulose shows a transmittance of around 30% at 600 nm due to light scattering, as it is composed of a mixture of micro- and nano-fibers (data not shown). Nevertheless, its preparation has the advantage of being less time and energy consuming than for nanofibers, and it gives rise to films with enough quality.

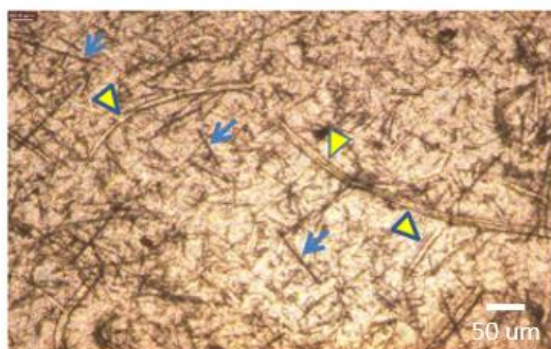


Figure 6.2: Incorporation of cellulose with CuHARS. Blue arrows indicate CuHARS (dark and straight structures), and yellow arrowheads indicate cellulose fibers (light, curved structures). Image obtained using inverted light microscopy. Scale bar = 50 μm .

6.3.2 Application of Constructed Cellulose Materials to Aqueous Solutions

The stability of constructed cellulose materials for potential environmental and biomedical applications in aqueous environments was tested by placing pieces of constructed films into water and cell culture media. Films were successfully constructed that provided sufficient porosity for the materials to be wettable and easily immersible in the liquid of interest (non-floating). The stability of constructed films in aqueous environments led to next test if the CuHARS-cellulose and other constructed films were compatible with *in vitro* cell culture systems. As shown in **Figure 6.3**, fast-growing brain tumor cells were used as a model for assessment, and they demonstrated that constructed films could be placed within cell culture plates for testing purposes. Since the cellulose films are easily wettable, but still somewhat mobile within the media-containing wells, the cut pieces of film still move around to some extent. Additionally, since the films settle on top of the cells, images were constructed from these *in vitro* experiments by digitally overlaying the Z-plane of focus for the films with the Z-plane focus for the cells, for the same field of view for a given image (**Figures 6.3, 6.4, and 6.5**).

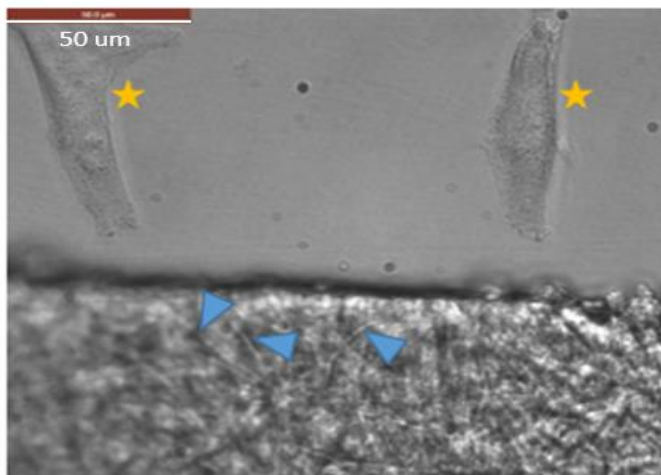


Figure 6.3: Cellulose films testing with cells in defined microenvironments. Cellulose matrix materials alone were tested for compatibility with cell culture conditions. The bottom portion of the image shows the cellulose matrix and top portion shows brain tumor cells. Blue arrowheads indicate cellulose fibers and stars indicate edges of glioma cells. Scale bar = 50 μm .

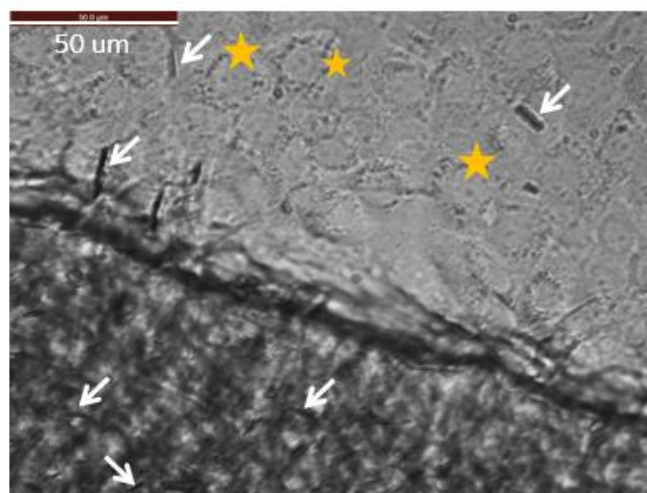


Figure 6.4: Cellulose films testing with cells in defined microenvironments. Cellulose-CuHARS biohybrids. The bottom portion shows the cellulose-CuHARS matrix and the top portion shows glioma cells with some released CuHARS. To evaluate integration into the matrix of smaller size biohybrids, CuHARS were sonicated as previously described [120] before they were combined with cellulose. White arrows indicate CuHARS and stars indicate edges of glioma cells. Scale bar = 50 μm .

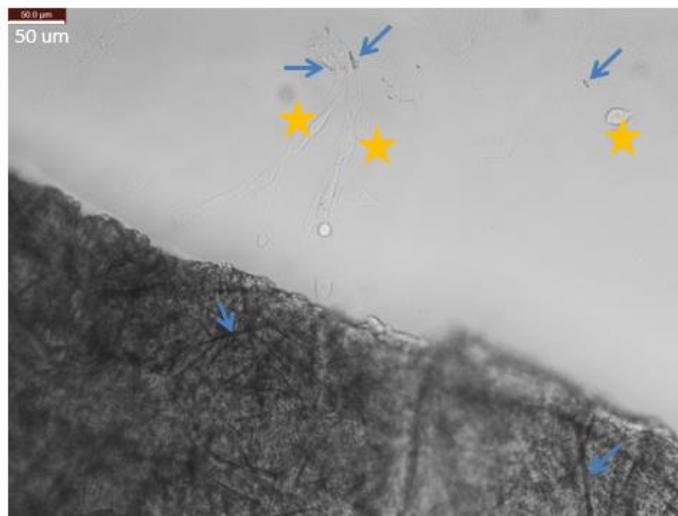


Figure 6.5: Cellulose-CuHARS-Fe₂O₃NPs biohybrids. Bottom portion shows the cellulose-CuHARS-Fe₂O₃NPs matrix and top portion shows glioma cells with some released CuHARS. For these integrated hybrids, CuHARS were not sonicated before mixing with cellulose. Therefore, some very long CuHARS were successfully integrated into the cellulose matrix, as indicated. Blue arrows indicate CuHARS and stars indicate edges of glioma cells. Scale bar = 50 μm.

6.3.3 Cellular Interaction of Sonicated CuHARS in a Co-culture Model

Sonicated CuHARS were tested for their toxicity and degradation in the co-culture model developed earlier. **Figures 6.6 - 6.11** are the microscopy images of interaction of co-culture with 1 μg/mL, 5 μg/mL, and 10 μg/mL sonicated CuHARS respectively. Images using bright field microscopy were obtained because the copper component of CuHARS stands out well and it is easier for image analysis. Morphological changes in cells were viewed in images taken using phase contrast microscopy.

Figure 6.6 shows phase contrast microscopy images from a co-culture of normal brain astrocytes and glioma cells over 72-hr timepoint. The microscopic images of control cells show proliferation over time and the cells appear to be healthy.

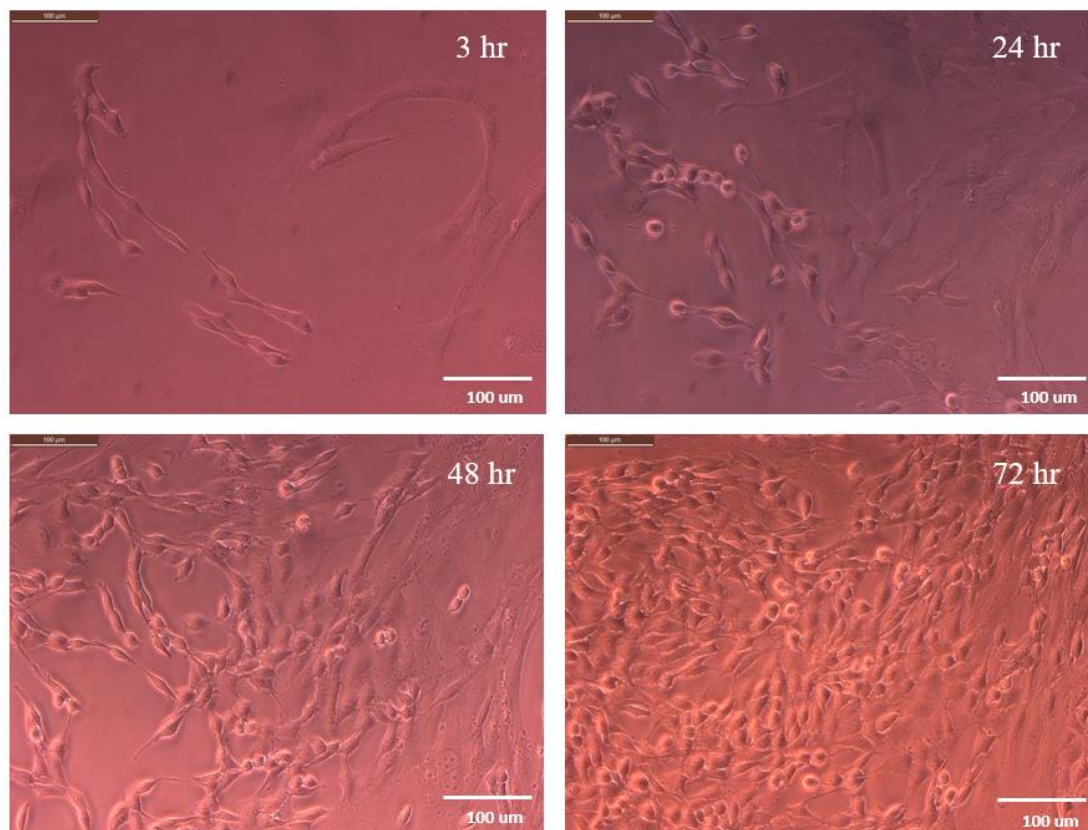


Figure 6.6: Phase contrast microscopy images of a co-culture experimental model with 1:3 ratio of glioma cells and normal brain astrocytes at 3, 24, 48, and 72 hr timepoints. Scale bar = 100 μm .

Figure 6.7 shows phase contrast images in a co-culture experimental model with 1 $\mu\text{g/mL}$ sonicated CuHARS. No obvious morphological differences are apparent between this figure and **Figure 6.6**, without CuHARS.

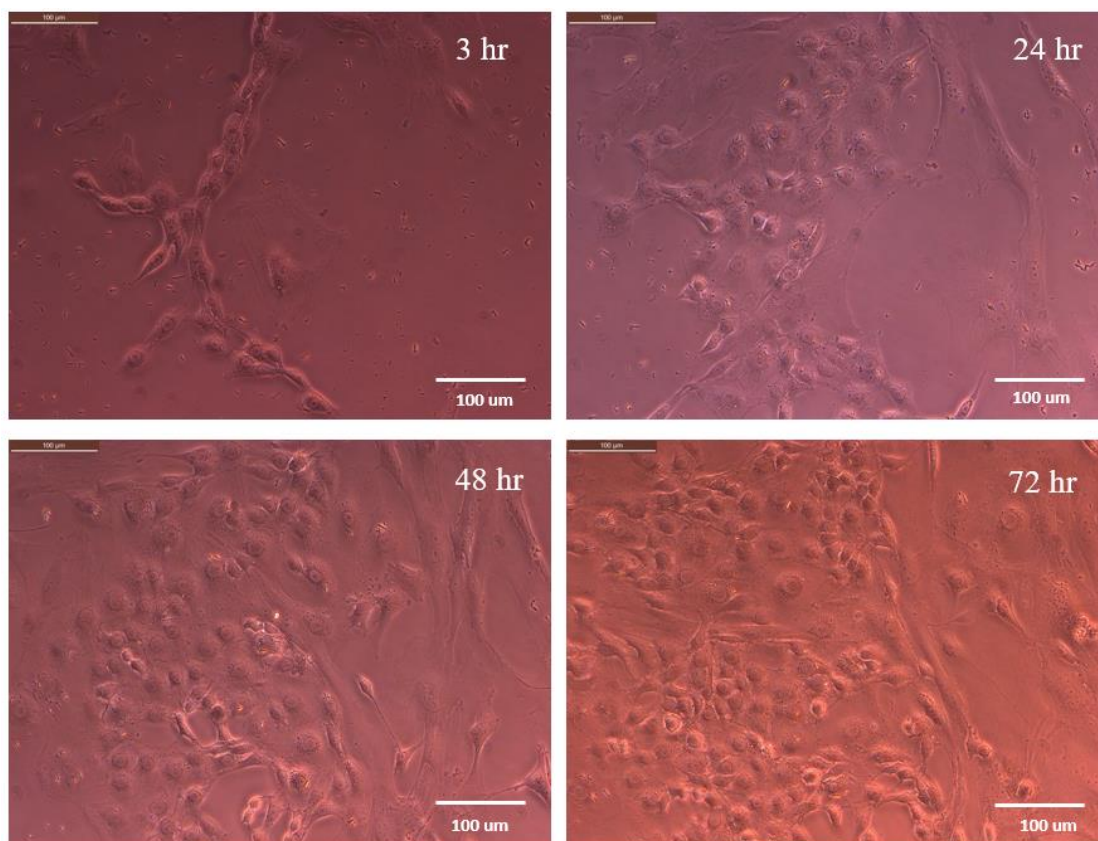


Figure 6.7: Phase contrast microscopy image of a co-culture of normal brain astrocytes and glioma cells with 1 ug/mL concentration of sonicated CuHARS at 3, 24, 48, and 72 hr timepoints. Scale bar = 100 um.

The co-culture with 1 ug/mL CuHARS is also shown in brightfield as shown in **Figure 6.8**. The CuHARS were evenly distributed throughout the wells and they degraded slowly over time. No clumping of sonicated CuHARS was noticed at any of the timepoints in 72 hr period.

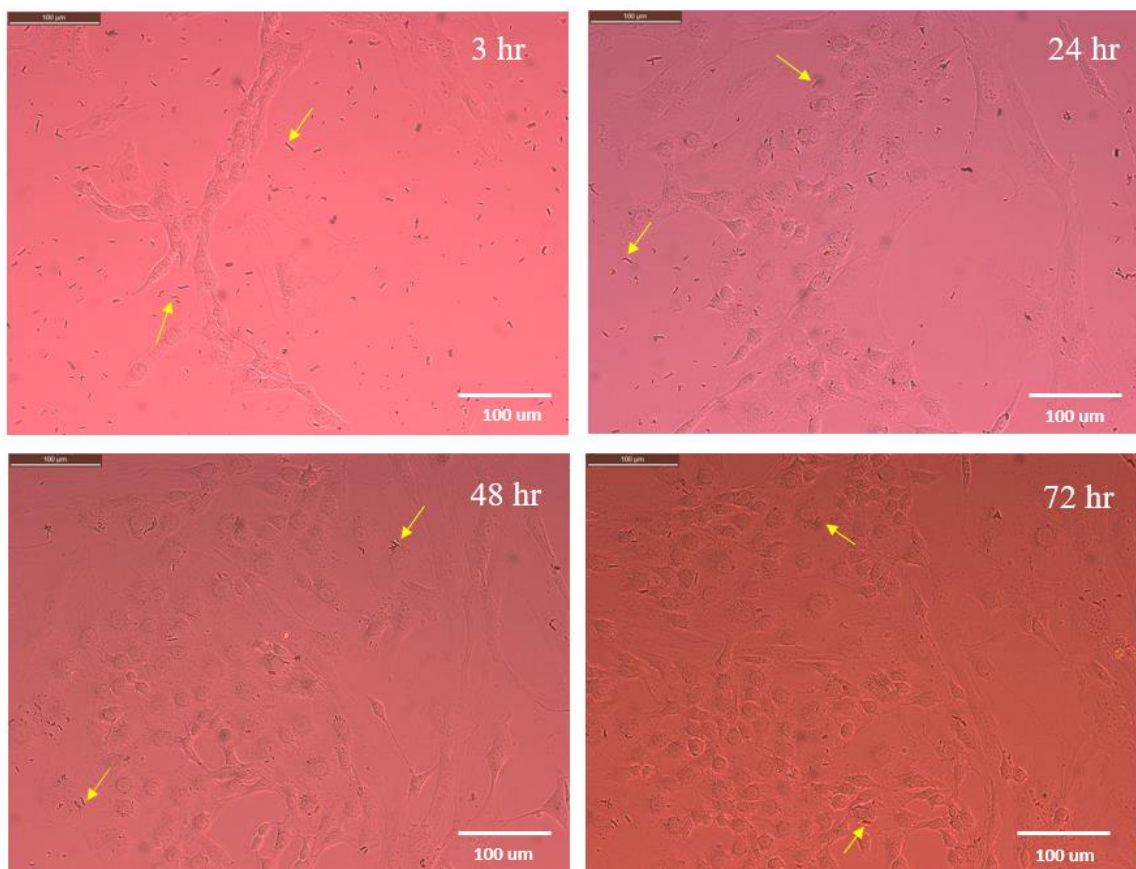


Figure 6.8: Bright field microscopy image of a co-culture of normal brain astrocytes and glioma cells with 1 ug/mL concentration of sonicated CuHARS (yellow arrows) at 3, 24, 48, and 72 hr timepoints. Scale bar = 100 um.

Figure 6.9 shows phase contrast images in a co-culture experimental model with the concentration of sonicated CuHARS increased to 5 ug/mL.

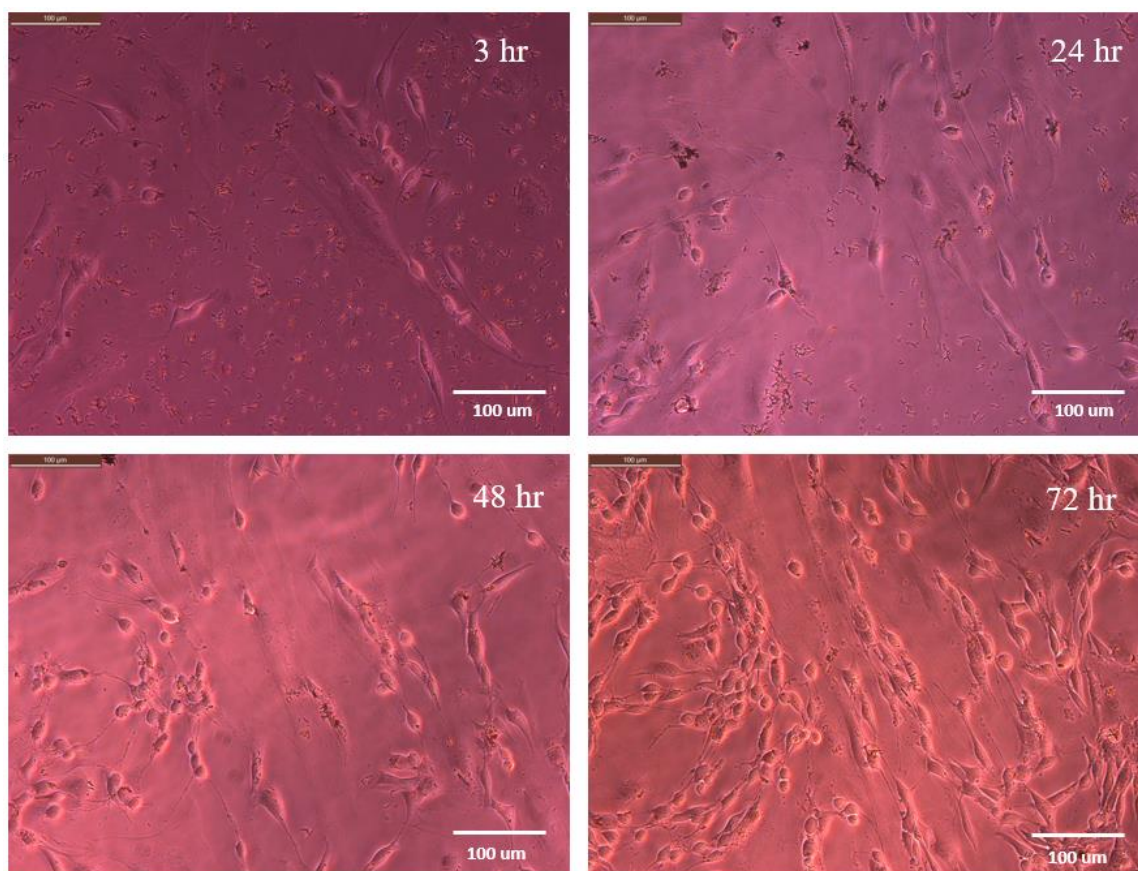


Figure 6.9: Phase contrast microscopy image of a co-culture of normal brain astrocytes and glioma cells with 5 ug/mL concentration of sonicated CuHARS at 3, 24, 48, and 72 hr timepoints. Scale bar = 100 um.

The brightfield images for the co-culture experiment with 5 ug/mL CuHARS is shown in **Figure 6.10**.

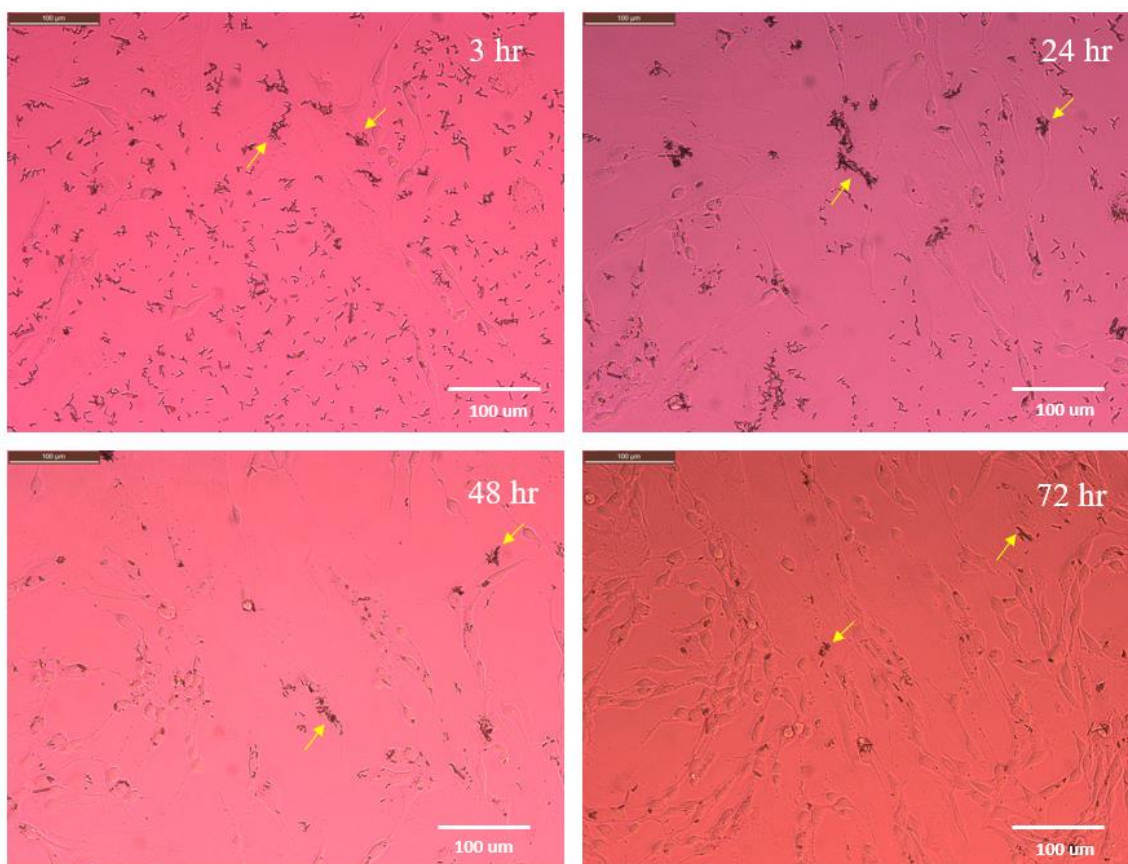


Figure 6.10: Bright field microscopy image of a co-culture of normal brain astrocytes and glioma cells with 5 µg/mL concentration of sonicated CuHARS (yellow arrows) at 3, 24, 48, and 72 hr timepoints. Scale bar = 100 µm.

Figure 6.11 shows phase contrast images in a co-culture experimental model with the concentration of sonicated CuHARS increased to 10 µg/mL. At 72 hr, the area coverage by cells was less than it was at the other concentrations of sonicated CuHARS, indicating that high concentrations of CuHARS could be toxic to cells.

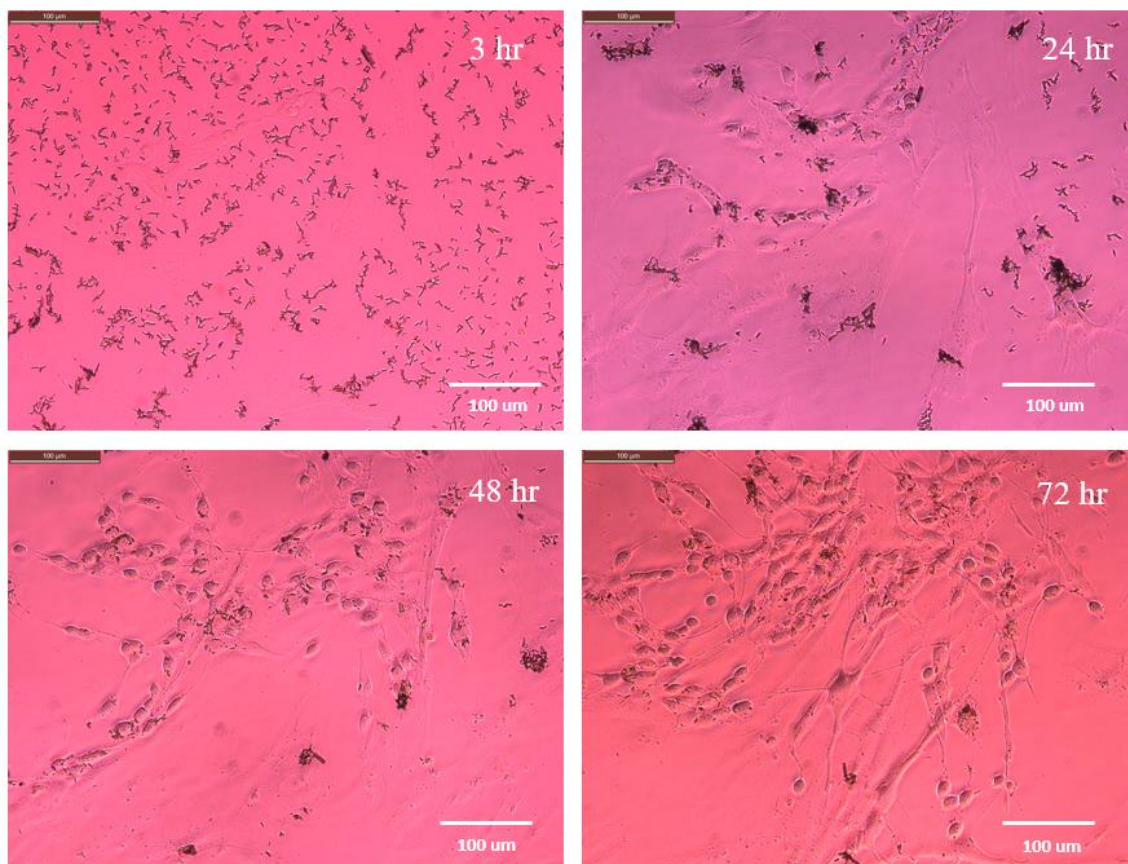


Figure 6.11: Phase contrast microscopy image of a co-culture of normal brain astrocytes and glioma cells with 10 ug/mL concentration of sonicated CuHARS at 3, 24, 48, and 72 hr timepoints. Scale bar = 100 um.

Figure 6.12 shows bright field images in a co-culture experimental model with the concentration of sonicated CuHARS at 10 ug/mL.

CuHARS were mostly seen in the areas with no cells at 3 hr with a little clumping, but at 48 hr clumping was seen, mostly on the cells. CuHARS degraded slowly from 24 hr to 72 hr.

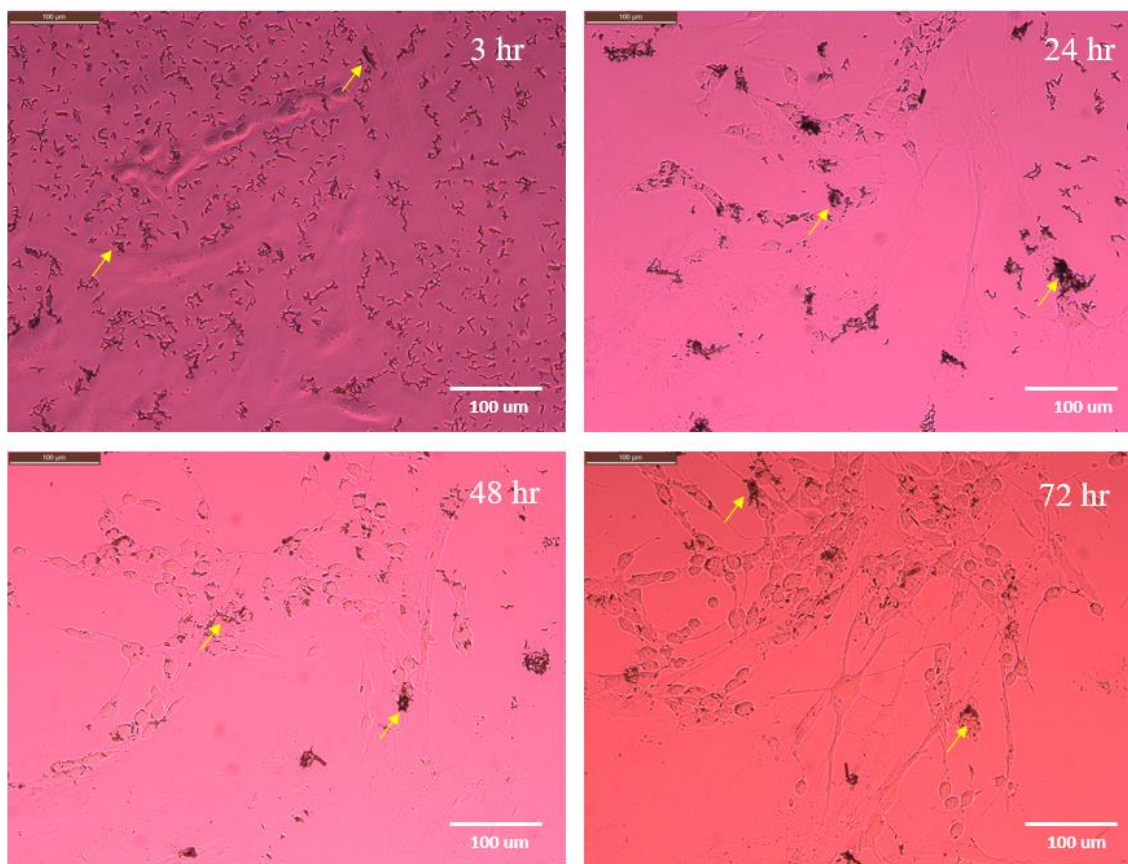


Figure 6.12: Bright field microscopy image of a co-culture of normal brain astrocytes and glioma cells with 10 ug/mL concentration of sonicated CuHARS (yellow arrows) at 3, 24, 48, and 72 hr timepoints. Scale bar = 100 um.

Figure 6.13 shows the bar graph of total area covered by 1 ug/mL, 5 ug/mL, and 10 ug/mL sonicated CuHARS at 3, 24, 48, and 72 hr timepoints. The total area covered by CuHARS for all the concentrations decreases at 3, 24, 48, and 72 hr which suggests that CuHARS degrades over time. At 1 ug/mL of sonicated CuHARS the area coverage at 3 hr was 1693 μm^2 and it did not change significantly at 24 hr. However, it decreased by 50% at 48 hr and by about 80% at 72 hr. At 5 ug/mL sonicated CuHARS the area covered at 3 hr was 15,177 μm^2 and it dropped to 56% of this value at 24 hr. It further decreased to about 10% of this value at 72 hr. At 10 ug/mL sonicated CuHARS, the area

coverage at 3 hr was 28,588 μm^2 whereas it decreased to about 19% of this value by 48 hr and then to 5.6% of this value at 72 hr, where it was nearly the same as the 5 $\mu\text{g}/\text{mL}$ case at the same time point. Hence, it can be concluded that the degradation of CuHARS does not slow down even though the concentration increases at 48 and 72 hr.

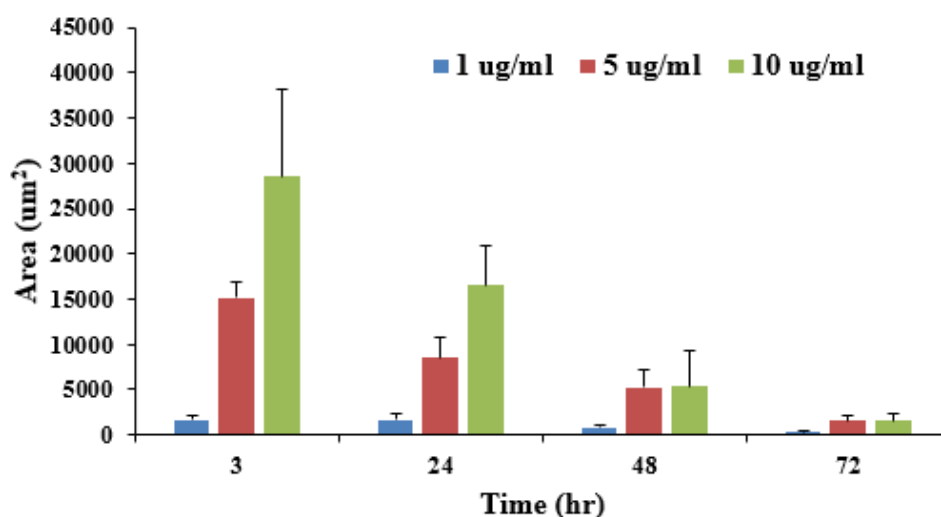


Figure 6.13: Total area covered by 1, 5, and 10 $\mu\text{g}/\text{mL}$ sonicated CuHARS at 3, 24, 48, and 72 hr timepoints.

Figure 6.14 shows the total number of objects covered by 1, 5, and 10 $\mu\text{g}/\text{mL}$ sonicated CuHARS at 3, 24, 48, and 72 hr timepoints. The total number of CuHARS for all the concentrations tested decreases progressively from 3 to 72 hr, which further supports that CuHARS degrades over time. For 1 $\mu\text{g}/\text{mL}$ sonicated CuHARS, the total number of objects was 221 at 3 hr and it dropped to 86%, 56% and 26% of this initial value at 24, 48, and 72 hr, respectively. For 5 $\mu\text{g}/\text{mL}$ sonicated CuHARS was more than four times the total number for 1 $\mu\text{g}/\text{mL}$ at 3 hr. The number of objects in 5 $\mu\text{g}/\text{mL}$

sonicated CuHARS dropped to 24% of this original value at 72 hr. For 10 ug/mL sonicated CuHARS the number was seven times the value for 1 ug/mL at 3 hr. It dropped to 14% of its 3 hr value at 72 hr.

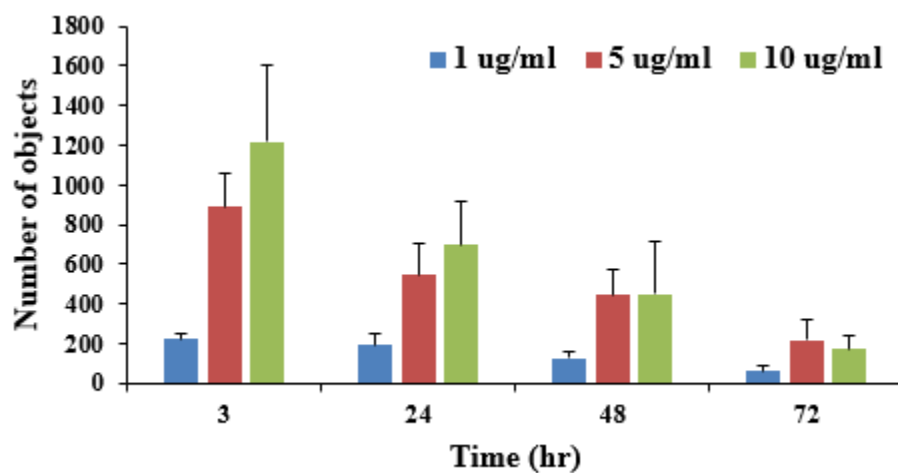


Figure 6.14: Total number of objects covered by 1, 5, and 10ug/mL sonicated CuHARS at 3, 24, 48, and 72 hr timepoints.

The size distribution for 1 ug/mL sonicated CuHARS at 3, 24, 48, and 72 hr are as shown in **Figure 6.15**. Most of the CuHARS ranged from 6-12 um in length whereas a few of them were as large as 13-33 um at 3 hr. At 24 and 48 hr timepoints, CuHARS larger than or equivalent to 20 um disappeared which suggests that CuHARS are degrading over time. However, only few CuHARS remained until 72 hr and they ranged from 3-13 um.

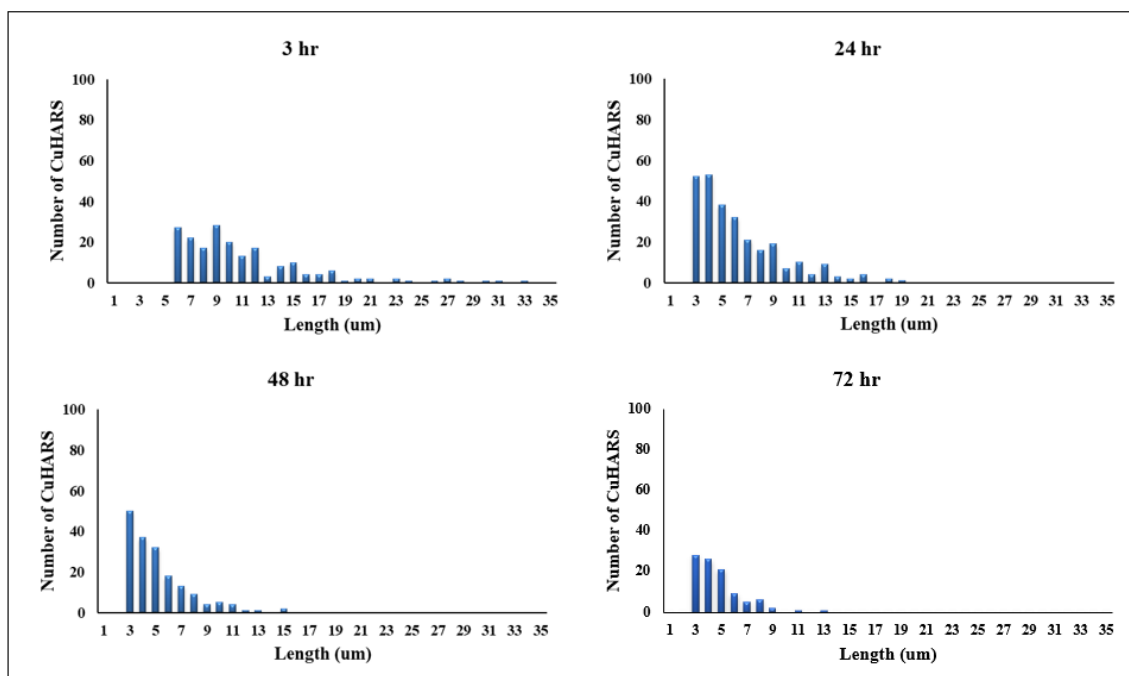


Figure 6.15: Size distribution of 1 ug/mL sonicated CuHARS at 3, 25, 48, and 72 hr.

The size distribution for 5 ug/mL sonicated CuHARS at 3, 24, 48, and 72 hr are as shown in **Figure 6.16**. Most of the CuHARS ranged from 3-13 um in length whereas a few of them were as large as 14-34 um at 3 hr. Some of the larger CuHARS disappeared at 24 hr which suggests that CuHARS was breaking down over time. At 48 hr timepoint, the size distribution for 3-4 um CuHARS increased and some of the CuHARS that ranged from 17-34 um disappeared which might indicate that the larger CuHARS are degrading and getting shorter while the smaller CuHARS are disappearing over time. However, a few of the CuHARS do not completely degrade at 72 hr but most of the CuHARS ranged from 3-10 um at 72 hr and a few ranged from 11-16 um.

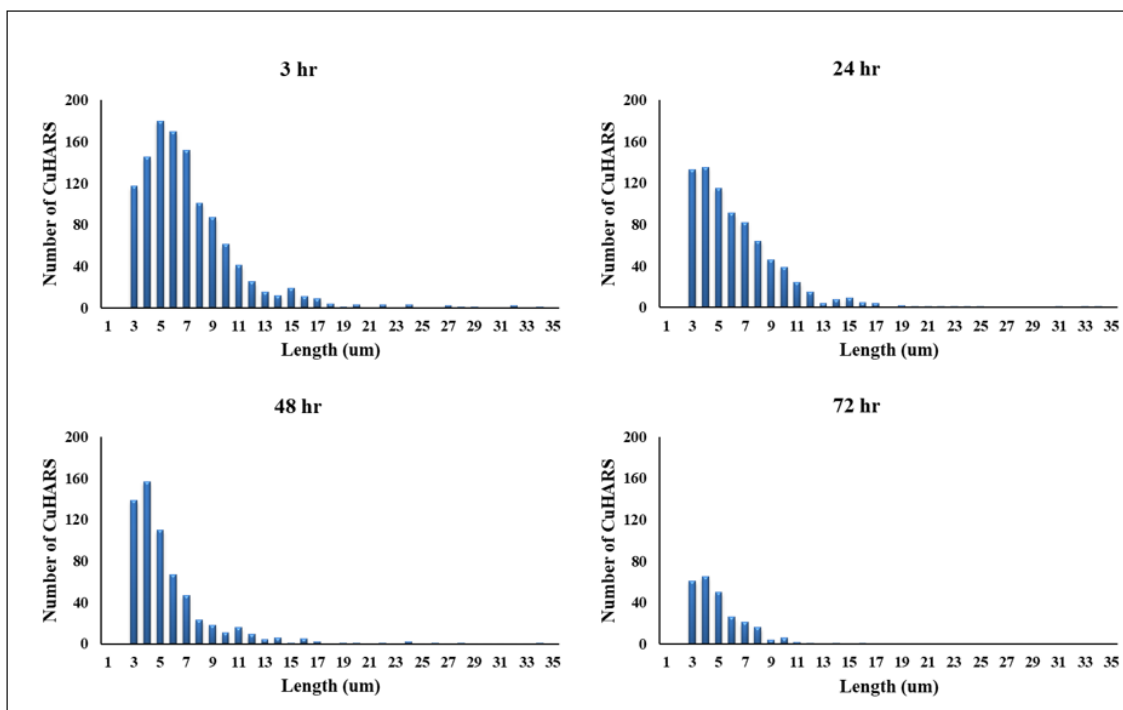


Figure 6.16: Size distribution of 5 ug/mL sonicated CuHARS at 3, 24, 48, and 72 hr.

The size distribution for 10 ug/mL sonicated CuHARS at 3, 24, 48, and 72 hr are as shown in **Figure 6.17**. Most of the CuHARS ranged from 3-18 um in length whereas a few of them were as large as 19-52 um and some were over 55 um at 3 hr. At 24 hr compared to 3 hr, less CuHARS were from 5-18 um, which suggests that CuHARS was breaking down over time, which is consistent with our findings for 5 ug/mL sonicated CuHARS. At 48 hr timepoint, more CuHARS ranged from 3-5 um and some of the longer CuHARS disappeared. However, a few of the CuHARS do not completely degrade at 72 hr.

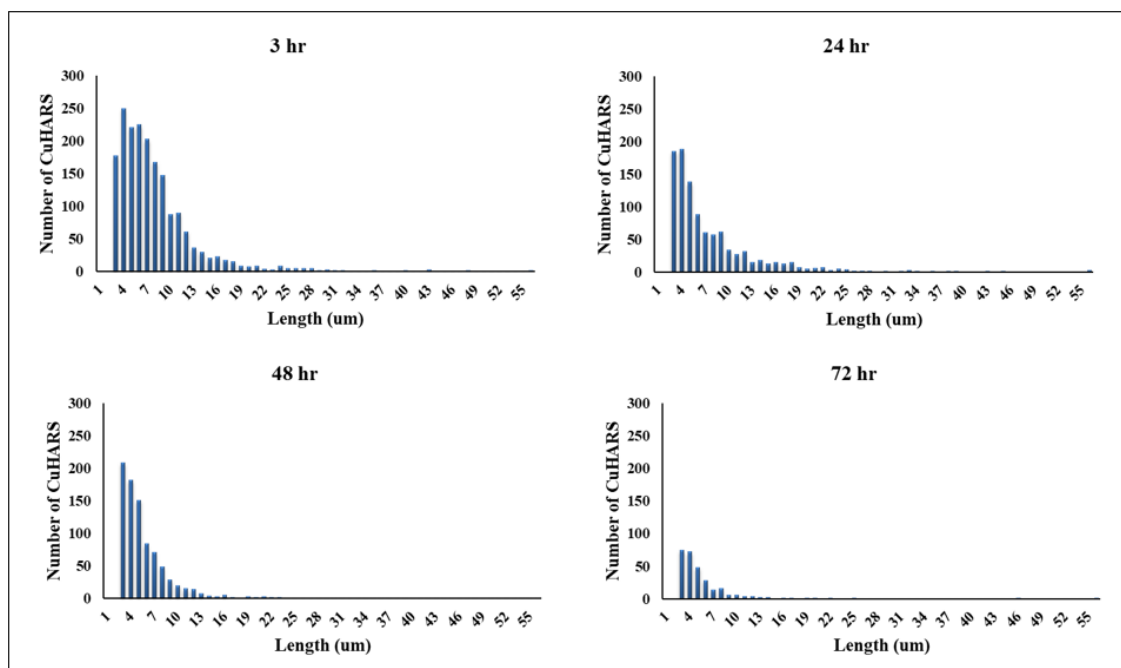


Figure 6.17: Size distribution of 10 ug/mL sonicated CuHARS at 3, 24, 48, and 72 hr.

6.4 Conclusion and Discussion

Initially, two major beneficial aspects were found for CuHARS integration with cellulose: 1) biohybrid sheets could be constructed that when dried, provided sufficient light penetration for effective imaging of materials by white light microscopy and 2) CuHARS-cellulose integrated materials were sufficiently wettable to interact with cells for initial *in vitro* testing).

For further proof of principle for comparative purposes with CuHARS, magnetically susceptible Fe₂O₃NPs were integrated into cellulose matrices. In the case of Fe₂O₃NPs, the generated material retained magnetic susceptibility for at least 8 months after fabrication with storage under dry, room temperature conditions. Due to the stability and scalability of CuHARS-cellulose matrices shown here and including incorporation of

additional functional materials such as Fe₂O₃NPs, environmental and sensor applications may be possible.

CuHARS may be stably integrated into a matrix containing the natural product cellulose, forming a convenient biohybrid. The CuHARS-cellulose biohybrid composite may also be combined with magnetically susceptible materials such as Fe₂O₃NPs for further control of the materials. The generated cellulose matrix discs are sufficiently thin to pass light for white light microscopy imaging and are sufficiently wettable and compatible with cell culture media to permit interactions for *in vitro* testing purposes. Since CuHARS are completely (but slowly) degradable under physiological conditions, incorporation of CuHARS into cellulose matrices may extend degradation lifetimes for biomedical applications.

The key considerations for any biomaterial include better understanding of degradation and how they interact with the cells. From this experiment, we observed that CuHARS interaction with cells is biphasic in the sense that it can promote cell growth at lower concentrations where as it can be toxic at high concentrations i.e. 10 ug/mL. Sonication breaks down CuHARS to more uniform size, thus causing them to exhibit the properties of nanomaterials such as agglomerating after 24 hr before degrading. However, 1 ug/mL sonicated CuHARS did not show any signs of clumping over the 72 hr timepoint. Further, CuHARS can degrade over time. Lower concentrations of CuHARS (1 ug/mL and 5 ug/mL) have a greater number of materials concentrated towards shorter lengths and they start to disappear whereas high concentrations of CuHARS (10 ug/mL) have longer lengths at the early timepoint (3 hr and 24 hr) which

breaks down into smaller lengths before finally disappearing. However, some CuHARS do not completely degrade.

Thus, potential applications of a novel biohybrid material CuHARS were explored for incorporation with cellulose and degradation of sonicated CuHARS was investigated.

CHAPTER 7

CONCLUSIONS AND FUTURE WORK

Astrocytes participate in various physiological and pathological conditions, and they are thought to influence tumor cell invasion and metastasis. In this dissertation, a co-culture model consisting of normal brain astrocytes and gliomas was developed using a mixed co-culture method to achieve a stable system that mimics the brain tumor microenvironment. Further, strategies to distinguish the different cell populations in a co-culture model was demonstrated. Understanding the complex interactions between the normal brain cells and brain tumor cells, and the relevance to tumor progression over time was achieved. Moreover, the co-culture model developed in this project provided a platform to study tumor microenvironment by overcoming the limitations between traditional monocultures and *in vivo* animal models. In most cases, anti-cancer drug treatments are tested on glioma cells only, but the co-culture model developed in this study consists of both astrocytes and glioma cells, representing a real case scenario. In future, the effect of anti-cancer drugs such as paclitaxel and doxorubicin can be studied in the co-culture model. Three-dimensional (3D) co-culture model can be developed in which the cells form aggregates or spheroids to bridge the gap between *in vitro* and *in vivo* models as well as resemble *in vivo* environment more closely than the two-dimensional (2D) model. Glutamate uptake by normal brain astrocytes and glioma cells was density dependent. However, extracellular glutamate uptake by astrocytes was six-

fold more compared to glioma cells. Results showed that uptake of glutamate by astrocytes in the presence of glioma cells was enhanced than the glutamate uptake by astrocytes alone. Inhibition of glutamate uptake may be linked to several pathological conditions. Using this co-culture system, therapeutic strategies for cancer emerging from astrocyte-tumor interaction can be developed. New technologies to measure real-time glutamate uptake in a co-culture model can be developed.

Morphological characteristics of brain cells were modified using apoptosis inducer staurosporine and necrosis inducer copper nanoparticles.

Figure 7.1 shows the schematic diagram of interaction of non-degradable and degradable biomaterials with brain cells and their outcome features.

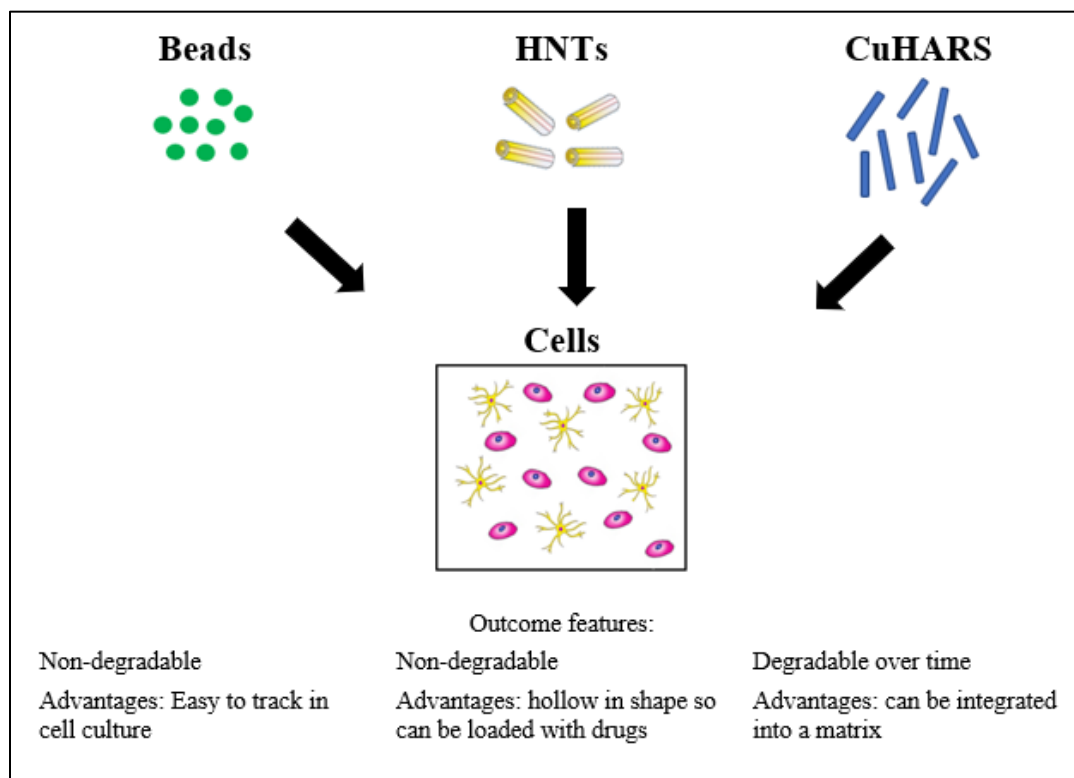


Figure 7.1: Schematic diagram of interaction of non-degradable and degradable biomaterials with brain cells and their outcome features.

While all the biomaterials have their own advantages and disadvantages, each material is chosen for their applications in the biomedical research. CuHARS are a degradable biomaterial whereas beads and halloysite nanotubes are non-degradable. Biomaterials can either be injected or implanted in the body with surgery. While the non-degradable biomaterials require further surgery for removal, degradable biomaterials do not require a second surgical event for removal. CuHARS may be integrated with cellulose to construct matrices that can be used for long term experiments. These matrices can be further controlled in time and space by combining them with magnetically susceptible materials such as Fe_2O_3 NPs. By incorporating CuHARS with cellulose matrices, CuHARS can be presented at defined densities and locations and then released in a controlled manner. This capability may provide a delayed action delivery platform to cells. CuHARS has attracted interest as it is degradable and can be integrated into a matrix, hence further surgery is not required to remove the scaffold after initial implantation surgery.

APPENDIX A
CELL CULTURE MEDIA

A.1 CRL-2303 Media

A.1.1 Materials Required for 250 mL Media

- Sterile filtration unit
- 221.25 mL Dulbecco's Modified Eagle's Medium (DMEM)
- 25 mL Fetal Bovine Serum (FBS) (10 %)
- 2.5 mL Amino acid solution (1 %)
- 1.25 mL Penicillin/Streptomycin solution (P/S) (0.5 %)

A.1.2 Preparation of CRL-2303 Growth Media

The procedure is carried out in a laminar flow hood (sterile environment).

1. Add 110.25 mL DMEM to sterile filtration unit.
2. Add Fetal Bovine Serum, Amino acid solution, and P/S to sterile filtration unit.
3. Add 111 mL DMEM to sterile filtration unit.
4. Place the lid over sterile filtration unit and connect it to vacuum nozzle.
5. Carefully turn on the vacuum and allow the liquid to pass through the filter. Make sure to hold sterile filtration unit during this step so the unit does not turn over.

Turn off the vacuum before bubbles form.
6. Twist top of filtration unit off carefully. Screw sterile cap onto container of media.
7. Label media as CRL-2303 media with date and your initials, and store in refrigerator.

A.2 Astrocyte Media

A.2.1 Materials Required for 250 mL Media

- Sterile filtration unit

- 223.75 mL Ham's F-12K media with L-Glutamine
- 12.5 mL Fetal Bovine Serum (FBS) (5.0 %)
- 12.5 mL Horse Serum (5.0 %)
- 1.25 mL Penicillin/Streptomycin solution (P/S) (0.5 %)

A.2.2 Preparation of Astrocyte Growth Media

The procedure is carried out in a laminar flow hood (sterile environment).

1. Add 100 mL Ham's F-12K media to sterile filtration unit.
2. Add Fetal Bovine Serum, Horse Serum, and P/S to sterile filtration unit.
3. Add 123.75 mL Ham's F-12K media to sterile filtration unit.
4. Place the lid over sterile filtration unit and connect it to vacuum nozzle.
5. Carefully turn on the vacuum and allow the liquid to pass through the filter. Make sure to hold sterile filtration unit during this step so the unit does not turn over.

Turn off the vacuum before bubbles form.
6. Twist top of filtration unit off carefully. Screw sterile cap onto container of media.
7. Label media as Astrocyte media with date and your initials, and store in refrigerator.

A.3 **Microglia Media**

A.3.1 Materials Required for 250 mL Media

- 211.25 mL DMEM: F-12
- 25 mL Heat-inactivated Fetal bovine serum (FBS) (10%)
- 12.5 mL Heat-inactivated Horse Serum (HS) (5%)
- 1.25 mL Penicillin/Streptomycin solution (P/S) (0.5 %)

A.3.2 Preparation of Microglia Growth Media

The procedure is carried out in a laminar flow hood (sterile environment).

1. Add 100 mL DMEM: F-12 media to sterile filtration unit.
2. Add Heat-inactivated Fetal Bovine Serum, Heat-inactivated Horse Serum, and P/S to sterile filtration unit.
3. Add 111.25 mL DMEM: F-12 media to sterile filtration unit.
4. Place the lid over sterile filtration unit and connect it to vacuum nozzle.
5. Carefully turn on the vacuum and allow the liquid to pass through the filter. Make sure to hold sterile filtration unit during this step so the unit does not turn over. Turn off the vacuum before bubbles form.
6. Twist top of filtration unit off carefully. Screw sterile cap onto container of media.
7. Label media as Astrocyte media with date and your initials, and store in refrigerator.

A.4 **Locke's Solution**

A.4.1 Materials Required for 250 mL Media

- 2250 mg of Sodium Chloride (NaCl) (154 mM)
- 104.4 mg of Potassium Chloride (KCl) (5.6 mM)
- 75.6 mg of Sodium Bicarbonate (NaHCO₃) (3.6 mM)
- 84.5 mg of Calcium Chloride (CaCl₂·2H₂O) (2.3 mM)
- 252.3 mg of Glucose (5.6 mM)
- 1.25 mL of 1M stock 4-(2-hydroxyethyle)-2-piperazineethanesulfonic acid (HEPES) (pH 7.4) (5 mM)

- 248.75 mL purified water

A.4.2 Preparation of Locke's Solution

1. Dissolve the components in 100 mL of purified water and add to the vacuum filtration unit.
2. Add 100 mL of purified water to vacuum filtration unit.
3. Add water with dissolved components.
4. Add 1.25 mL of 1 M stock HEPES.
5. Add remaining amount of purified water.
6. Place cap on unit. Carefully turn on the vacuum.
7. Allow all the liquid to pass through the filter. Turn off the vacuum before bubbles form.
8. Twist the top of vacuum unit off carefully. Screw the sterile cap onto the container of the solution.
9. Label as Locke's solution with date and your initials, and store in refrigerator.

Note: For preparing Locke's solution without sodium, replace the Sodium Chloride with same molarity of Choline Chloride. There is no any account for Sodium Bicarbonate.

APPENDIX B
FIXING CELLS

Protocol for fixation is explained in following steps:

1. Remove complete media from cell culture.
2. Wash the cells with pre-warmed Locke's solution.
3. Add the fixing solution (DiffQuik from Siemens) to cover whole surface of well or dish and leave it for 10 minutes.
4. Remove the fixing solution and add Phosphate Buffer Saline (PBS) to cover whole surface.
5. For storage, label the plate or dish, seal with parafilm and keep it at 2-8 °C (in refrigerator).

APPENDIX C

GFAP ANTIBODY (AB) STAINING

1. Fixation of Cells:
 - Remove complete media from cell culture.
 - Wash twice the cells with pre-warmed Locke's solution.
 - Add ice-cold methanol to cover whole surface of well or dish and keep it for 5 minutes.
 - Remove methanol and add 1X PBS to cover whole surface.
 - For storage seal the plate or dish with paraffin and keep it at 2-8 °C (in refrigerator).
2. Permeabilization of cells: Remove PBS from pre-fixed cells and 0.2 % Triton X 100 (in 1X PBS) to cover whole surface and keep it at room temperature for 15 minutes.
3. Blocking: Remove Triton X 100 and add 2% Goat Serum (in 1X PBS) to cover whole surface. Seal the plate or dish with paraffin and keep it at 2-8 °C (in refrigerator) for 4-5 hrs or overnight.
4. Primary Ab: Remove goat serum and add 1° Ab (Anti-GFAP produced in rabbit in 1:500 1X PBS) to cover the whole surface. Seal the plate or dish with paraffin and keep it at 2-8 °C (in refrigerator) for 24 hrs or overnight.
5. Washing: Remove 1° Ab and wash twice with 1X PBS.
6. Secondary Ab: Add 2° Ab (1:500 Goat Anti- Rabbit Ig Ab in 2% Goat Serum which is in 1X PBS) to cover the whole surface. Seal the plate or dish with paraffin and cover with aluminum foil and keep it at room temperature for 45-60 minutes.
7. Washing: Remove 2° Ab and wash twice with 0.2 % Triton X 100 (in 1X PBS). Lastly add 1X PBS to cover whole surface.
8. Fluorescence Microscopy: Observe staining using fluorescent microscope.

9. Storage: Seal the plate or dish with paraffin and cover with aluminum foil and keep it at 2-8 °C (in refrigerator) for storage for weeks.

APPENDIX D

B-GALACTOSIDASE STAINING

D.1.1 Reagents Required for Staining

- 10X PBS
70.2 mM Na₂HPO₄, 14.7 mM KH₂PO₄, 1.37 M NaCl, and 26.8 mM KCl
- 10X Fixation Buffer
20% formaldehyde and 2% glutaraldehyde in 10X PBS
- Reagent A - 200 mM MgCl₂
- Reagent B - 400 mM potassium ferricyanide
- Reagent C - 400 mM potassium ferrocyanide
- X-Gal - (5-Bromo-4-chloro-3-indolyl-B-D-galactopyranoside)
- Dimethylformamide (DMF)

D.1.2 Preparation Instructions

- Dilute 10X PBS 10-fold with sterile water to prepare 1X PBS.
- Dilute 10X Fixation Buffer 10-fold with sterile water to prepare 1X fixation solution.
- Prepare a 20 mg/mL solution of X-Gal in DMF in a polypropylene tube or a glass vial. The solution can be stored in the dark at -20 °C for 1 month.

D.1.3 Procedure for 48-well Cell Culture Plate

1. Aspirate the growth medium from the cells.
2. Wash cells twice with 300 uL of 1X PBS. Remove the wash solution entirely with aspiration.
3. Add 300 uL of 1X fixation solution and incubate 10 minutes at room temperature.
During the fixation process, prepare the staining solution in a polypropylene tube as follows:

4. Staining Solution

Component	Amount
Reagent A	10 uL
Reagent B	10 uL
Reagent C	10 uL
X-Gal solution (20 mg/mL)	50 uL
1X PBS	920 uL
Total volume	1 mL (enough for 3 wells)

5. Rinse the cells twice with 300 uL of 1X PBS.
6. Add 300 uL of staining solution to the plate. Ensure even coverage of the plate.
7. Incubate at 37 °C for 0.5-2 hr or longer, until the cells stain blue. In the event a longer staining period is needed, seal the plate with parafilm to prevent it from drying out. The exact incubation time must be optimized.
8. Observe the cells under the microscope. Count the cells and calculate the percent of stained cells to unstained cells.
9. For long-term storage of stained plate, remove the staining solution, overlay cells with 300 uL 1X PBS and store at 4 °C.

APPENDIX E
DAPI STAINING PROTOCOL

1. A 14.27 millimolar concentration of DAPI in DI water was diluted 1 to 1000 in 1x PBS.
2. Once DAPI has been added place dish in 37 °C incubator for 10 minutes (depending on the health of the cells you may need a longer time to load do to the fact that healthy cells take longer to load DAPI than damaged or dead cells).

APPENDIX F
IMAGE-PRO PLUS VERSION 7.0

F.1.1 Calculating the Area of β -gal Staining from the Image

1. Insert the dongle (special security plug) that comes with Image-Pro Plus to unlock the program.
2. Open Image-Pro Plus 7.0. A dialog box 'Macro Browser' appears. Click Done.
3. Go to File → Open → Select the image.
4. Go to Measure → Count/Size → Choose 'Manual' → Click 'Select Colors' → A dialog box appears. Click 'Color Cube Based' → Select Class '1' → Under Options, Select Sensitivity '4' → Pick 'color picker tool'. Then click on the indigo blue color staining (Start selecting the color from lightest to darkest) → Under Preview, select 'Current Class' → Change to 'Class Color on Black' from 'Class Color on Transparent' → Select 'Apply Mask' → Click 'OK'.
5. Now choose 'Automatic Bright Objects' → Click 'Count'. The white area gets selected.
6. Go to 'Measure' → Click 'Select Measurements' → Choose 'Area' → Click 'Measure'.
7. Go to 'View' → Click 'Measurement Data' → Choose 'Sort Down'.
8. Go to 'File' → Click 'Export Data'. This will copy the data into an excel spreadsheet.

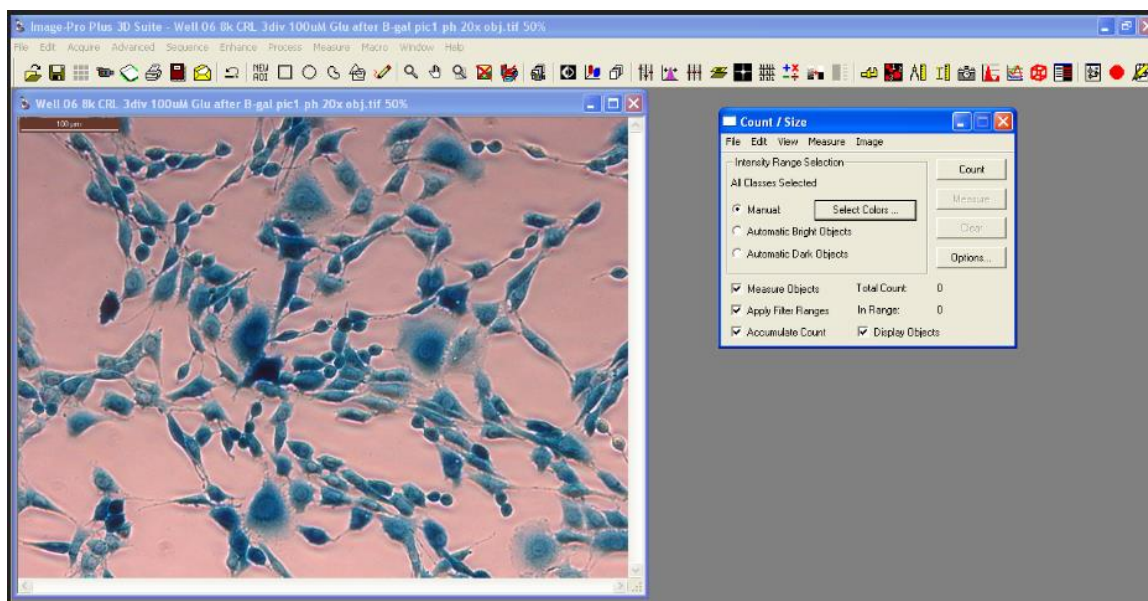


Figure F.2: An example to import an image to Image Pro-Plus 7.0 to calculate the area of β -gal staining.

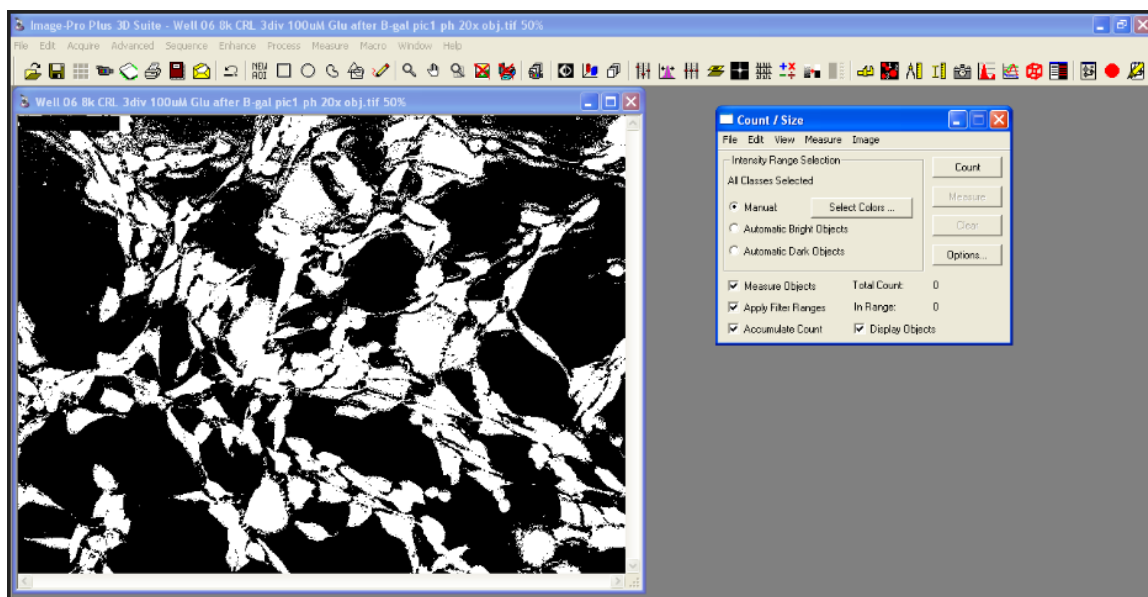


Figure F.3: An example to apply mask to the image to calculate the area of β -gal staining.

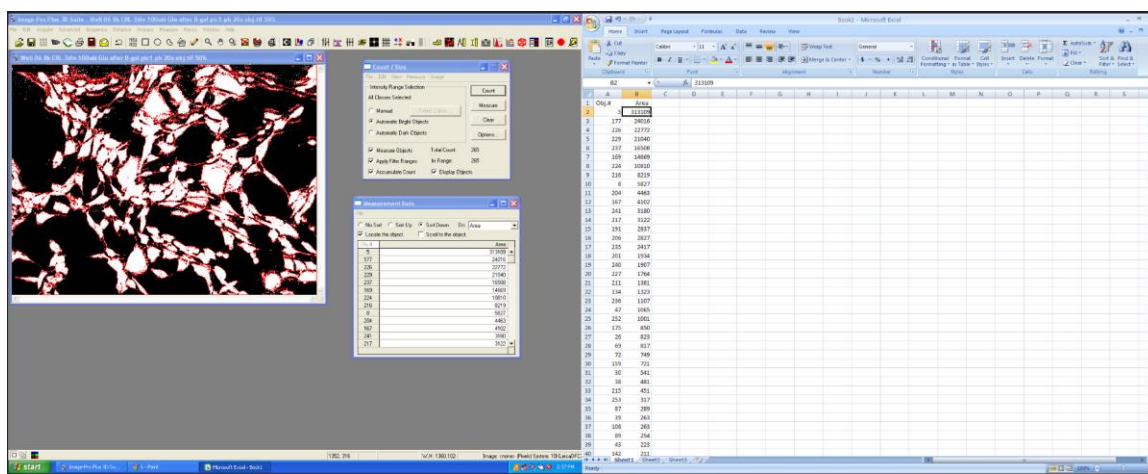


Figure F.4: An example to export the data to Excel spreadsheet using Image Pro Plus version 7.0.

BIBLIOGRAPHY

- [1] N. A. Charles, E. C. Holland, R. Gilbertson, R. Glass, and H. Kettenmann, "The brain tumor microenvironment," *Glia*, vol. 59, no. 8, pp. 1169–1180, 2011.
- [2] G. Li, Z. Qin, Z. Chen, L. Xie, R. Wang, and H. Zhao, "Tumor microenvironment in treatment of glioma," *Open Medicine*, vol. 12, no. 1, pp. 247–251, 2017.
- [3] E. Gronseth, L. Wang, D. R. Harder, and R. Ramchandran, "The Role of Astrocytes in Tumor Growth and Progression," in *Astrocyte-Physiology and Pathology*, InTech, 2018.
- [4] R. D. Hurst and I. B. Fritz, "Properties of an immortalised vascular endothelial/glioma cell co-culture model of the blood-brain barrier," *Journal of Cellular Physiology*, vol. 167, no. 1, pp. 81–88, 1996.
- [5] L. Goers, P. Freemont, and K. M. Polizzi, "Co-culture systems and technologies: taking synthetic biology to the next level," *Journal of The Royal Society Interface*, vol. 11, no. 96, p. 20140065, 2014.
- [6] N. E Savaskan, Z. Fan, T. Broggin, M. Buchfelder, and I. Y Eyupoglu, "Neurodegeneration in the brain tumor microenvironment: glutamate in the limelight," *Current Neuropharmacology*, vol. 13, no. 2, pp. 258–265, 2015.
- [7] V. L. Jacobs and J. A. De Leo, "Increased glutamate uptake in astrocytes via propentofylline results in increased tumor cell apoptosis using the CNS-1 glioma model," *Journal of Neuro-oncology*, vol. 114, no. 1, pp. 33–42, 2013.
- [8] M. Lorger, "Tumor microenvironment in the brain," *Cancers*, vol. 4, no. 1, pp. 218–243, 2012.
- [9] T. Brommeland, L. Rosengren, S. Fridlund, R. Hennig, and V. Isaksen, "Serum levels of glial fibrillary acidic protein correlate to tumour volume of high-grade gliomas," *Acta Neurologica Scandinavica*, vol. 116, no. 6, pp. 380–384, 2007.

- [10] S. Jäkel and L. Dimou, “Glial cells and their function in the adult brain: a journey through the history of their ablation,” *Frontiers in Cellular Neuroscience*, vol. 11, p. 24, 2017.
- [11] L. A. Lampson, M. A. Lampson, and A. D. Dunne, “Exploiting the lacZ reporter gene for quantitative analysis of disseminated tumor growth within the brain: use of the lacZ gene product as a tumor antigen, for evaluation of antigenic modulation, and to facilitate image analysis of tumor growth in situ,” *Cancer Research*, vol. 53, no. 1, pp. 176–182, 1993.
- [12] K. Takano, M. Ogawa, K. Kawabe, M. Moriyama, and Y. Nakamura, “Inhibition of Gap Junction Elevates Glutamate Uptake in Cultured Astrocytes,” *Neurochemical Research*, vol. 43, no. 1, pp. 50–56, 2018.
- [13] O. Prakash, W. J. Lukiw, F. Peruzzi, K. Reiss, and A. E. Musto, “Gliomas and seizures,” *Medical Hypotheses*, vol. 79, no. 5, pp. 622–626, 2012.
- [14] H. Ohgaki, “Epidemiology of brain tumors,” in *Cancer Epidemiology*, Springer, 2009, pp. 323–342.
- [15] H. Suzuki *et al.*, “Mutational landscape and clonal architecture in grade II and III gliomas,” *Nature Genetics*, vol. 47, no. 5, p. 458, 2015.
- [16] Y. Dong and E. N. Benveniste, “Immune function of astrocytes,” *Glia*, vol. 36, no. 2, pp. 180–190, 2001.
- [17] Y. Chen and R. A. Swanson, “Astrocytes and brain injury,” *Journal of Cerebral Blood Flow & Metabolism*, vol. 23, no. 2, pp. 137–149, 2003.
- [18] J. Ciesielski-Treska, M.-F. Bader, and D. Aunis, “Microtubular organization in flat epitheloid and stellate process-bearing astrocytes in culture,” *Neurochemical Research*, vol. 7, no. 3, pp. 275–286, 1982.
- [19] E. Hanson *et al.*, “Astrocytic glutamate uptake is slow and does not limit neuronal NMDA receptor activation in the neonatal neocortex,” *Glia*, vol. 63, no. 10, pp. 1784–1796, 2015.
- [20] H. K. Kimelberg and M. Nedergaard, “Functions of astrocytes and their potential as therapeutic targets,” *Neurotherapeutics*, vol. 7, no. 4, pp. 338–353, 2010.
- [21] R. H. Miller and M. C. Raff, “Fibrous and protoplasmic astrocytes are biochemically and developmentally distinct,” *Journal of Neuroscience*, vol. 4, no. 2, pp. 585–592, 1984.

- [22] L. A. Lampson, P. Wen, V. A. Roman, J. H. Morris, and J. A. Sarid, “Disseminating tumor cells and their interactions with leukocytes visualized in the brain,” *Cancer Research*, vol. 52, no. 4, pp. 1018–1025, 1992.
- [23] N. J. Maragakis and J. D. Rothstein, “Mechanisms of disease: astrocytes in neurodegenerative disease,” *Nature Reviews Neurology*, vol. 2, no. 12, p. 679, 2006.
- [24] Y. Miki, K. Ono, S. Hata, T. Suzuki, H. Kumamoto, and H. Sasano, “The advantages of co-culture over mono cell culture in simulating in vivo environment,” *The Journal of Steroid Biochemistry and Molecular Biology*, vol. 131, no. 3–5, pp. 68–75, 2012.
- [25] Y. Tanouchi, R. P. Smith, and L. You, “Engineering microbial systems to explore ecological and evolutionary dynamics,” *Current Opinion in Biotechnology*, vol. 23, no. 5, pp. 791–797, 2012.
- [26] B. Momeni, C.-C. Chen, K. L. Hillesland, A. Waite, and W. Shou, “Using artificial systems to explore the ecology and evolution of symbioses,” *Cellular and Molecular Life Sciences*, vol. 68, no. 8, p. 1353, 2011.
- [27] N. Dalchau, M. J. Smith, S. Martin, J. R. Brown, S. Emmott, and A. Phillips, “Towards the rational design of synthetic cells with prescribed population dynamics,” *Journal of the Royal Society Interface*, vol. 9, no. 76, pp. 2883–2898, 2012.
- [28] K. Alain and J. Querellou, “Cultivating the uncultured: limits, advances and future challenges,” *Extremophiles*, vol. 13, no. 4, pp. 583–594, 2009.
- [29] W. Harcombe, “Novel cooperation experimentally evolved between species,” *Evolution*, vol. 64, no. 7, pp. 2166–2172, 2010.
- [30] M. C. Hesselman *et al.*, “A multi-platform flow device for microbial (co-) cultivation and microscopic analysis,” *PLoS One*, vol. 7, no. 5, p. e36982, 2012.
- [31] A. A. Zeidan, P. Rådström, and E. W. van Niel, “Stable coexistence of two *Caldicellulosiruptor* species in a de novo constructed hydrogen-producing co-culture,” *Microbial Cell Factories*, vol. 9, no. 1, p. 102, 2010.
- [32] K. Hatherell, P.-O. Couraud, I. A. Romero, B. Weksler, and G. J. Pilkington, “Development of a three-dimensional, all-human in vitro model of the blood–brain barrier using mono-, co-, and tri-cultivation Transwell models,” *Journal of Neuroscience Methods*, vol. 199, no. 2, pp. 223–229, 2011.
- [33] N. Klitgord and D. Segrè, “Environments that induce synthetic microbial ecosystems,” *PLoS Computational Biology*, vol. 6, no. 11, p. e1001002, 2010.

- [34] D. R. Bogdanowicz and H. H. Lu, "Studying cell-cell communication in co-culture," *Biotechnology Journal*, vol. 8, no. 4, pp. 395–396, 2013.
- [35] C. Guguen-Guillouzo *et al.*, "Maintenance and reversibility of active albumin secretion by adult rat hepatocytes co-cultured with another liver epithelial cell type," *Experimental Cell Research*, vol. 143, no. 1, pp. 47–54, 1983.
- [36] A. C Paz, S. Javaherian, and A. P McGuigan, "Micropatterning co-cultures of epithelial cells on filter insert substrates," *Journal of Epithelial Biology and Pharmacology*, vol. 5, no. 1, 2012.
- [37] J. Fukuda *et al.*, "Micropatterned cell co-cultures using layer-by-layer deposition of extracellular matrix components," *Biomaterials*, vol. 27, no. 8, pp. 1479–1486, 2006.
- [38] I.-N. E. Wang *et al.*, "Role of osteoblast–fibroblast interactions in the formation of the ligament-to-bone interface," *Journal of Orthopaedic Research*, vol. 25, no. 12, pp. 1609–1620, 2007.
- [39] I.-N. E. Wang, D. R. Bogdanowicz, S. Mitroo, J. Shan, S. Kala, and H. H. Lu, "Cellular interactions regulate stem cell differentiation in tri-culture," *Connective Tissue Research*, vol. 57, no. 6, pp. 476–487, 2016.
- [40] S. Ryu *et al.*, "Nanothin coculture membranes with tunable pore architecture and thermoresponsive functionality for transfer-printable stem cell-derived cardiac sheets," *ACS Nano*, vol. 9, no. 10, pp. 10186–10202, 2015.
- [41] J. Renaud and M.-G. Martinoli, "Development of an Insert Co-culture System of Two Cellular Types in the Absence of Cell-Cell Contact.," *Journal of Visualized Experiments: JoVE*, no. 113, 2016.
- [42] K. E. Snow and S. P. Langdon, "Coculture of Ovarian Cells Using Porous Tissue Culture Inserts," in *Cancer Cell Culture*, Springer, 2004, pp. 303–306.
- [43] N. Gagliano *et al.*, "Glioma-astrocyte interaction modifies the astrocyte phenotype in a co-culture experimental model," *Oncology Reports*, vol. 22, no. 6, pp. 1349–1356, 2009.
- [44] R. Bjerkvig, O. D. Laerum, and O. Mella, "Glioma cell interactions with fetal rat brain aggregates in vitro and with brain tissue in vivo," *Cancer Research*, vol. 46, no. 8, pp. 4071–4079, 1986.
- [45] S. J. Bidarra, C. C. Barrias, M. A. Barbosa, R. Soares, J. Amédée, and P. L. Granja, "Phenotypic and proliferative modulation of human mesenchymal stem cells via crosstalk with endothelial cells," *Stem Cell Research*, vol. 7, no. 3, pp. 186–197, 2011.

- [46] W. Zhang, W. T. Couldwell, M. F. Simard, H. Song, J. H. Lin, and M. Nedergaard, "Direct gap junction communication between malignant glioma cells and astrocytes," *Cancer Research*, vol. 59, no. 8, pp. 1994–2003, 1999.
- [47] D. M. Le *et al.*, "Exploitation of astrocytes by glioma cells to facilitate invasiveness: a mechanism involving matrix metalloproteinase-2 and the urokinase-type plasminogen activator–plasmin cascade," *Journal of Neuroscience*, vol. 23, no. 10, pp. 4034–4043, 2003.
- [48] F. Gullotta, F. Schindler, R. Schmutzler, and A. Weeks-Seifert, "GFAP in brain tumor diagnosis: possibilities and limitations," *Pathology-Research and Practice*, vol. 180, no. 1, pp. 54–60, 1985.
- [49] A. Hara *et al.*, "Proliferative assessment of GFAP-positive and GFAP-negative glioma cells by nucleolar organizer region staining," *Surgical Neurology*, vol. 36, no. 3, pp. 190–194, 1991.
- [50] P. R. Maycox, J. W. Hell, and R. Jahn, "Amino acid neurotransmission: spotlight on synaptic vesicles," *Trends in Neurosciences*, vol. 13, no. 3, pp. 83–87, 1990.
- [51] Y. Zhou and N. C. Danbolt, "Glutamate as a neurotransmitter in the healthy brain," *Journal of Neural Transmission*, vol. 121, no. 8, pp. 799–817, 2014.
- [52] M.-Y. Min, D. A. Rusakov, and D. M. Kullmann, "Activation of AMPA, kainate, and metabotropic receptors at hippocampal mossy fiber synapses: role of glutamate diffusion," *Neuron*, vol. 21, no. 3, pp. 561–570, 1998.
- [53] M. H. Baslow, "A novel key–lock mechanism for inactivating amino acid neurotransmitters during transit across extracellular space," *Amino Acids*, vol. 38, no. 1, pp. 51–55, 2010.
- [54] H. R. Arias, "Marine toxins targeting ion channels," *Marine Drugs*, vol. 4, no. 3, pp. 37–69, 2006.
- [55] E. S. Valenstein, "The discovery of chemical neurotransmitters," *Brain and Cognition*, vol. 49, no. 1, pp. 73–95, 2002.
- [56] B. Si and E. Song, "Recent Advances in the Detection of Neurotransmitters," *Chemosensors*, vol. 6, no. 1, p. 1, 2018.
- [57] D. L. Roe, "From DOPA to Parkinson's disease: the early history of dopamine research," *Journal of the History of the Neurosciences*, vol. 6, no. 3, pp. 291–301, 1997.
- [58] A. Schousboe and H. S. Waagepetersen, "GABA: homeostatic and pharmacological aspects," *Progress in Brain Research*, vol. 160, pp. 9–19, 2007.

- [59] A. R. Butler and R. Nicholson, *Life, death and nitric oxide*, vol. 33. Royal Society of Chemistry, 2003.
- [60] F. Fonnum, “Glutamate: a neurotransmitter in mammalian brain,” *Journal of Neurochemistry*, vol. 42, no. 1, pp. 1–11, 1984.
- [61] J. R. Stern, L. V. Eggleston, R. Hems, and H. A. Krebs, “Accumulation of glutamic acid in isolated brain tissue,” *Biochemical Journal*, vol. 44, no. 4, p. 410, 1949.
- [62] T. HAYASHI, “Effects of sodium glutamate on the nervous system,” *The Keio Journal of Medicine*, vol. 3, no. 4, pp. 183–192, 1954.
- [63] R. Bear, D. Rintoul, B. Snyder, M. Smith-Caldas, and C. Herren, *Principles of Biology*, vol. 1. New Prairie Press, 2016.
- [64] A. V. Tzingounis and J. I. Wadiche, “Glutamate transporters: confining runaway excitation by shaping synaptic transmission,” *Nature Reviews Neuroscience*, vol. 8, no. 12, p. 935, 2007.
- [65] L. Pellerin and P. J. Magistretti, “Glutamate uptake into astrocytes stimulates aerobic glycolysis: a mechanism coupling neuronal activity to glucose utilization,” *Proceedings of the National Academy of Sciences*, vol. 91, no. 22, pp. 10625–10629, 1994.
- [66] Z.-C. Ye, J. D. Rothstein, and H. Sontheimer, “Compromised glutamate transport in human glioma cells: reduction–mislocalization of sodium-dependent glutamate transporters and enhanced activity of cystine–glutamate exchange,” *Journal of Neuroscience*, vol. 19, no. 24, pp. 10767–10777, 1999.
- [67] B. Meldrum, “Possible therapeutic applications of antagonists of excitatory amino acid neurotransmitters,” *Clinical Science*, vol. 68, no. 2, pp. 113–122, 1985.
- [68] D. E. Bergles and C. E. Jahr, “Glial contribution to glutamate uptake at Schaffer collateral–commissural synapses in the hippocampus,” *Journal of Neuroscience*, vol. 18, no. 19, pp. 7709–7716, 1998.
- [69] K. Tanaka *et al.*, “Epilepsy and exacerbation of brain injury in mice lacking the glutamate transporter GLT-1,” *Science*, vol. 276, no. 5319, pp. 1699–1702, 1997.
- [70] S. M. O’Donovan, C. R. Sullivan, and R. E. McCullumsmith, “The role of glutamate transporters in the pathophysiology of neuropsychiatric disorders,” *NPJ Schizophrenia*, vol. 3, no. 1, p. 32, 2017.
- [71] N. C. Danbolt, “Glutamate uptake,” *Progress in Neurobiology*, vol. 65, no. 1, pp. 1–105, 2001.

- [72] Y. Kanai and M. A. Hediger, "Primary structure and functional characterization of a high-affinity glutamate transporter," *Nature*, vol. 360, no. 6403, p. 467, 1992.
- [73] P. M. Beart and R. D. O'shea, "Transporters for L-glutamate: an update on their molecular pharmacology and pathological involvement," *British Journal of Pharmacology*, vol. 150, no. 1, pp. 5–17, 2007.
- [74] Y. Shigeri, R. P. Seal, and K. Shimamoto, "Molecular pharmacology of glutamate transporters, EAATs and VGLUTs," *Brain Research Reviews*, vol. 45, no. 3, pp. 250–265, 2004.
- [75] A. C. Fontana, "Current approaches to enhance glutamate transporter function and expression," *Journal of Neurochemistry*, vol. 134, no. 6, pp. 982–1007, 2015.
- [76] S. Duan, C. M. Anderson, B. A. Stein, and R. A. Swanson, "Glutamate induces rapid upregulation of astrocyte glutamate transport and cell-surface expression of GLAST," *Journal of Neuroscience*, vol. 19, no. 23, pp. 10193–10200, 1999.
- [77] C. Perego *et al.*, "The GLT-1 and GLAST glutamate transporters are expressed on morphologically distinct astrocytes and regulated by neuronal activity in primary hippocampal cocultures," *Journal of Neurochemistry*, vol. 75, no. 3, pp. 1076–1084, 2000.
- [78] C. Mim, P. Balani, T. Rauen, and C. Grewer, "The glutamate transporter subtypes EAAT4 and EAATs 1-3 transport glutamate with dramatically different kinetics and voltage dependence but share a common uptake mechanism," *The Journal of General Physiology*, vol. 126, no. 6, pp. 571–589, 2005.
- [79] A. Hacimuftuoglu *et al.*, "Astrocyte/neuron ratio and its importance on glutamate toxicity: an in vitro voltammetric study," *Cytotechnology*, vol. 68, no. 4, pp. 1425–1433, 2016.
- [80] A. A. Jensen, C. Fahlke, W. E. Bjørn-Yoshimoto, and L. Bunch, "Excitatory amino acid transporters: recent insights into molecular mechanisms, novel modes of modulation and new therapeutic possibilities," *Current Opinion in Pharmacology*, vol. 20, pp. 116–123, 2015.
- [81] K. Tanaka, "Antibiotics rescue neurons from glutamate attack," *Trends in Molecular Medicine*, vol. 11, no. 6, pp. 259–262, 2005.
- [82] U. Sonnewald and A. Schousboe, "Introduction to the glutamate–glutamine cycle," in *The Glutamate/GABA-Glutamine Cycle*, Springer, 2016, pp. 1–7.

- [83] L. Hertz, “The glutamate–glutamine (GABA) cycle: importance of late postnatal development and potential reciprocal interactions between biosynthesis and degradation,” *Frontiers in Endocrinology*, vol. 4, p. 59, 2013.
- [84] O. Devinsky, A. Vezzani, S. Najjar, N. C. De Lanerolle, and M. A. Rogawski, “Glia and epilepsy: excitability and inflammation,” *Trends in Neurosciences*, vol. 36, no. 3, pp. 174–184, 2013.
- [85] M. Barker-Haliski and H. S. White, “Glutamatergic mechanisms associated with seizures and epilepsy,” *Cold Spring Harbor Perspectives in Medicine*, p. a022863, 2015.
- [86] H. Sontheimer, “A role for glutamate in growth and invasion of primary brain tumors,” *Journal of Neurochemistry*, vol. 105, no. 2, pp. 287–295, 2008.
- [87] S. C. Buckingham *et al.*, “Glutamate release by primary brain tumors induces epileptic activity,” *Nature Medicine*, vol. 17, no. 10, p. 1269, 2011.
- [88] A. G. Thomas *et al.*, “High-throughput assay development for cystine-glutamate antiporter (xc-) highlights faster cystine uptake than glutamate release in glioma cells,” *PloS One*, vol. 10, no. 8, p. e0127785, 2015.
- [89] N. A. Jackman, T. F. Uliasz, J. A. Hewett, and S. J. Hewett, “Regulation of System xc- Activity and Expression in Astrocytes by Interleukin-1 β : Implications for Hypoxic Neuronal Injury,” *Glia*, vol. 58, no. 15, pp. 1806–1815, 2010.
- [90] H. Sontheimer, “A role for glutamate in growth and invasion of primary brain tumors,” *Journal of Neurochemistry*, vol. 105, no. 2, pp. 287–295, 2008.
- [91] S. A. Lyons, W. J. Chung, A. K. Weaver, T. Ogunrinu, and H. Sontheimer, “Autocrine glutamate signaling promotes glioma cell invasion,” *Cancer Research*, vol. 67, no. 19, pp. 9463–9471, 2007.
- [92] C. Joshi, B. Karumuri, J. J. Newman, and M. A. DeCoster, “Cell morphological changes combined with biochemical assays for assessment of apoptosis and apoptosis reversal,” *Curr Microsc Contrib to Adv Sci Technol (A Méndez-Vilas, Ed)*, pp. 756–762, 2012.
- [93] P. A. Rosenberg, S. Amin, and M. Leitner, “Glutamate uptake disguises neurotoxic potency of glutamate agonists in cerebral cortex in dissociated cell culture,” *Journal of Neuroscience*, vol. 12, no. 1, pp. 56–61, 1992.
- [94] D. Gerlier and N. Thomasset, “Use of MTT colorimetric assay to measure cell activation,” *Journal of Immunological Methods*, vol. 94, no. 1–2, pp. 57–63, 1986.

- [95] G. Ciapetti, E. Cenni, L. Pratelli, and A. Pizzoferrato, "In vitro evaluation of cell/biomaterial interaction by MTT assay," *Biomaterials*, vol. 14, no. 5, pp. 359–364, 1993.
- [96] A. Bahuguna, I. Khan, V. K. Bajpai, and S. C. Kang, "MTT assay to evaluate the cytotoxic potential of a drug," *Bangladesh Journal of Pharmacology*, vol. 12, no. 2, pp. 115–118, 2017.
- [97] A. Strasser, L. O'Connor, and V. M. Dixit, "Apoptosis signaling," *Annual Review of Biochemistry*, vol. 69, no. 1, pp. 217–245, 2000.
- [98] S. Elmore, "Apoptosis: a review of programmed cell death," *Toxicologic Pathology*, vol. 35, no. 4, pp. 495–516, 2007.
- [99] M. A. DeCoster, "The nuclear area factor (NAF): a measure for cell apoptosis using microscopy and image analysis," *Modern Research and Educational Topics in Microscopy*, pp. 378–384, 2007.
- [100] G. Majno and I. Joris, "Apoptosis, oncosis, and necrosis. An overview of cell death.," *The American Journal of Pathology*, vol. 146, no. 1, p. 3, 1995.
- [101] R. Oliveira *et al.*, "Contribution of gap junctional communication between tumor cells and astroglia to the invasion of the brain parenchyma by human glioblastomas," *BMC Cell Biology*, vol. 6, no. 1, p. 7, 2005.
- [102] P. G. Lal, R. S. Ghirnikar, and L. F. Eng, "Astrocyte-astrocytoma cell line interactions in culture," *Journal of Neuroscience Research*, vol. 44, no. 3, pp. 216–222, 1996.
- [103] M. Aubert, M. Badoual, C. Christov, and B. Grammaticos, "A model for glioma cell migration on collagen and astrocytes," *Journal of the Royal Society Interface*, vol. 5, no. 18, pp. 75–83, 2008.
- [104] S. Yamada *et al.*, "Carnitine-induced senescence in glioblastoma cells," *Experimental and Therapeutic Medicine*, vol. 4, no. 1, pp. 21–25, 2012.
- [105] W. Ma, K. Rogers, B. Zbar, and L. Schmidt, "Effects of different fixatives on β -galactosidase activity," *Journal of Histochemistry & Cytochemistry*, vol. 50, no. 10, pp. 1421–1424, 2002.
- [106] R. N. Mukherjee, P. Chen, and D. L. Levy, "Recent advances in understanding nuclear size and shape," *Nucleus*, vol. 7, no. 2, pp. 167–186, 2016.
- [107] I. V. Chekhonin, D. A. Chistiakov, N. F. Grinenko, and O. I. Gurina, "Glioma Cell and Astrocyte Co-cultures As a Model to Study Tumor–Tissue Interactions: A Review of Methods," *Cellular and Molecular Neurobiology*, pp. 1–17.

- [108] W. J. Chung *et al.*, “Inhibition of cystine uptake disrupts the growth of primary brain tumors,” *Journal of Neuroscience*, vol. 25, no. 31, pp. 7101–7110, 2005.
- [109] W. J. Chung and H. Sontheimer, “Sulfasalazine inhibits the growth of primary brain tumors independent of nuclear factor- κ B,” *Journal of Neurochemistry*, vol. 110, no. 1, pp. 182–193, 2009.
- [110] C. Grewer, A. Gameiro, and T. Rauen, “SLC1 glutamate transporters,” *Pflügers Archiv-European Journal of Physiology*, vol. 466, no. 1, pp. 3–24, 2014.
- [111] Z.-C. Ye and H. Sontheimer, “Glioma cells release excitotoxic concentrations of glutamate,” *Cancer Research*, vol. 59, no. 17, pp. 4383–4391, 1999.
- [112] D. R. Brown, “Neurons depend on astrocytes in a coculture system for protection from glutamate toxicity,” *Molecular and Cellular Neuroscience*, vol. 13, no. 5, pp. 379–389, 1999.
- [113] I. Khan, K. Saeed, and I. Khan, “Nanoparticles: Properties, applications and toxicities,” *Arabian Journal of Chemistry*, 2017.
- [114] L. E. Dike, C. S. Chen, M. Mrksich, J. Tien, G. M. Whitesides, and D. E. Ingber, “Geometric control of switching between growth, apoptosis, and differentiation during angiogenesis using micropatterned substrates,” *In Vitro Cellular & Developmental Biology-Animal*, vol. 35, no. 8, pp. 441–448, 1999.
- [115] C. S. Chen, M. Mrksich, S. Huang, G. M. Whitesides, and D. E. Ingber, “Micropatterned surfaces for control of cell shape, position, and function,” *Biotechnology Progress*, vol. 14, no. 3, pp. 356–363, 1998.
- [116] L. Zhao *et al.*, “Staurosporine Induces Platelet Apoptosis Through p38 Mitogen-Activated Protein Kinase Signaling Pathway.,” *Clinical Laboratory*, vol. 61, no. 7, pp. 717–726, 2015.
- [117] Y. M. Lvov, M. M. DeVilliers, and R. F. Fakhrullin, “The application of halloysite tubule nanoclay in drug delivery,” *Expert Opinion on Drug Delivery*, vol. 13, no. 7, pp. 977–986, 2016.
- [118] M. Ljungman and P. C. Hanawalt, “The anti-cancer drug camptothecin inhibits elongation but stimulates initiation of RNA polymerase II transcription,” *Carcinogenesis*, vol. 17, no. 1, pp. 31–36, 1996.
- [119] Y. Yang, Y. Chen, F. Leng, L. Huang, Z. Wang, and W. Tian, “Recent advances on surface modification of halloysite nanotubes for multifunctional applications,” *Applied Sciences*, vol. 7, no. 12, p. 1215, 2017.

- [120] K. C. Kelly, J. R. Wasserman, S. Deodhar, J. Huckaby, and M. A. DeCoster, "Generation of scalable, metallic high-aspect ratio nanocomposites in a biological liquid medium," *Journal of Visualized Experiments: JoVE*, no. 101, 2015.
- [121] A. Karan, M. Darder, U. Kansakar, Z. Norcross, and M. A. DeCoster, "Integration of a Copper-Containing Biohybrid (CuHARS) with Cellulose for Subsequent Degradation and Biomedical Control," *International Journal of Environmental Research and Public Health*, vol. 15, no. 5, 2018.
- [122] Q. Xing, F. Zhao, S. Chen, J. McNamara, M. A. DeCoster, and Y. M. Lvov, "Porous biocompatible three-dimensional scaffolds of cellulose microfiber/gelatin composites for cell culture," *Acta Biomaterialia*, vol. 6, no. 6, pp. 2132–2139, 2010.
- [123] M. Jorfi and E. J. Foster, "Recent advances in nanocellulose for biomedical applications," *Journal of Applied Polymer Science*, vol. 132, no. 14, 2015.
- [124] S. Deodhar, J. Huckaby, M. Delahoussaye, and M. A. DeCoster, "High-aspect ratio bio-metallic nanocomposites for cellular interactions," in *IOP Conference Series: Materials Science and Engineering*, 2014, vol. 64, p. 012014.
- [125] T. Saito, S. Kimura, Y. Nishiyama, and A. Isogai, "Cellulose nanofibers prepared by TEMPO-mediated oxidation of native cellulose," *Biomacromolecules*, vol. 8, no. 8, pp. 2485–2491, 2007.